Doctoral Program in Fluid mechanics
Doctoral Program in Civil and Environmental Engineering (XXXVIII cycle)

Wind-tunnel study on the influence of trees on street canyon ventilation

Focus on tree density, street canyon geometry, and wind direction

Doctoral Dissertation by

Annika Vittoria Del Ponte

******

Supervisors:
Sofia Fellini
Luca Ridolfi
Pietro Salizzoni
Lionel Soulhac

Doctoral Examination Committee:
Maria Grazia Badas, Examiner, Università degli Studi di Cagliari
Sofia Fellini, invited, Politecnico di Torino
Christof Gromke, Examiner, Karlsruher Institut für Technologie
Costantino Manes, Examiner, Politecnico di Torino
Paolo Monti, Reviewer, Università di Roma "La Sapienza"
Luca Ridolfi, Examiner, Politecnico di Torino
Pietro Salizzoni, Examiner, École Centrale de Lyon
Lionel Soulhac, Examiner, École Centrale de Lyon
Christina Vanderwel, Reviewer, University of Southampton

Politecnico di Torino & École Centrale de Lyon
2025

Declaration

I hereby declare that, the contents and organization of this dissertation constitute my own original work and does not compromise in any way the rights of third parties, including those relating to the security of personal data.

Annika Vittoria Del Ponte
2025

The important thing is not to stop questioning
Albert Einstein

Acknowledgements

I am really grateful to my supervisors Sofia Fellini, Luca Ridolfi, Pietro Salizzoni, and Lionel Soulhac for the huge help that they gave me in realising the work presented in this thesis. They generously shared with me their great knowledge about fluid mechanics, they had always inspiring ideas to develop my PhD subject, and they provided me with solid foundations to grow as a researcher. I also thank them, as well as the two hosting universities Politecnico di Torino and École Centrale de Lyon, for giving me the possibility to carry out a joint PhD program. This experience allowed me to grow both professionally and personally. Moreover, I thank a lot Massimo Marro for his great availability, his patience, and his crucial support in the wind tunnel and in my work, during my period in Lyon. I thank also Horacio Correira, for his technical support in the wind tunnel and his friendliness.

I would like to thank a lot Paolo Monti and Christina Vanderwel for the careful reading and review of this thesis. Their comments helped me a lot to improve the final version of the thesis and to think on some important concepts of my work. I thank also Christoph Gromke for the careful reading of the thesis and his very interesting comments.

I am also grateful to Professor Carlo Camporeale, who gave me the possibility to teach exercises in his course of "Hydraulics". I thank him a lot for his availability to clarify my doubts.

Preamble

This thesis has been carried out with a joint PhD program between the DIATI (Dipartimento di Ingegneria per l'Ambiente, il Territorio e le Infrastrutture) departement of Politecnico di Torino and LMFA (Laboratoire de Mécanique des Fluides et d'Acoustique) laboratory of École Centrale de Lyon. This thesis is part of the projects ARIA P@LIT@, funded by DIATI, and VEB-MU, funded by the Auvergne-Rhône-Alpes Region.

Part of the work presented in this thesis was published in two scientific papers:

- Del Ponte A.V., Fellini S., Marro M., van Reeuwijk M., Ridolfi L., Salizzoni P. (2024) *Influence of street trees on turbulent fluctuations and transport processes in an urban canyon: a wind tunnel study*. Boundary-Layer Meteorology, Vol. 190.
- Del Ponte A.V., Fellini S., Marro M., Soulhac L., Ridolfi L., Salizzoni P. (2025) *The Turbulent Flow within a Wind-Aligned Street Canyon with Trees: an Experimental Study*. Boundary-Layer Meteorology, Vol. 191.

Abstract

Inserting vegetation within cities leads to several benefits, including higher deposition of air pollutants, mitigation of the air temperature, regulation of storm water runoff, and creation of recreational areas. However, the aerodynamic effect of vegetation is not always positive for air quality, especially within urban streets. For example, in tree-lined avenues, wind speeds are low and pollutants accumulate at the pedestrian level. Most experimental studies about the aerodynamic effect of trees on street canyon ventilation focus on two-dimensional isolated canyons perpendicular to the external wind. Other wind directions or more complex urban geometries received less attention. Moreover, velocity and concentration turbulent fluctuations were poorly investigated, even though their importance in the vertical exchange between the urban canopy and the external atmosphere. To fill these gaps, we performed concentration, velocity, and simultaneous concentration-velocity measurements within a street canyon, modeled inside the wind tunnel of École Centrale de Lyon. We analysed the turbulent flow and concentration fields within a canyon, considering different street aspect ratio, wind directions, tree densities, and the presence of street intersections. The aerodynamic effect of trees was simulated by placing two rows of plastic miniatures along the canyon's lateral walls. We used ground-level sources of a passive tracer to simulate traffic pollution.

The results show that, with orthogonal wind direction, the presence of trees hinders the upward mean vertical velocity close to the upwind wall and reduces the turbulent kinetic energy and turbulent mass fluxes inside the canyon, with respect to a non-vegetated case. As a consequence, the increase in tree density leads to a strongly heterogeneous spatial pattern of the mean and turbulent concentration field along the canyon. At the rooftop, with high tree density, the mean concentration increases by 75%, moving from the downwind to the

upwind wall. Within a wind-aligned street canyon, high density vegetation with touching crowns reduces the mean longitudinal velocity by 80% and decreases velocity fluctuations by 15%, compared to an empty wind-aligned canyon. At the rooftop, the interaction between the external flow and tree crowns leads to 30% increase in velocity fluctuations. As the height-to-width ratio decreases (i.e., for wider canyons), a vegetation-free corridor between the rows of trees results in 25% decrease in mean longitudinal velocity and 30% increase in velocity fluctuations compared to the empty large canyon. This induces a street ventilation more efficient with respect to the vegetated narrow canyon, especially when pollutants are emitted at pedestrian level. With oblique wind direction, the coexistence of longitudinal flow and transversal recirculation within the non-vegetated canyon promotes the entrainment of fresh air from the external flow into the canyon, along the downwind wall, and the accumulation of pollutants in the canyon central core. The presence of trees hinders the longitudinal and transversal mean flows within the canyon, but it enhances turbulent fluctuations and pollutant mixing in correspondence of the downwind tree. This causes an almost zero mean concentration at the downwind wall and in the canyon centre and 70% higher mean concentration at the upwind wall.

The presence of street intersections causes flow detachment regions, dampens the transversal recirculation, increases flow velocity fluctuations with respect to the laterally-closed canyon, especially with oblique wind direction and in the absence of trees. Conversely, trees alter lateral flow structures and partially re-establish the turbulent flow field typical of a canyon without intersections.

In addition to the innovative experimental results, the detailed dataset collected during this thesis can be exploited to validate analytical models and numerical simulations for better urban air quality management.

Résumé

La végétation dans les villes implique plusieurs avantages, notamment la majeur déposition des polluants, la réduction de la température, la régulation des écoulements des eaux pluviales et la création d'espaces de loisirs. Cependant, l'effet aérodynamique de la végétation n'est pas toujours positif pour la qualité de l'air, surtout dans les rues urbaines. Par exemple, dans les avenues bordées d'arbres, la vitesse du vent est faible et les polluants s'accumulent au niveau des piétons. La plupart des études expérimentales sur l'effet aérodynamique des arbres sur la ventilation des canyons urbains considèrent des canyons bidimensionnels isolés, perpendiculaires au vent extérieur. Les autres directions du vent ou géométries des rues plus complexes ont reçu moins d'attention. De plus, les fluctuations turbulentes de vitesse et de concentration ont été peu étudiées, malgré leur rôle important dans l'échange vertical entre la canopée urbaine et l'atmosphère extérieure. Pour combler ces lacunes, nous avons effectué des mesures de concentration, de vitesse et de mesures simultanées concentration-vitesse dans un canyon urbain, modélisé dans la soufflerie de l'École Centrale de Lyon. Nous avons analysé les champs de concentration et de vitesse turbulents dans un canyon, en considérant plusieurs géométries de la rue, directions du vent, densités des arbres et la présence des intersections des rues. L'effet aérodynamique des arbres a été reproduit en plaçant des miniatures d'arbres en plastique le long des parois du canyon. Nous avons utilisé des sources de traceur passif, placées au sol, pour simuler la pollution due au trafic.

Les résultats montrent que, avec une direction du vent orthogonale à la rue, la présence des arbres entrave la vitesse verticale moyenne près de la paroi amont par rapport au vent et réduit l'énergie cinétique turbulente et les flux de masse turbulents dans le canyon, par rapport au cas sans arbres. En conséquence,

l'augmentation de la densité des arbres entraîne une distribution spatiale très hétérogène de la concentration moyenne et turbulent le long du canyon. Au sommet du canyon, avec une densité des arbres élevée, la concentration moyenne augmente de 75% de paroi amont au paroi aval par rapport au vent. Dans un canyon parallèle au vent, une densité élevée d'arbres avec des couronnes qui se croisent réduit la vitesse longitudinale moyenne de 80% et réduit les fluctuations de vitesse de 15% par rapport au canyon vide parallèle au vent. Au sommet du canyon, l'interaction entre l'écoulement extérieur et les couronnes des arbres entraîne une augmentation de 30% des fluctuations de vitesse. Lorsque le rapport d'aspect du canyon diminue (i.e., dans les canyons larges), un couloir libre entre les lignes d'arbres ne provoque qu'une diminution de 25% de la vitesse longitudinale moyenne et une augmentation de 30% des fluctuations turbulentes de vitesse, par rapport à un canyon large vide. Cela induit une ventilation de rue plus efficace par rapport au canyon étroit avec les arbres, en particulier quand les polluants sont émis au niveau des piétons.

Avec une direction du vent oblique, la coexistence d'un écoulement longitudinal et d'une recirculation transversale dans le canyon sans arbres favorise l'entraînement d'air de l'extérieur dans le canyon, le long de la paroi aval par rapport au vent, et l'accumulation de polluants au centre du canyon. La présence d'arbres bloque les écoulements longitudinal et transversal moyens dans le canyon, mais elle augmente les fluctuations turbulentes et le *mixing* des polluants en correspondance de l'arbre aval par rapport au vent. Cela implique une concentration moyenne quasi nulle proche du paroi aval par rapport au vent et au centre du canyon, et une concentration moyenne supérieure de 70% proche de la paroi amont par rapport au vent.

La présence d'intersections cause des zones de détachement de l'écoulement, modifie la recirculation transversale et augmente les fluctuations turbulentes de la vitesse par rapport au canyon sans intersections, en particulier avec une direction du vent oblique et en l'absence d'arbres. Au contraire, les arbres bloquent les structures turbulentes sur les côtés du canyon et rétablissent partiellement le champ de vitesse turbulent typique d'un canyon sans intersections.

En plus de résultats expérimentaux innovants, l'ensemble de données collectées au cours de cette thèse est utile pour valider des modèles analytiques

et des simulations numériques afin d'améliorer la gestion de la qualité de l'air urbain.

Sommario

La vegetazione nelle città comporta diversi vantaggi, tra cui la maggiore deposizione di inquinanti, la diminuzione della temperatura, la regolazione dei flussi d'acqua piovana e la creazione di zone di svago. Tuttavia, l'effetto aerodynamico della vegazione non è sempre positivo, soprattutto nei canyon urbani. Ad esempio, nei viali alberati la velocità del vento è bassa e gli inquinanti si accumulano a livello dei pedoni. La maggior parte degli studi sperimentali sull'effetto aerodinamico degli alberi sulla ventilazione dei canyon urbani considerano canyon isolati bidimensionali, perpendicolari rispetto al vento esterno. Altre direzioni del vento o geometrie urbane più complesse hanno ricevuto meno attenzione. Inoltre, le fluttuazioni turbolente di velocità e concentrazione sono state poco studiate, nonostante il loro ruolo importante negli scambi verticali tra l'ambiente urbano e l'atmosfera esterna. Per colmare queste lacune, abbiamo effettuato misure di concentrazione, velocità e misure accoppiate concentrazione-velocità in un canyon urbano, riprodotto nella galleria del vento dell'École Centrale de Lyon. Abbiamo analizzato i campi turbolenti di velocità e concentrazione, considerando diverse geometrie del canyon, direzioni del vento, densità di alberi e la presenza di intersezioni stradali. L'effetto aerodinamico degli alberi è stato riprodotto inserendo miniature di alberi in plastica lungo le pareti del canyon. Abbiamo usato sorgenti di scalare passivo, posizionate a livello del suolo, per simulare l'inquinamento dovuto al traffico.

I risultati mostrano che, con una direzione del vento ortogonale rispetto al canyon, la presenza di alberi ostacola la velocità media verticale vicino alla parete di monte rispetto al vento e causa la riduzione dell'energia cinetica turbolenta e dei flussi di massa turbolenti all'interno del canyon, rispetto ad una configurazione senza alberi. Di conseguenza, l'aumento della densità di alberi provoca una forte eterogeneità spaziale della concentrazione media e

turbolenta lungo il canyon. Al tetto del canyon, con alta densità di alberi, la concentrazione media aumenta del 75%, spostandosi transversalmente dalla parete di valle alla parete di monte del canyon. Nel canyon parallelo al vento esterno, un'alta densità di alberi con le chiome che si intersecano riduce del 80% la velocità media longitudinale e del 15% le fluttuazioni turbolente di velocità, rispetto a un canyon vuoto parallelo al vento. Al tetto, l'interazione tra il flusso esterno e le chiome degli alberi causa un aumento del 30% delle fluttuazioni turbolente di velocità. Al diminuire del rapport d'aspetto del canyon (i.e., in canyon larghi), un corridoio libero tra le file di alberi causa la diminuzione solo del 25% della velocità media longitudinale e l'aumento del 30% delle fluttuazioni turbolente di velocità, rispetto a un canyon largo vuoto. Ciò comporta ad una ventilazione del canyon più efficace rispetto ad un canyon stretto con alberi, in particolare quando gli inquinanti vengono emessi a livello pedonale.

Con una direzione del vento obliqua, la coesistenza di un flusso longitudinale e una recircolazione trasversale nel canyon senza alberi favorisce l'entrata di aria proveniente dal flusso esterno nel canyon, lungo la parete di valle, e l'accumulo di inquiananti al centro del canyon. La presenza di alberi ostacola i flussi medi longitudinali e transversali nel canyon, ma aumenta le fluttuazioni turbolente e il *mixing* turbolento degli inquinanti in corrispondenza dell'albero di valle rispetto al vento esterno. Questo causa una concetrazione media quasi nulla vicino alla parete di valle e al centro del canyon e una concetrazione più alta del 70% alla parete di monte.

La presenza di intersezioni causa regioni di distacco del flusso, inibisce la recircolazione transversale, aumenta le fluttuazioni turbolente di velocità rispetto a un canyon senza incroci, soprattutto con direzione del vento obliqua e in assenza di alberi. Al contrario, gli alberi alterano le strutture turbolente ai lati del canyon e ristabiliscono parzialmente il campo di moto turbolento tipico di un canyon senza intersezioni.

Oltre ai risultati sperimentali innovativi, il dataset dettagliato raccolto durante questa tesi è utile per validare modelli analitici o simulazioni numeriche per migliorare la gestione della qualità dell'aria in ambiente urbano.

Contents

List of symbols **xvi**

1 Introduction **1**

2 Experimental set-up and measuring techniques **10**

2.1 The atmospheric wind tunnel and urban geometry modeling . . 10

2.2 Measuring instruments 13

2.2.1 Hot-Wire Anemometer 13

2.2.2 Laser Doppler Anemometer 13

2.2.3 Flame Ionization Detector 14

2.3 Aerodynamic characterisation of the model trees 15

2.4 Boundary layer above buildings 17

3 Turbulent fluctuations and transport processes in a canyon perpendicular to the external flow **23**

3.1 Experimental details 24

3.1.1 Turbulent mass fluxes measurements 26

3.2 Results 28

3.2.1 Flow field 28

3.2.2 Concentration field 36

3.2.3 Vertical mass transport 42

3.3 Conclusions to Chapter 3 48

4 Turbulent flow within a wind-aligned street canyon 51

4.1 Experimental details 52

4.2 Longitudinal homogeneity along the street canyon 55

4.3 Results: turbulent flow field within the street canyon 58

4.3.1 Square street canyon: H/W=1 58

4.3.2 Large street canyon: H/W_w=0.5 65

4.4 Results: analytical modeling 70

4.4.1 Empty canyon 71

4.4.2 Vegetated canyon 75

4.5 Conclusions to Chapter 4 78

5 Turbulent flow within a canyon with intersections for different wind directions 81

5.1 Experimental details 83

5.2 Velocity field in a street canyon without intersections for different wind directions 85

5.2.1 Cross-sectional velocity field in the street canyon 85

5.2.2 Transversal velocity profiles 92

5.2.3 Cross section-averaged mean longitudinal velocity 92

5.3 Velocity field in a street canyon with intersections for different wind directions 95

5.3.1 Cross-sectional velocity field in the street canyon 95

5.3.2 Transversal velocity profiles 104

5.3.3 Cross section-averaged mean longitudinal velocity 106

5.3.4 Discussion about the flow field within a street network without vegetation 109

5.4 Conclusions to Chapter 5 111

6 Experimental evaluation of the canyon ventilation 115

6.1 Experimental details 117

6.2 Concentration field in a street canyon without intersections for different wind directions 119

6.2.1 Cross-sectional concentration field in the street canyon . 120

6.2.2 Vertical exchange velocity 123

6.3 Concentration field in a street canyon with intersections for different wind directions 129

6.3.1 Cross-sectional concentration field in the street canyon . 129

6.3.2 Vertical exchange velocity 135

6.4 Conclusions to Chapter 5 138

7 Conclusions and perspectives 141

Appendix A Expressions of the third and fourth moments of the gamma, lognormal, and Weibull distributions 155

Appendix B Longitudinal homogeneity in the wind-aligned square street canyon 157

Appendix C Turbulent flow field within a wind-aligned square canyon in the Half configuration 159

Appendix D Mean and turbulent flow fields in the centre of the vegetated canyon with intersections 161

Appendix E Comparison between velocity statistics measured with LDA and HWA 163

List of symbols

Latin symbols

A_c	Projected frontal area of the tree
a_w	Scale parameter of the Weibull 2p distribution
$c(t)$	Time series of the concentration in one point
$c'(t)$	Instantaneous fluctuations of the concentration
$\overline{c}$	Time-averaged concentration in one point
C_{ad}	Experimental spatial average of the mean scalar concentration in the cross-section of the canyon
C_v	Coefficient of variation of the concentration
C_{vol}	Experimental spatial average of the mean scalar concentration in the three-dimensional control volume of the canyon
d	zero-plane displacement
F	Probability distribution
f	Sampling frequency
f_{ad}	Non-dimensional sampling frequency
F_d	Drag force of trees
H	Height of the blocks
H_T	Height of the model tree

H/W Height-to-width ratio of square streets

H/W_w Height-to-width ratio of wide streets

J_0, J_1 Bessel functions of the first kind

k^* Turbulent kinetic energy normalised by U_∞^2

K_u One-point kurtosis of the concentration

Ku_u, Ku_v One-point kurtosis of the streamwise and transversal velocity

L Length of the reference canyon

l_d Length of the tree drag

L_s Length of the linear source

L_T Length of the tree canopy

$\mathcal{P}$ Production of turbulent kinetic energy

p Pressure

Q_{et} Ethane mass flowrate

Re_δ Reynolds number of the flow

Re_H Reynolds numbers based on the obstacle height and $\overline{u}_H$

Re_r Roughness Reynolds number

Re_∞ Reynolds numbers based on the obstacle height and U_∞

S_k One-point skewness of the concentration

S_u, S_v, S_w Spectra of streamwise, transversal, and vertical velocity fluctuations

Sk_u, Sk_v One-point skewness of the streamwise and transversal velocity

t Time

$u(t), v(t), w(t)$ Time series of the streamwise, transversal, and vertical velocity in one point

$u'(t), v'(t), w'(t)$ Instantaneous fluctuations of the streamwise, transversal, and vertical velocity

$\overline{u}, \overline{v}, \overline{w}$ Time-averaged streamwise, transversal, and vertical velocity in one point

U_{an} Analytical average mean longitudinal velocity in the cross-section of the canyon

$U_{an,\theta}$ Analytical average mean longitudinal velocity in the cross-section for any wind direction θ

U_{δ_i} Mean streamwise velocity at $y = \delta_i$

u_d Bulk vertical exchange velocity within the canyon without intersections

u_d^+ Bulk vertical exchange velocity within the canyon with intersections

U_{exp} Experimental spatial average of the mean longitudinal velocity in the cross-section of the empty canyon

$\overline{u}_H$ Mean streamwise velocity in the centreline of the canyon rooftop

U_{lin} Cell-weighted spatial average of the resampled $\overline{u}$ measurements in the empty canyon adding the missing data close to the canyon boundaries by extrapolation with linear law

U_m Mean longitudinal velocity at the centreline of the rooftop

$U_{\parallel}$ Component of U_∞ projected along the longitudinal axis of the canyon

$U_{\parallel,log}$ Cell-weighted spatial average of the resampled $\overline{u}$ measurements in the empty canyon adding the missing data close to the canyon boundaries by extrapolation with logarithmic law

$U_{\perp}$ Component of U_∞ projected along the cross-wind axis of the canyon

u_* Friction velocity

u_*^s Friction velocity at the canyon floor

$U_{tr,exp}$ Experimental spatial average of the mean longitudinal velocity in the cross-section of the vegetated canyon

$U_{tr,lin}$ Cell-weighted spatial average of the resampled $\overline{u}$ measurements in the vegetated canyon adding the missing data close to the canyon boundaries by extrapolation with linear law

$U_{tr,log}$ Cell-weighted spatial average of the resampled $\overline{u}$ measurements in the vegetated canyon adding the missing data close to the canyon boundaries by extrapolation with logarithmic law

U_∞ Streamwise velocity at the top of the boundary layer

$\overline{u'w'}$ Reynolds stresses

W Width of narrow streets

W_T Width of the model tree

W_w Width of large streets

$\overline{w'c'}$ Cross-correlation between velocity and concentration fluctuations

x, y, z Longitudinal, transversal, and vertical coordinates of the reference system

Y_0, Y_1 Bessel functions of the second kind

z_i Roughness of the canyon walls

z_0 aerodynamic roughness length

Greek symbols

$\alpha_{op,c}$ Optical porosity of the vegetated cross-section

α_t Aerodynamic porosity of the model tree

$\Gamma(\cdot)$ Gamma function

δ_1 Depth of the boundary layer of Configuration 1

δ_2 Depth of the boundary layer of Configuration 2

δ_i Thickness of the boundary layer developed along the canyon boundaries

Δt_{lag} Time delay between the concentration and velocity signal

ε	Dissipation of turbulent kinetic energy
θ	Angle between the approaching flow and the longitudinal axis of the reference canyon
ϑ	Shape parameter of the gamma distribution
κ	von Kármán constant
λ_t	Pressure loss coefficient of the trees
λ_w	Pressure loss coefficient of the canyon walls
ν	Kinematic viscosity of the air at 19°C
ρ_a	Air density at 25°C
σ_c	Standard deviation of the concentration in one point
$\sigma_u, \sigma_v, \sigma_w$	Standard deviation of the streamwise, transversal, and vertical velocity in one point
τ_H	Shear stress exerted by the external flow at the canyon rooftop
$\chi(t)$	Sample space variable of the concentration

Abbreviations

an	Analytical
exp	Experimental
FID	Flame Ionization Detector
HWA	Hot-Wire Anemometer
LDA	Laser Doppler Anemometer
LES	Large Eddy Simulations
lin	Linear
log	Logarithmic
pdf	Probability density function

RANS Reynolds-averaged Navier–Stokes

t.k.e Turbulent kinetic energy

tr Trees

UBL Urban Boundary Layer

Chapter 1

Introduction

The exposure to air pollution is one of the major risk for the human health. It causes serious diseases, like asthma, stroke, ischaemic heart disease, and lung cancer (EEA, 2020). According to the World Health Organization (WHO), air pollution was responsible for 6.7 million premature deaths worldwide, in 2019 (WHO, 2023). In 2021, WHO updated its air quality guidelines with more stringent values for the most dangerous pollutants for the health, i.e., nitrogen dioxide (NO_2), Particulate Matter ($PM_{2.5}$ and PM_{10}), ozone (O_3), carbon monoxide (CO), and sulfur dioxide (SO_2). Considering the new guidelines, the *State of Global Air 2024* Report (HEI, 2024) reported that almost 34% of the World's population is exposed to air that exceeds healthy-air levels. Cities are one of the major hot-spots for air pollution, since they host several sources of pollutants of concern for the human health. For example, in European cities, road traffic is the main source of NO_2, while household heating is responsible for 43% of the emissions of PM_{10} and 62% of the emissions of $PM_{2.5}$ (EEA, 2024). The Unites Nations reported that, nowadays, 57% of the Word's population lives in cities and this percentage will increase to 68% by 2050. For this reason, cities around the World began to implement concrete measures to reduce air pollution.

One of the most encouraged strategies to reduce urban air pollution is the greening of cities. Vegetation removes gaseous and particle pollutants from the air by dry deposition and absorption on the leaves, with an efficiency which depends on the leaf area density, wind speed, and plant species (Diener and



Figure 1.1 Examples of green spaces in (a) Hong Kong, (b) London, (c) Sydney, (d) Lyon, (e) Turin, and (f) Milan.

Mudu, 2021; Zhang et al., 2021; Linden et al., 2023). Moreover, during the daytime, photosynthesis guarantees CO_2 sequestration (Nowak and Crane, 2002; Ferrini and Fini, 2011). From the aerodynamic point of view, small-size vegetation limits the movement of suspended pollutants from vehicle traffic to sidewalks (Gromke et al., 2016; Abhijith et al., 2017; Bao et al., 2025), reducing pedestrians' exposure to traffic pollution. In addition to air pollution removal, urban vegetation provides other ecosystem services, that improve the liveability of cities, reduce air temperature and mitigate the vulnerability to extreme rainfall events (Ferrini et al., 2020; Ji et al., 2024). The presence of trees in urban streets decreases air temperature by shading and increases moisture by transpiration (Oliveira et al., 2011; Grilo et al., 2020). In addition, they limit the evaporation of the air humidity transpired from the humid soil, by limiting the entrance of solar radiation into street canyons (Aboelata and Sodoudi, 2020; Zheng et al., 2023). The mitigation of air temperature within the urban environment attenuates the energy consumption of buildings for air conditioning during summer (Wang et al., 2019; Hsu and Chao, 2021). Green areas increase the amount of permeable surface and therefore the infiltration capacity of urban terrain. This ensures the regulation of stormwater runoff, and an increase of soil moisture for evapotranspiration (Zölch et al., 2017; Marrazzo and Raimondi, 2025). Besides, green areas offer human and ecosystem well-being, providing natural areas for amusement, increasing biodiversity, and attenuating noise

pollution, when they are placed close to the noise source (Van Renterghem et al., 2015; Zhao et al., 2021).

To take advantage of the benefits of vegetation, many cities implemented strategic programs to increase trees in the urban environment (Fig. 1.1), to do maintenance of existing species, and to provide guidelines for optimal tree-planting plannings (Clemente et al., 2025). Among them, Paris developed the *Plan Arbre* in 2020, which provides for planting 170,000 trees in the city between 2020 and 2026. Thanks to this planning, Paris planted around 130,000 trees from 2020 to present. Many other cities in France are implementing similar plans to improve the air quality and mitigate the urban heat island effect (e.g., Lyon, Bordeaux). For example, Lyon city restored an old industrial site close to the city centre into a park, inserting 6700 m^2 of green spaces over a surface of 11,000 m^2. This action created a cooling island within a densely populated area. Also Italy is working to increase green spaces in cities. In 2018, the FORESTAMI project started in Milan, aimed at planting 3 million new trees and shrubs within the metropolitan area of Milan by 2030 (Pastore et al., 2025). Thanks to this project, already 611,400 trees where planted around the city. Rome is currently developing a Street Tree Master Plan (STMP) based on the conservation of existing trees and the adaptation of the tree-planting to the type of streets, with particular attention to preserving the landscape identity and historical heritage of the city (Corona et al., 2024; Clemente et al., 2025). Outside Europe, developing countries such as China adopted greening policy to tackle the air pollution problem in cities. In Hong Kong, the Civil Engineering and Development Department implemented the Greening Master Plans (GMP) for urban areas in 2011, to guide the planning, design, and implementation of green infrastructures and the choice of planting species. Thanks to this plan, around 25,000 trees were planted up to present. Also the city of Beijing added 14.6 ha of green areas, over the past decade.

Even though vegetation provides several benefits to the urban environment – e.g., removes air pollution from the air, mitigates air temperature, regulates storm water runoff, create recreational areas for citizens – its aerodynamic effects is not always beneficial for the air quality. For example, the presence of trees reduces the wind velocity within street canyons and alters pollutant dispersion mechanisms, depending on its density, its spatial configuration, as well as the relative location of the pollutant source (Abhijith et al., 2017).

This aspect must be considered when designing green infrastructure (Tomson et al., 2021). Experimentally, the aerodynamic effect of vegetation on pollutant dispersion in urban areas was studied in wind tunnels, as reviewed by Zhao et al. (2023a), placing reduced-scale vegetation in model street canyons. Pioneering experimental studies by Gromke and Ruck (2007, 2009) demonstrated that trees with large crowns, or small tree spacing, cause an increase in the mean scalar concentration in the canyon higher than smaller or scattered trees, and that the concentration of pollutants (emitted at ground level) is sensitive to variation in crown porosity, it is is greater than 97%. With a wind blowing with an angle of 45° with respect to the canyon axis, the increase of pollutant concentration due to the presence of trees is still detectable (Gromke and Ruck, 2012). More recently, Fellini et al. (2022) provided a high-resolution three-dimensional characterization of the mean concentration field within a canyon placed in an urban district, and subject to an orthogonal wind, for different vegetation densities. They found that, in a canyon with height-to-width ratio 0.5, the longitudinal tree spacing has a remarkable impact on the spatial distribution of the mean and turbulent pollutant concentration and that the presence of trees deteriorates the air quality at the pedestrian level. Conversely, small vegetation (i.e., hedges) reduces the pedestrian exposure to high scalar concentration close to the canyon walls (Gromke et al., 2016; Carlo et al., 2024). In addition to the concentration field, a study by Zhao et al. (2023b) investigated the effect of trees on the turbulent flow and heat exchanges within street canyons. They found that large trees dampen momentum fluxes at the canyon rooftop and hinder heat removal from the inner canyon to the rooftop, while small trees enhance turbulent fluctuations and promote airflow exchange with the external flow.

A vegetation-induced increase in mean concentration within isolated urban canyons, orthogonal to the external wind, was also observed with Reynolds-averaged Navier–Stokes simulations (RANS) (Gromke et al., 2008; Buccolieri et al., 2009) and Large Eddy Simulations (LES) (Moonen et al., 2013; Merlier et al., 2018). Grylls and van Reeuwijk (2022) employed LES to study the effects of trees on air quality in street canyons, using a vegetation model that incorporates deposition, shading, and aerodynamic drag (Grylls and van Reeuwijk, 2021) and analysing the two competing processes affecting air quality: the beneficial role of deposition on the leaves and the reduced

ventilation induced by trees aerodynamics. In addition to the vegetation effects, Zhang et al. (2021) analysed the effects of wind direction and wind speed on deposition and dispersion of pollutant particles within vegetated canyons, with a Computational Fluid Dynamic model. They showed that the optimal vegetation configuration and type to improve the air quality within canyons depend on the spatial distribution of the pollutant concentration, which is governed by the external wind direction. A recent numerical study by Li et al. (2023) quantified the benefits of vegetation on the thermal comfort within orthogonal canyons. They found that high tree density significantly decreases the air temperature within only-pedestrian streets, while high tree density within busy streets, especially along the upwind wall, leads to pollutant accumulation at the pedestrian level, rather than improvement on the thermal comfort. RANS simulations were exploited also to investigate the influence of vegetation, wind direction, and street geometry on the ventilation within realistic urban neighborhoods by Buccolieri et al. (2011) and Jeanjean et al. (2015). They highlighted the crucial role of trees in the flow dynamics and pollutant distribution in complex urban geometries: the presence of trees could be beneficial for the air quality in low density built-up areas, with a street-axis parallel wind direction, or, in the case of a perpendicular wind direction, when deposition exceeds the aerodynamic effect (Jeanjean et al., 2017; Buccolieri et al., 2018).

The results from numerical studies highlighted that the aerodynamic effect of trees on urban canyon ventilation depends on many factors, like building and street geometries, wind direction, vegetation density and displacement, the presence of street intersections. Even though numerical models allowed many of these aspects to be investigated simultaneously, their results need to be validated with experimental data. However, the majority of experimental studies focus on mean pollutant concentration within simplified two-dimensional vegetated canyons, perpendicular to the prevailing wind. The wind-tunnel study by Gromke and Ruck (2012) is the only one investigating the combined effect of street geometry and wind direction on the mean concentration field within a vegetated canyon. Also turbulent fluctuations of concentration and velocity fields within vegetated canyons were poorly investigated experimentally, even though their importance in pollutant transport and mixing within canyons and on the vertical exchange between vegetation (Poggi et al., 2004; Pietri

et al., 2009) or urban canopies (Salizzoni et al., 2011; Di Bernardino et al., 2018) and the external boundary layer. To our knowledge, the experimental study by Zhao et al. (2023b) is the first investigation of the influence of tree size on vertical turbulent momentum fluxes between the canyon and the external flow. However, other studies investigating turbulent flow and concentration fields within vegetated urban canopies with non-orthogonal wind directions or three-dimensional street geometries are completely missing.

In this framework, the aim of this thesis is to present the results of a high-resolution experimental investigation of the turbulent flow and scalar concentration fields within an urban canyon, considering different wind directions, street height-to-width ratio, vegetation densities, and the presence of street intersections. We performed concentration, velocity and coupled concentration-velocity measurements within street canyons with different geometries, inserted within a street network modeled inside the atmospheric wind tunnel of École Centrale de Lyon. With the experimental data collected in this work, we evaluated the spatially-averaged mean longitudinal velocity in urban canyons, the pressure loss coefficient associated to trees, and the vertical exchange velocity between the canyon and the external atmosphere, which can be incorporated into analytical models or numerical simulation aimed at modeling pollutant dispersion within urban geometries.

General concepts about the Urban Boundary Layer

The Urban Boundary Layer (UBL) is the part of the Atmospheric Boundary Layer passing through cities (Fig. 1.2a). Its physical behaviour is influenced by the roughness and the thermal effects of the city. In this thesis, we assume neutral stratification, thus turbulence is generated only by mechanical processes. In the vertical direction, the UBL is divided into two regions: the inertial region and the roughness sub-layer. In the inertial region, the wind flow is homogeneous in the horizontal planes and its vertical evolution is reasonably described by a logarithmic law (details about the logarithmic law and its modeling in the wind tunnel are provided in the next chapter). The roughness sub-layer is the part of UBL which interacts with the urban elements. It is heterogeneous in the horizontal planes, since it is affected by the position, the geometry, and the orientation of buildings with respect to the approaching flow. A formal

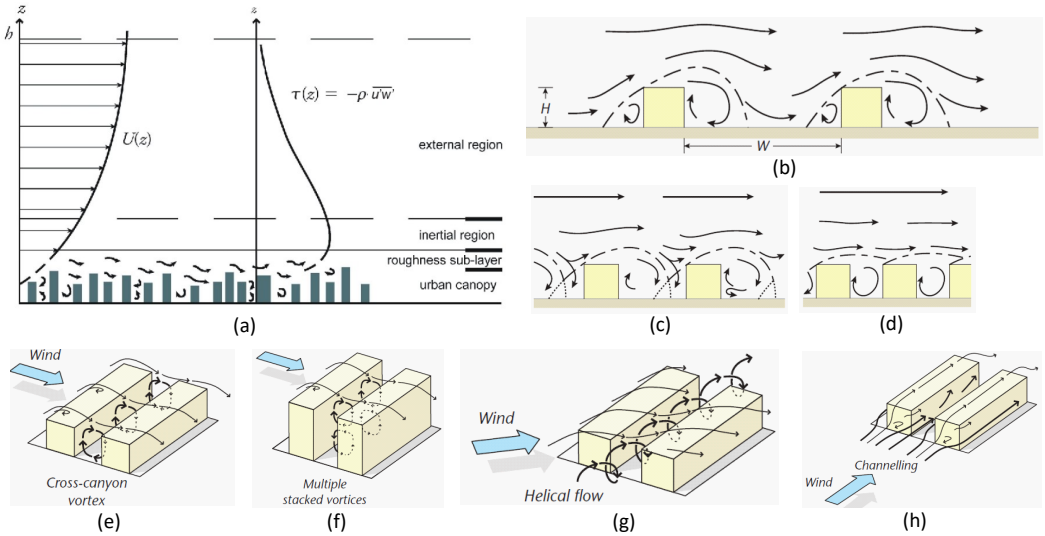


Figure 1.2 (a) Vertical structure of the atmospheric boundary layer above the urban canopy (Source: Cancelli et al. (2006)). Flow regimes associated with different urban geometries: (b) isolated roughness flow, (c) wake interference, and (d) skimming flow (Source: Oke et al. (2017)). Flow structures within street canyons with (e-f) perpendicular, (g) oblique, and (h) parallel wind directions with respect to the street axis (Source: Oke et al. (2017)).

law to describe the flow behaviour between building is not provided, but it is possible to distinguish three different regimes based on the building density (Oke et al., 2017). The distinction among the regimes is based on the street aspect ratio H/W (being H the building height and W the along-wind spacing). If the obstacles are sufficiently spaced apart ($H/W < 0.35$), the flow has time to recover its undisturbed condition before investing a second obstacle. The flow pattern between the two obstacles appears to be the same as if they were isolated and this regime is called *isolated roughness flow regime* (Fig. 1.2b). For lower spacing between buildings ($0.35 < H/W < 0.65$), the flow cannot recover its initial conditions before investing the second obstacle, thus the wakes generated by the single obstacles interact. This regime is called *wake interference flow regime* (Fig. 1.2c). Finally, the *skimming flow regime* (Fig. 1.2d) occurs when the building spacing is further decreased ($H/W > 0.65$) and the flow in the canyon becomes decoupled from the flow above the buildings.

In the wind tunnel, the urban complexity is modeled as a network of urban street canyons, that are street of width W flanked by two buildings of height H. In this thesis, we consider buildings of homogeneous height and

flat roofs. Depending on the wind direction (θ), we can identify some known flow structures within the street canyon. Notably, with the wind blowing perpendicular to the canyon longitudinal axis (θ=90°), the canyon flow is dominated by a recirculating vortex, that occupies the entire cross-section of the canyon (Fig. 1.2e). For very large H/W, a secondary counter-rotating vortex generates towards ground level (Fig. 1.2f), while within large canyons (i.e., for small H/W), a secondary vortex generates in the upwind part of the cross-section of the canyon. With oblique wind direction (30°< θ <70°), the transversal recirculation is coupled with a flow channeling and a helicoidal flow pattern is created (Fig. 1.2g). With street axis-parallel wind direction (θ<30°), the flow is channeled along the canyon (Fig. 1.2h).

In addition to building and streets, other elements can be found in real cities, such as industries, parks, skyscrapers, means of transports, water bodies. In this dissertation, we consider the presence of trees within urban canyons. The trees are modeled as obstacles made by porous material. The vital functions of trees, as well as evapotranspiration phenomenon, deposition and filtration of pollutants are neglected in our model. The aerodynamic effect of trees on the urban flow is characterised by the drag coefficient and the pressure loss coefficient.

Structure of the thesis

This thesis is structured in seven chapters. Chapter 2 contains the description of the wind-tunnel facility, the measuring instruments, and the characterisation of the boundary layer above the two different street networks considered in the thesis (i.e., a regular street network and a street network with different widths of longitudinal and transversal streets). In Chapter 3, we analyse the influence of vegetation density on the turbulent scalar concentration and vertical velocity fields and on turbulent mass fluxes, within a canyon perpendicular to the external flow. We present the first attempt of simultaneous measurements of velocity and scalar concentration, within a vegetated canyon. The subsequent chapters are dedicated to the analysis of the flow and concentration fields within canyons with non-orthogonal wind directions. In Chapter 4, we present the mean and turbulent flow fields within a two-dimensional wind-aligned street canyon. We analyse two vegetation configurations (empty and vegetated canyons) and

two canyon height-to-width ratios. Moreover, we compare the experimental data collected in the empty canyon configurations with the analytical model developed by Soulhac et al. (2008) and we provide an estimation of the pressure loss coefficient associated with trees, using the experimental data collected in the vegetated canyon configurations. In Chapter 5, we analyse the influence of wind direction, presence of vegetation, and street intersections on the mean and turbulent flow fields within a square canyon. The analysis of the effects of these parameters on the mean concentration field and ventilation efficiency within a square canyon is addressed in Chapter 6. In Chapter 7, we draw the general conclusions of this thesis.

Chapter 2

Experimental set-up and measuring techniques

2.1 The atmospheric wind tunnel and urban geometry modeling

Experiments were conducted in the atmospheric wind tunnel at the Laboratoire de Mécanique des Fluides et d'Acoustique, at École Centrale de Lyon (Fig. 2.1a). This recirculating wind tunnel features a test section that is 12 m long, 2 m high, and 3.5 m wide. It is equipped with an axial fan capable of generating wind velocities ranging from 0.5 to 6 ms^{-1}, as well as a heat exchanger system to regulate air temperature. Inside the test section, we recreated a network of streets at a 1:200 scale, with a geometry similar to the one adopted by Garbero et al. (2010), covering the floor with square blocks measuring 0.5 m on each side and H=0.1 m high. The distance between the obstacles was varied according to two different configurations. Configuration 1 consists of obstacles spaced by 0.2 m in the streamwise direction and by 0.1 m in the spanwise direction (see Fig. 2.1b). Narrower streamwise streets (height-to-width ratio H/W=1, where W is the width of narrow streets) and wider perpendicular streets (H/W_w=0.5, where W_w is the width of large streets) were arranged to avoid flow channeling. Configuration 2 is a regular network of square streets, reproduced with blocks 0.1 m spaced apart both in the streamwise and spanwise direction (see Fig. 2.1c-d). In both configurations, on the top of the blocks,

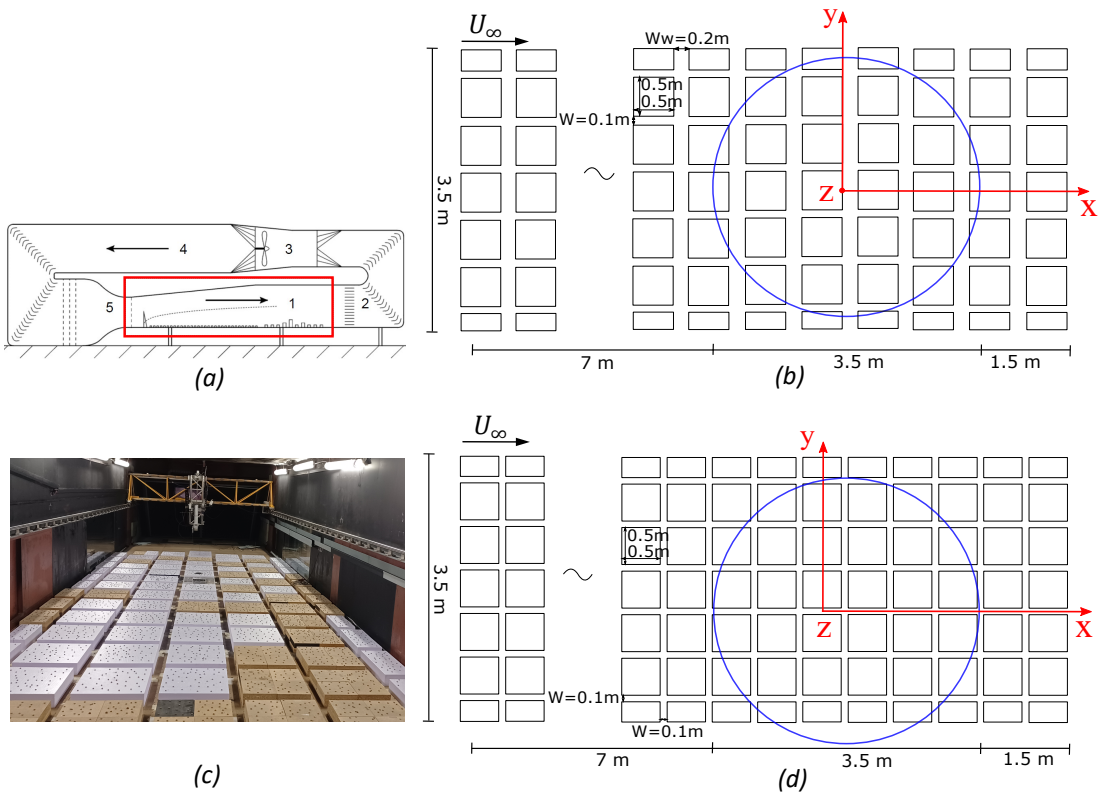


Figure 2.1 (a) Scheme of the wind tunnel: 1 test section; 2 heat exchanger system; 3 fan; 4 diverging system; 5 converging system and generating turbulence grid. The red rectangle indicates the test section. (b) Planar view of the street network reproduced inside the test section of the wind tunnel (Configuration 1). Photo (c) and planar view (d) of the regular street network reproduced inside the test section of the wind tunnel (Configuration 2).

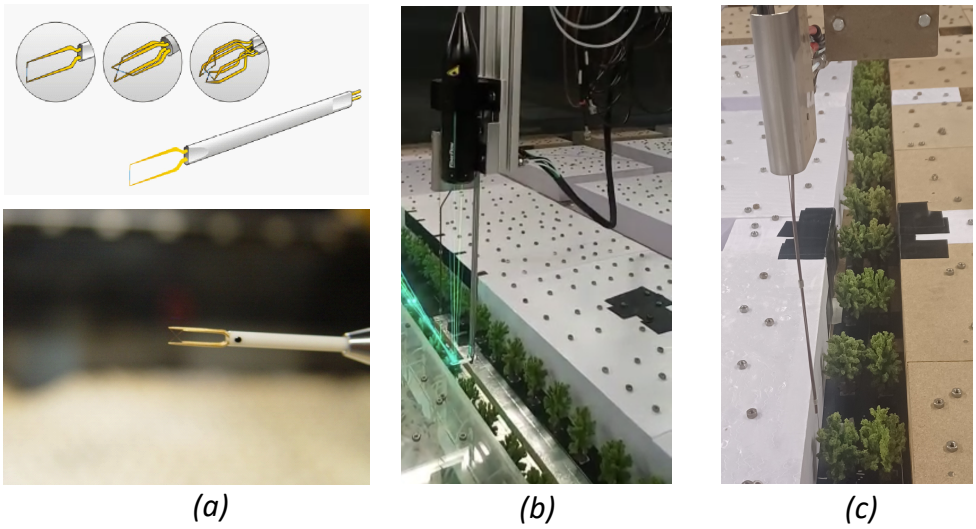


Figure 2.2 (a) Hot-Wire Anemometer. (b) System LDA-FID coupled with the mirror. (c) Flame Ionization Detector.

5 mm high steel nuts were randomly placed to reproduce the roughness of the roofs. A wind flow was generated by an axial fan, installed in the upper conduit of the recirculating wind tunnel. The turbulent flow was developed placing a homogeneous turbulent grid and a row of 7 Irwin spires at the entrance of the test section. Upwind of Configuration 1, Irwin spires 0.95 m high were used and the interaction of the wind flow with the grid, the spires and the rough blocks on the floor generates a neutrally-stratified boundary layer of depth δ_1=1.1 m and with free-stream velocity of 5 ms^{-1}. Smaller spires, 0.5 m high (raised 0.1 m above the floor) were installed in Configuration 2, generating a neutrally-stratified boundary layer of depth δ_2=0.9 m. At a distance of 7 m from the entrance of the test section, a rotating platform with a diameter of 3.5 m is mounted on the floor, to allow the wind direction to be studied (blue circle in panels 2.1b and 2.1d). The x-, y-, and z-axes of the reference system are oriented in the streamwise, transversal, and vertical directions of the wind tunnel, respectively. Traffic pollution was simulated placing linear and point sources at ground level, emitting ethane, which behaves as a passive scalar.

2.2 Measuring instruments

2.2.1 Hot-Wire Anemometer

The Hot-Wire Anemometer (HWA) is an instrument to measure the flow velocity, equipped with a X-wire probe with an acceptance angle of ±45°, allowing for the simultaneous measurement of two velocity components (Fig. 2.2a). The platinum probe wire is 1 mm long and with a diameter of 5 μm. The instrument was calibrated by comparison with a Pitot tube. Notably, we related, with a fourth order polynomial (in accordance with the King's law), the current, measured with the HWA, required to maintain the temperature of the wire invested by the local flow constant, and the flow velocity, measured with the Pitot tube. In addition, we placed a type K thermocouple close to the probe wire, to constantly monitor the temperature. A 2-minutes acquisition time at a frequency of 5000 Hz ensure good convergence of the velocity statistics – notably, the uncertainties in the convergence of the mean and standard deviation of the velocity signals are smaller than 0.1% and 2%, respectively – and well-resolved power spectra. The HWA was used to characterise the boundary layer above the obstacles.

2.2.2 Laser Doppler Anemometer

The Laser Doppler Anemometer (LDA) Argon class IV is an instrument suitable to measure the flow velocity within recirculating flow region. This instrument is equipped with a 5 W power laser, emitting two blue and two green beams with wavelengths λ_{blue}=488 nm and λ_{green}=514.5 nm, respectively. The beams have a diameter of 0.1 mm and the LDA focal length is 400 mm. The point of intersection of the four beams determines the measuring volume. In dual-beam configuration, the LDA provides the module and the direction of two velocity components simultaneously, notably the streamwise and the transversal component. To measure vertical velocity component, the LDA is coupled with a mirror, which deflects the laser beams (see Fig. 2.2b). The flow was seeded with the fluid SAFEX®-Inside-Nebelfluid Dräger Spezial W, emitting droplets with dimensions in the range 0.5-2 μm. The LDA was used to characterise the flow field inside the street canyon and to repeat the characterisation of the boundary

layer above the obstacles. In Appendix E, we report the comparison of flow velocity statistics measured with HWA e LDA. The profiles are essentially the same, a part from those of Reynolds stresses, since the LDA provides a measure of them more precise than HWA in turbulent boundary layers (Marro et al., 2020). To achieve a good convergence of the statistics of the velocity signal, we maintained a data rate between 800 and 2000 Hz – notably, the data rate tends to decrease towards the canyon floor, due to lower seeding –, setting a sampling time sufficiently long to collect at least 150000 values for each measuring point. These data rate and sampling frequency guarantee that the convergence of the mean and the standard deviation of the velocity signals has uncertainties smaller than 2% and that of skewness and kurtosis smaller than 5%. During the acquisition, the power of the blue and the green beams was set at 800 mW.

2.2.3 Flame Ionization Detector

The scalar concentration was measured using a Flame Ionization Detector model HFR400 (reported in Fig. 2.2c), suitable to measure hydrocarbon concentration time series. The instrument is equipped with a sampling capillary tube 0.3 m long, $1.27 \cdot 10^{-4}$ m inner radius, and imposed pressure drop of 33330.6 Pa, guaranteeing a frequency response of about 800 Hz (Nironi et al., 2015). The FID works in the range 0-10 V, and it detects concentration values in the range 0-5000 ppm, with a precision of about 1-2 ppm. The relation between the electric potential measured by the FID and the concentration in ppm is a linear function, whose slope coefficient is calculated by calibrating the instrument at the beginning and at the end of each measurement session (Marro et al., 2020). A variation of $\pm 3\%$ of the coefficient is accepted, as the instrument is sensitive to ambient conditions. Since the wind tunnel is a recirculating system, the background concentration increases with time. Thus, a linearly interpolated value of the background concentration recorded at the beginning and at the end of each measurement is subtracted from the concentration signals. The measurements were performed setting a constant sampling frequency of 1000 Hz and an acquisition time of 120 s. Analysing concentration signals, we verified that the acquisition time is enough long to guarantee a good convergence of the mean and standard deviation of the concentration.

2.3 Aerodynamic characterisation of the model trees

The urban vegetation was simulated through plastic miniatures of trees, with a trunk of 2 cm and a porous crown, made of plastic filaments, 6.5 cm high and 4.5 cm wide. In a 1:200 scale, the miniatures represent trees 16 m high and 9 m wide, similar to plane trees or hypochestnuts, typically planted in tree-lined boulevards located in urban canyons flanked by buildings 20 m high. The aerodynamic behavior of the model trees was characterized measuring their aerodynamic porosity and drag coefficient (Fellini et al., 2022). The aerodynamic porosity is the ratio between the spatial average wind speed downstream the obstacle and the average speed of the approaching wind. It was evaluated performing velocity measurements on a dense grid upstream and downstream a single tree, placed in a homogeneous flow. The velocity field was integrated over the tree silhouette, obtaining an aerodynamic porosity equal to 0.3, which approximates the porosity of a real tree (Manickathan et al., 2018) and is consistent with the value of the optical porosity computed with image processing. The drag coefficient was estimated as $2F_d/\rho_a U_{ref}^2 A_c$, where F_d is the drag force measured by means of a load cell, ρ_a the air density (around 1.18 kgm^{-3} at 25 °C), U_{ref} the velocity of the approaching wind measured using the Pitot tube, and A_c the projected frontal area of the tree. Increasing U_{ref}, the drag coefficient converges to a constant value equal to 0.65, which is in line with the drag coefficient of a real tree (Manickathan et al., 2018), for Reynolds numbers based on the tree ($Re_t = U_{ref} H_T/\nu$, where H_T is the tree height) greater than 10^4. Note that the miniatures do not have leaves distinct from the branches and this prevents us from evaluating a real leaf area density In this work, the model trees are inserted along the long sides of a street canyon, arranged according to three different configurations: no trees inside the canyon (Zero), two parallel rows of trees spaced 14 cm apart (Half) and two parallel rows of trees spaced by 7 cm (Full).

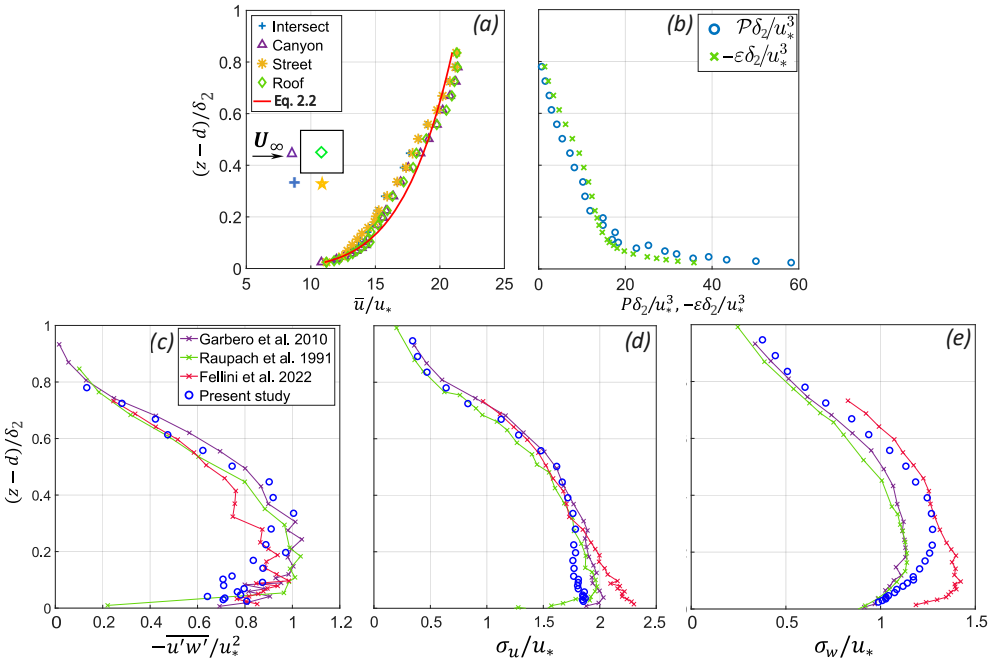


Figure 2.3 (a) Vertical profiles of the mean longitudinal velocity, measured at four different positions around an obstacle (the white square represents an obstacle and the symbols around it indicate the positions). The red line represents the power law defined by Eq. 2.2. (b) Production and dissipation of t.k.e.. Comparison of the Reynolds stresses (c), longitudinal velocity standard deviation (d), and vertical velocity standard deviation (e), measured above the obstacles, with Raupach et al. (1991), Garbero et al. (2010), and Fellini et al. (2022). The vertical profiles from Garbero et al. (2010), Fellini et al. (2022), and from the present study are obtained as average over four different positions around an obstacle.

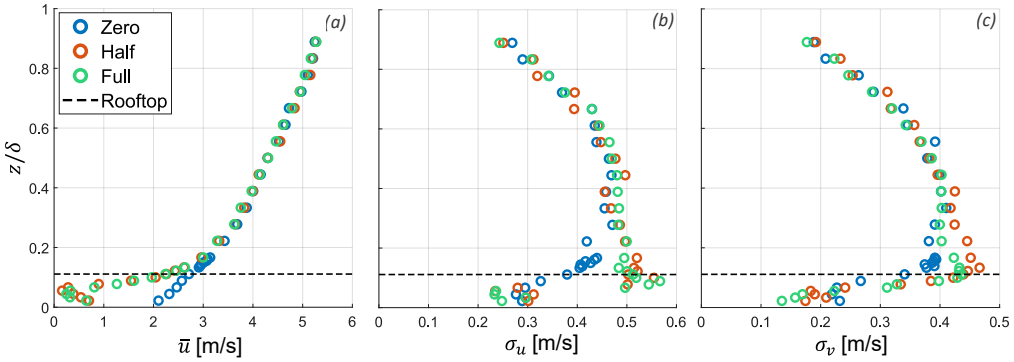


Figure 2.4 Vertical profiles of the mean longitudinal velocity (a), longitudinal velocity standard deviation (b), and transversal velocity standard deviation (c), measured within and above a streamwise street, along the vertical axis (at y/H=0). The different colors (blue, orange, and green) indicate different tree densities reproduced within the street (Zero, Half, and Full configurations).

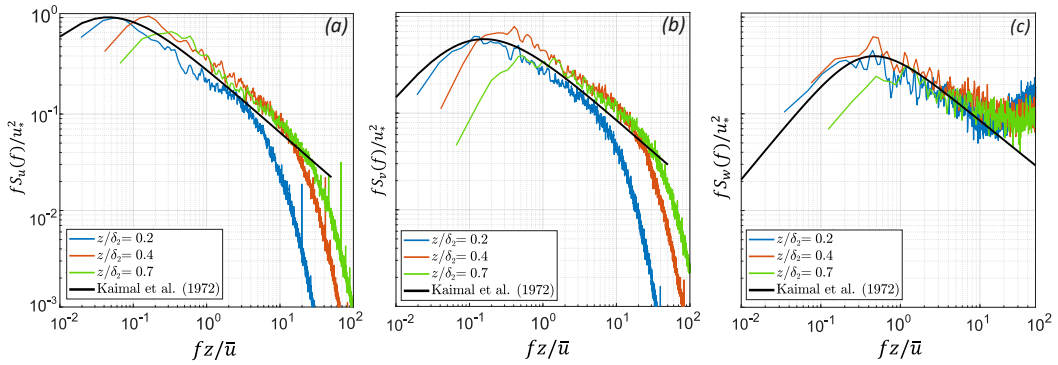


Figure 2.5 Velocity spectra of the streamwise velocity (a), transversal velocity (b), and vertical velocity fluctuations (c), calculated above the obstacles, at different positions along the z-axis. The empirical spectra $S_u(f)$, $S_v(f)$, and $S_w(f)$ are compared with the model by Kaimal et al. (1972), extrapolated from field data and represented with a black line.

2.4 Boundary layer above buildings

In this section, we characterise the boundary layer developing above the urban canopy, analysing flow velocity statistics measured above the blocks. This characterization serves to demonstrate the Reynolds independence of the turbulent flow, the spatial homogeneity of the boundary layer above the reference canyon and its similarity with typical urban boundary layers, and to provide the parameters required for numerical modeling. The boundary layer developed above the obstacle Configuration 1 was characterised by Fellini et al. (2022), thus first, we present the complete characterisation of the boundary layer above Configuration 2 and then we recall only the main characteristics of that above Configuration 1.

The boundary layer above the obstacle Configuration 2 is $\delta_2 = 0.9$ m high and it has free-stream velocity equal to around $U_\infty = 5$ ms^{-1}. The characteristic Reynolds number of the flow is $Re_\delta = \delta_2 U_\infty/\nu \simeq 2.9 \cdot 10^5$ (where $\nu \sim 1.52 \cdot 10^{-5}$ m^{2}s^{-1} is the kinematic viscosity of the air at 19 °C) and the Reynolds numbers based on the obstacle height are equal to $Re_\infty = HU_\infty/\nu \simeq 3.3 \cdot 10^4$ and $Re_H = H\overline{u}_H/\nu \simeq 2 \cdot 10^4$, being $\overline{u}_H$ the mean streamwise velocity at $z = H$. In a square canyon perpendicular to the external flow, the Reynolds independence condition is reached for $Re_\infty > 13,000$ according to Allegrini et al. (2013) and for $Re_H > 3400$ according to Marucci and Carpentieri (2019). Additionally, Lin et al. (2021) reported that the criterion $Re_H > 11,000$, set by

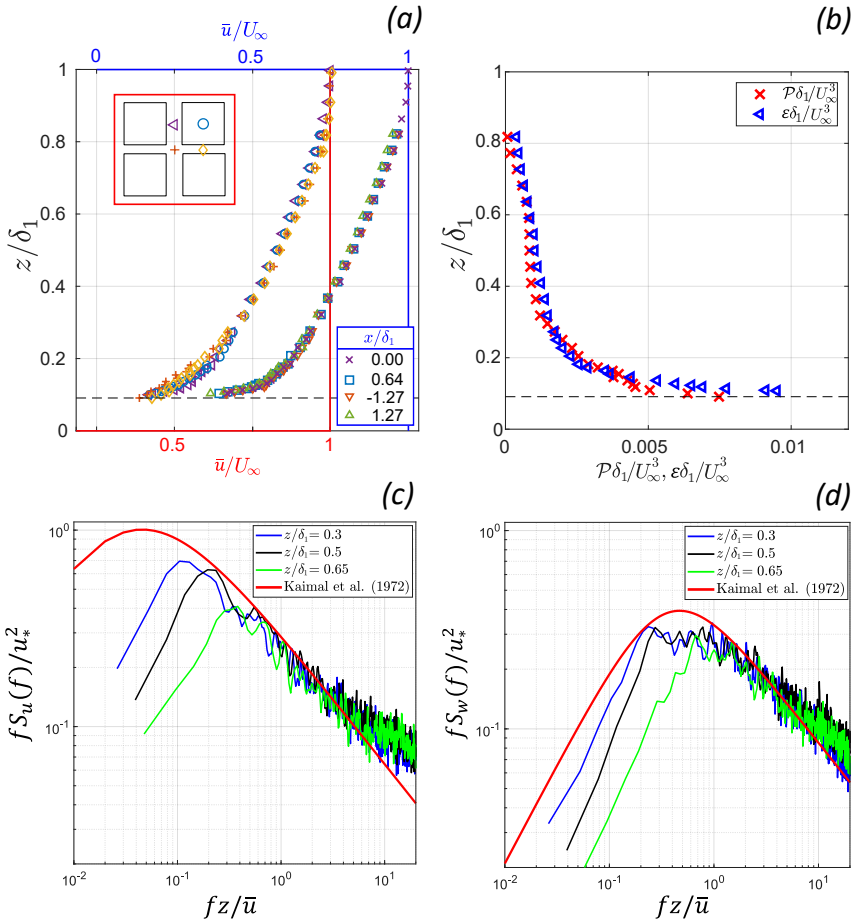


Figure 2.6 (a) Streamwise mean velocity profiles at the top of the building-like obstacles of (black dashed line) of Configuration 1, measured at 4 different positions around a building-like-obstacle (red bottom x-axis) and at 4 different distances along the streamwise direction of the wind tunnel (blue top x-axis). (b) Production and dissipation rate of turbulent kinetic energy. Panels (a) and (b) are taken from Fellini et al. (2022). Velocity spectra of the streamwise velocity (c) and vertical velocity fluctuations (d), calculated above the obstacles, at different positions along the z-axis. The empirical spectra $S_u(f)$, $S_v(f)$, and $S_w(f)$ are compared with the model by Kaimal et al. (1972), extrapolated from field data and represented with a red line.

Snyder (1972), holds for canyons with $H/W < 2.4$. Based on these findings, the values of Re_∞ and Re_H in the present experiment can be considered sufficiently high to ensure a Reynolds-independent flow structure.

We characterised the boundary layer flow measuring vertical profiles of flow velocity statistics above the obstacles, in different longitudinal and transversal positions in the wind tunnel. In Fig. 2.3a, we show vertical profiles of the mean streamwise velocity ($\overline{u}$) acquired in four different locations around an obstacle: on the rooftop (Roof), above a streamwise street (Street), above a spanwise street (Canyon), and above a street intersection (Intersect). These profiles were measured at a distance $10\delta_2$ downstream the entrance of the test section, where the combined effect of the wake of the vortex generators and of the obstacle array placed at the ground has reasonably reached an equilibrium condition (Salizzoni et al., 2008). We can therefore consider that, above the so-called *blending height*, the velocity field can be considered as homogeneous in the horizontal plane. This is indeed confirmed by the overlapping between the profiles above the reference canyon, the perpendicular street, the intersection between the two and above a roof (see Fig. 2.3a). Note that we measured vertical profiles of $\overline{u}$ and of the standard deviation of the longitudinal (σ_u) and transversal (σ_v) velocity adding different tree densities inside the streamwise street (Fig. 2.4) and we found that, outside the street, these profiles maintain the same shape of those measured above the empty canyon, demonstrating that the presence of trees has not significant effects on the turbulent flow above the obstacles. The mean longitudinal velocity at the top of the boundary layer $\overline{u}(x = \delta_2)$ measured at different longitudinal positions in the range $-1.6 < x/\delta_2 < 2$ shows slight variations, with gradients in the range $0.01 < dU_\infty/dx < 0.04$ s^{-1}.

More in detail, the lower part of the boundary layer is divided into two regions: the roughness sub-layer (below the blending height), where the flow is affected by the wakes of each single block, and the inertial sub-layer, where the flow statistics depend instead on the vertical coordinate, only. In the inertial region, the vertical profile of the mean streamwise velocity can be modeled by a logarithmic profile

$$\overline{u}(z) = \frac{u_*}{\kappa} \ln\Big(\frac{z-d}{z_0}\Big), \tag{2.1}$$

where u_* is the friction velocity, $\kappa \approx 0.4$ is the von Kárman constant, d is the zero-plane displacement length, and z_0 is the aerodynamic roughness length.

We estimated u_* from the relation $u_*^2 = -\overline{u'w'}$ (Tritton, 2012), therefore we explored the profile of $\overline{u'w'}/u_*^2$ in the range $0.22 \leq z/\delta_2 \leq 0.55$ ($2 \leq z/H \leq 5$), to find the region where $\overline{u'w'}/u_*^2$ varies around 1. We found this region in the range $0.25 \leq z/\delta_2 \leq 0.44$ ($2.25 \leq z/H \leq 4$), which is a plausible extent of the inertial layer, where the Reynolds stresses profile varies around a constant value. The parameters d and z_0 were estimated by least square fitting of Eq. 2.1 to the experimental $\overline{u}$ data in the inertial layer, with the value of u_* fixed (Salizzoni et al., 2008). We obtained $u_*/U_\infty = 0.047$ ($u_* = 0.25$ ms^{-1}), $d/\delta_2 = 0.11$ (d=0.098 m), and $z_0/\delta_2 = 4.3 \cdot 10^{-4}$ ($z_0 = 3.9 \cdot 10^{-4}$ m). Note that the estimated values of d/H and z_0/H are in agreement with the empirical relation based on morphometrical parameters proposed by Grimmond and Oke (1999). The mean velocity throughout the whole boundary layer depth can be instead modeled by a power law of the form (see red curve in Fig. 2.3a)

$$\overline{u}(z) = U_\infty \Big(\frac{z-d}{\delta_2 - d} \Big)^n, \tag{2.2}$$

with an exponent $n = 0.18$ providing the best-fit the the experimental data.

In Fig. 2.3b, we present the profiles of turbulent kinetic energy (t.k.e.) production and dissipation. The t.k.e. dissipation was evaluated as $\varepsilon = \dfrac{15\nu}{\overline{u}} \overline{\Big(\dfrac{\partial u'}{\partial t} \Big)^2}$, i.e. assuming local isotropy and adopting Taylor's hypothesis of frozen turbulence (Hinze, 1967). The temporal derivative of $u'(t)$ was obtained from the velocity time series. The t.k.e. production was calculated as $\mathcal{P} = -\overline{u'w'} \dfrac{\partial \overline{u}}{\partial z}$, using the vertical profiles of $\overline{u}$ and $\overline{u'w'}$. The strong overlap between the two quantities indicates that, to a first approximation, the flow can be considered in local equilibrium, which is characteristic of boundary layer flows (Tennekes and Lumley, 1972).

Panels 2.3c-2.3e show vertical profiles of Reynolds stresses, and longitudinal and vertical (σ_w) velocity standard deviation. These quantities, normalised by u_*, are compared to the reference profiles obtained by Raupach et al. (1991) and to the experimental profiles obtained by Garbero et al. (2010) and Fellini et al. (2022). The latter are the profiles measured above the obstacle Configuration 1. The $\overline{u'w'}$ and σ_u profiles agree well with the ones of the previous studies, even if there are discrepancies in the lowest part of the σ_u/u_* profiles (see panel 2.3d), due to the sensitivity to the roughness geometry and the experimental

conditions (Raupach et al., 1991). Conversely, σ_w/u_* profiles (panel 2.3e) show significant difference one from the others, depending on the geometry of the building array. As pointed out by Krogstadt and Antonia (1999), this greater sensitivity of the vertical velocity fluctuations on the geometry of the wall is expected and has been previously observed for a variety of configurations of roughness elements.

Finally, in Fig. 2.5, we report the pre-multiplied spectra of the three components of velocity fluctuations – $u'(t)$, $v'(t)$, and $w'(t)$ –, calculated at increasing vertical distances from the obstacles. The power spectral density was evaluated applying the Welch method, to obtain well-resolved spectra. The velocity signals were re-sampled with a regular frequency of 5000 Hz and divided into 3000 windows, each filtered with the Hamming filter. The spectra, normalised by u_* and plotted against the non-dimensional frequency $f_{ad} = fz/\overline{u}$ (where z is the position along the z-axis where the spectra were calculated and $\overline{u}$ is the local mean longitudinal velocity), are compared to the empirical relations by Kaimal et al. (1972),

$$\frac{fS_u(f)}{u_*^2} = \frac{102 f_{ad}}{(1+33 f_{ad})^{5/3}}, \quad \frac{fS_v(f)}{u_*^2} = \frac{17 f_{ad}}{(1+9.5 f_{ad})^{5/3}}, \quad \frac{fS_w(f)}{u_*^2} = \frac{2.1 f_{ad}}{1+5.3 f_{ad}^{5/3}}, \tag{2.3}$$

obtained by fitting field measurements. We observe a strong overlap in both the production and inertial frequency ranges, indicating that the spectral energy distribution in the boundary layer developed during this experiment closely resembles that of a real atmospheric boundary layer.

The turbulent flow above the obstacle Configuration 1 is $\delta_1 = 1.1$ m high and it is characterised by a Reynolds number of the flow $Re_\delta = \delta_1 U_\infty/\nu \simeq 3.6 \cdot 10^5$ (where U_∞ is around 5 ms^{-1}), which guarantees Reynolds independent flow dynamics (Allegrini et al., 2013; Marucci and Carpentieri, 2019). In Fig. 2.6a, we report the four vertical profiles of $\overline{u}$ measured at different positions around a building-like-obstacle and at different streamwise distances from the entrance of the test section. The vertical profiles collapse onto a single curve, meaning that the external boundary layer has reasonably reached an equilibrium condition. Consistently, the production ($\mathcal{P}$) and dissipation (ε) of turbulent kinetic energy overlap throughout the whole boundary layer (Fig. 2.6b). In the inertial layer of the boundary layer – defined in the range $0.15 < z/\delta_1 < 0.4$ (Fellini et al.,

2022)) –, the mean velocity profile is well fitted by the logarithmic profile (2.1), whose parameter are equal to u_*=0.29 ms^{-1}, d=0.094 m, and $z_0 = 1 \cdot 10^{-3}$ m. Note that the ratio u_*/U_∞ is around 0.05 in both obstacle Configurations 1 and 2, consistently with previous studies simulating similar urban geometries (Salizzoni et al., 2008; Garbero et al., 2010). The spectra of the streamwise velocity signal ($u(t)$) and of the vertical velocity signal ($w(t)$) for increasing distances from the obstacles, are reported on panels 2.6c and 2.6d. We found a good agreement between the measured spectra and the Kaimal et al. (1972) model (Eqs. 2.3) in the inertial region.

Chapter 3

Turbulent fluctuations and transport processes in a canyon perpendicular to the external flow

The work described in this chapter has been partially derived from Del Ponte et al. (2024).

This chapter focuses on the analysis of the effect of tree density on turbulent flow and concentration fields within a canyon perpendicular to the external wind flow. The work by Fellini et al. (2022) presented the results of an experimental campaign aimed at providing a high-resolution three-dimensional characterization of the mean scalar concentration field inside a vegetated street canyon, perpendicular to the wind flow. They found that different spatial patterns of the mean concentration emerge depending on the tree density. Moreover, the presence of trees increases the pollutant concentration at the upwind wall, mostly at the pedestrian level, even if it does not affect significantly the average concentration calculated over the whole canyon. The work presented in this chapter was aimed at extending this investigation to the estimation of the turbulent mass fluxes, within the canyon, which drive the transfer of pollutant towards the external atmosphere.

The issue of the turbulent (mass and momentum) transfer between the external flow and a plant (Raupach et al., 1996; Finnigan, 2000) or urban (Garbero et al., 2010; Neophytou et al., 2014; Perret et al., 2019) canopy has

been so far addressed by a large number of authors. On one side, studies on plant canopies were conducted adopting idealised (Raupach et al., 1986; Poggi et al., 2006) or (more rarely) realistic (Pietri et al., 2009) modeled trees, focusing on the role of vegetation density (Poggi et al., 2004) and terrain morphology (Poggi and Katul, 2007a,b). On the other side, most studies on the urban canopy considered simplified urban geometries, focusing on the effect of the canyon height-to-width ratio (H/W_c, where H is the height of the canyon and W_c is its width) (Di Bernardino et al., 2015, 2018; Jaroslawski et al., 2020), upstream turbulence (Salizzoni et al., 2011; Blackman et al., 2015, 2018) and thermal fluxes (Marucci and Carpentieri, 2019; Fellini et al., 2020) on the street canyon ventilation.

Studies focusing on the combined effect of both trees and building density on turbulence dynamics are however still missing. To do a step forward to fill this gap, we present an experimental characterization of flow (Sect. 3.2.1) and concentration fields (Sect. 3.2.2) and vertical mass fluxes (Sect. 3.2.3), within and above a street canyon, considering different vegetation densities. In Sect. 3.2.2 we provide a probabilistic characterization of concentration fluctuations, with a focus on extreme values, which have important applications in toxic risk analysis. Conclusions of this chapter are drawn in Sect. 3.3.

3.1 Experimental details

The reference street canyon is a closed cavity L=1 m long, H=0.1 m high, W_w=0.2 m wide, within which the scalar ground-level line source is placed. It is subject to the neutrally-stratified boundary layer developed above the obstacle Configuration 1 (see Fig. 2.1b). We adopted a canyon with lateral edges bordered by walls in order to avoid lateral mass fluxes and to define a control volume for the rigorous estimation of the ventilation efficiency, performing a mass balance between the mass flux emitted by the line source and the mass flux leaving the canyon at the rooftop. The geometry of the street canyon provides an aspect ratio H/W_w=0.5 and a length to height ratio L/H=10, which approximates the characteristics of an indefinitely long canyon (Salizzoni et al., 2009; Allegrini et al., 2013). The canyon is around 9 m away from the entrance of the test section of the wind tunnel, and it is oriented perpendicular

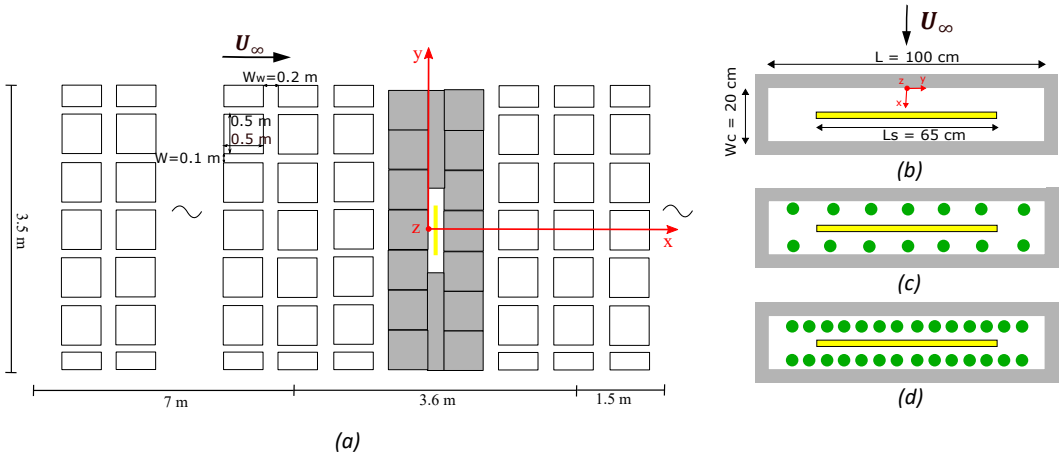


Figure 3.1 (a) Scheme of the urban network reproduced inside the test section of the wind tunnel. The blocks confining the reference canyon are coloured grey (b) Reference street canyon in the Zero (b), Half (c), and Full (d) configurations. The yellow line represents the linear source, while the green dots are the model trees.

to the wind flow direction. The ground-level linear source (simulating traffic pollutant emissions) is L_s=0.65 m long, thus it does not cover the entire length of the canyon (see yellow line in Fig. 3.1), in order to avoid wall effects. It consists of a metallic tube pierced with needles emitting an ethane-air mixture within a homogenization chamber, located in a slot cut in the floor of the wind tunnel. From this chamber, the gas mixture is injected in the canyon, at ground level, through a metallic grid 65 cm long and 1 cm wide. The small holes of the grid produce substantial pressure drop thus rendering the gas flow in the street canyon insensitive to local pressure fluctuations. The injection flow rate is 4 l/min, allowing an emission velocity (equal to 0.01 ms^{-1}) sufficiently low to avoid flow perturbation in the cavity (Marro et al., 2020). Ethane was chosen as a passive tracer since it has a density similar to air. The origin of the reference system was assumed in the middle of the street canyon, at the upwind wall (see red arrows in Fig. 3.1a,b), with the x-coordinate oriented in the streamwise direction, the y-coordinate oriented along the canyon axis and the z-coordinate oriented upward.

The aerodynamic effect of trees was simulated using plastic miniatures of trees (described in Sect. 2.3) arranged according to three different configurations: no trees inside the canyon (Zero, Fig. 3.1b), two parallel rows of seven trees

spaced 14 cm apart (Half, Fig. 3.1c) and two parallel rows of fourteen trees spaced by 7 cm (Full, Fig. 3.1d).

We used the LDA technique, to measure the streamwise (u), transversal (v), and vertical (w) components of the velocity field. As detailed below, we first measured simultaneously u and v inside the canyon only, then we coupled a mirror to the LDA to measure u and w both inside the canyon and at the roof level (a detailed description of this method is available in Sect. 2.2.2). In a third measuring session, the system LDA-mirror was coupled with a FID to measure vertical turbulent mass fluxes, both inside the canyon and at the rooftop. The concentration field was measured with high spatial resolution by means of the FID alone (Fellini et al., 2022). In the present work, we extract from that dataset a two-dimensional vertical section in the centre of the canyon (x/H=1), and a two-dimensional horizontal section at the rooftop (z/H=1). Moreover, to collect more samples for the investigation of the probability density function of the concentration, we extended the acquisition time to 300 s for a limited number of sampling points located along a longitudinal profile in the center of the canyon (x and z coordinates were fixed at x/H=1 and z/H=0.4, respectively). In the vegetated canyon configurations, a higher number of sampling points were measured, to capture the heterogeneity of the mean concentration profiles.

3.1.1 Turbulent mass fluxes measurements

The turbulent vertical mass fluxes are evaluated as the cross-correlation between concentration fluctuations and velocity fluctuations, $c'(t)$ and $w'(t)$, respectively. Instantaneous fluctuations are defined as $c'(t) = c(t) - \overline{c}$ and $w'(t) = w(t) - \overline{w}$ respectively, where $c(t)$ is the concentration time series with the background concentration removed (see Sects. 2.2.3), $w(t)$ is the vertical velocity time series, $\overline{c}$ and $\overline{w}$ are their mean, and t is the time. The estimate of cross-correlation requires concentration and velocity to be measured simultaneously, in the same control volume. This can be achieved by coupling the FID and the LDA (Fig. 2.2b).

The installation of the LDA-FID system and the evaluation of the cross-correlation were performed following the approaches and methods provided

by Marro et al. (2020). The distance between the measuring volume of the LDA and the sampling tube of the FID was set at 4 mm, as it is the optimal distance to avoid flow disturbances caused by the FID and to guarantee that concentration and velocity measurements refer to the same fluid elements. In this setup, the time delay between the two signals (Δt_{lag}), due to the travel of the particles across the sampling tube (see Sect. 2.2.3), was estimated to be 0.016 s (Marro et al., 2020). The cross-correlation between velocity and concentration fluctuations ($\overline{w'c'}$) was computed using the sample-and-hold reconstruction and resampling (S+H) method (Kukačka et al., 2012; Marucci and Carpentieri, 2019). Notably, the concentration signal was shifted by Δt_{lag}, and resampled on the irregular sampling frequency of $w(t)$, using the nearest neighbor interpolation since the correspondence between velocity and concentration data was missing. This method is reliable in this application, as it provides results with less than 6% difference from those of the well-established slot correlation method (Marro et al., 2020).

Flow velocity and turbulent mass fluxes were measured on a two-dimensional vertical grid along the longitudinal axis of the canyon (the streamwise coordinate is fixed at x/H=1) and on a horizontal grid at the rooftop (fixing the vertical coordinate at z/H=0.98). The vertical grid, being located in the centre of the canyon, is easily accessible to the experimental equipment (in particular the system LDA-FID coupled with the mirror) in both the empty and vegetated canyons, the horizontal grid, fixed 2 mm below the canyon rooftop, is used to investigate the flow field and mass transfer between the inner canyon and the external atmosphere. The vertical grid at x/H=1 is composed of five longitudinal profiles sampled at heights z/H=[0.2, 0.4, 0.6, 0.8, 0.98], whilst the horizontal section at the rooftop includes three longitudinal profiles at x/H=[0.5, 1, 1.5]. Both sections extend from y/H=–3.5 to y/H=+3.5. The longitudinal spacing of the sampling points is 50 mm in the Zero configuration, while it is irregular in the vegetated canyon configurations, due to the encumbrance of trees, and due to the fact that the mean scalar field is not homogeneous, so more points were acquired in correspondence of the mean concentration peaks (Fellini et al., 2022).

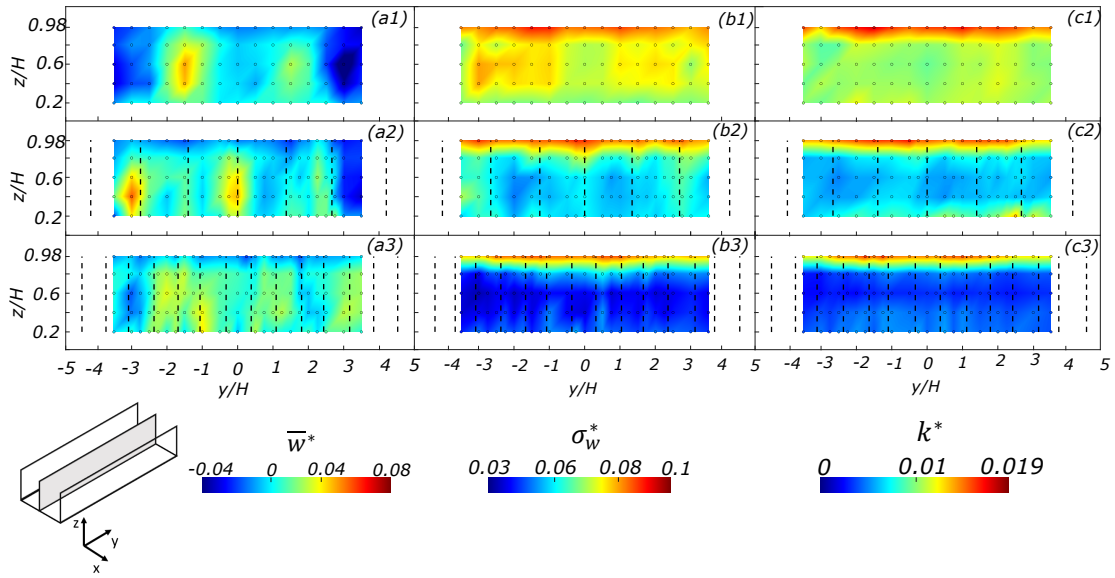


Figure 3.2 Two-dimensional sections of mean vertical velocity (a1-a3), vertical velocity standard deviation, (b1-b3) and turbulent kinetic energy (c1-c3), on the plane at x/H=1. The Zero (a1, b1, c1), Half (a2, b2, c2), and Full (a3, b3, c3) configurations are shown. Black dashed lines indicate the position of the trees. Colored circles represent the measuring points. The shaded area in the sketch shows the position of the cross-section in the canyon.

3.2 Results

In this section, we investigate the influence of tree density on the flow velocity (Fig. 3.2-3.4), concentration statistics (Fig. 3.5-3.9), and mass fluxes (Fig. 3.10-3.13). The mean and the turbulent components of all quantities are shown on vertical and horizontal sections (located at x/H=1 and z/H=0.98 or z/H=1, respectively), both obtained from linear interpolation of measured data. Moreover, using instantaneous concentration, velocity, and mass fluxes data we evaluate the concentration probability density function inside the canyon (Fig. 3.9) and the spectra of vertical velocity fluctuations and turbulent mass fluxes at the rooftop (Fig. 3.4, 3.13).

3.2.1 Flow field

As we are interested in analyzing the vertical mass transport in the street canyon, we focus here on the spatial distribution of the mean and standard deviation

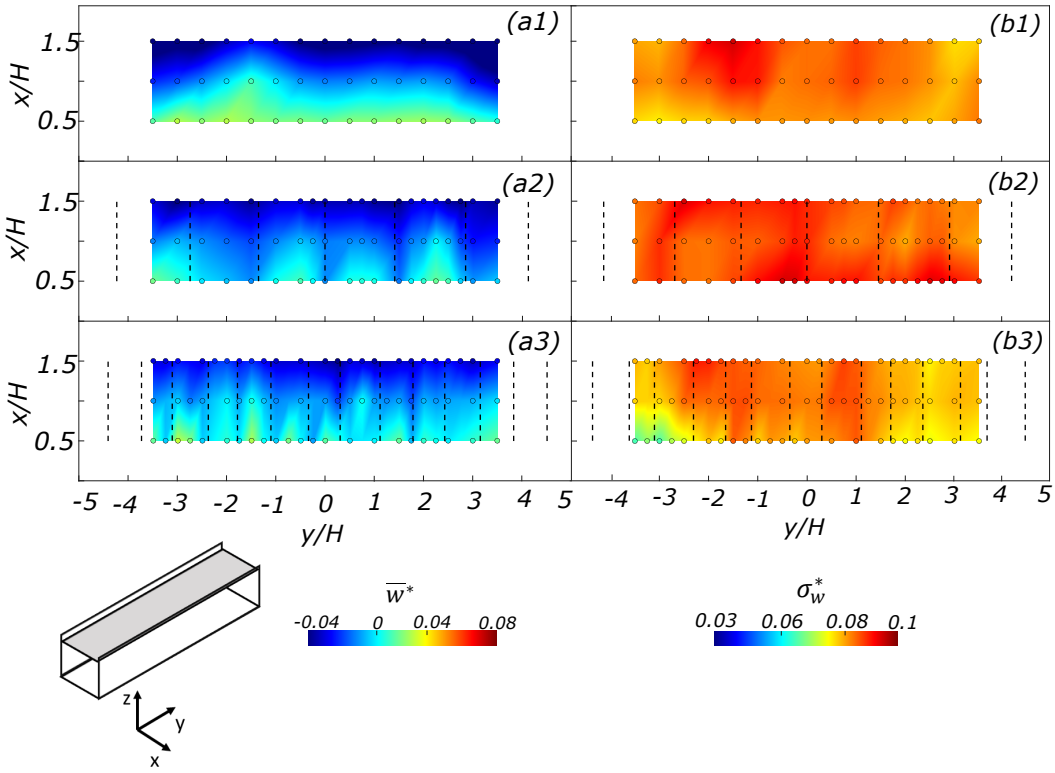


Figure 3.3 Two-dimensional sections of mean vertical velocity (a1-a3) and vertical velocity standard deviation (b1-b3), on the plane at z/H=0.98. The Zero (a1, b1), Half (a2, b2), and Full (a3, b3) configurations are shown. Black dashed lines indicate the position of the trees. Colored circles represent the measuring points. The shaded area in the sketch shows the position of the cross-section in the canyon.

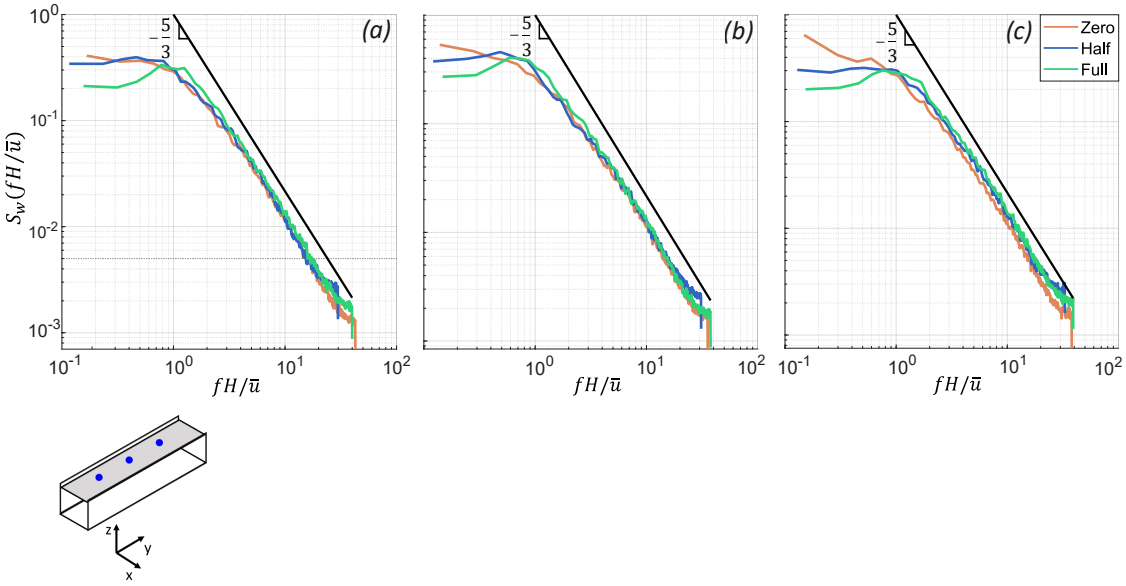


Figure 3.4 Spectra of $w'(t)$ calculated in three different sampling points along the central line (x/H=1) at the rooftop (z/H=0.98): (a) y/H=-1.5, (b) y/H=0, (c) y/H=2. The blue points on the shaded plane in the bottom inset represent the positions where the spectra were calculated.

of the vertical velocity, normalized as $(\overline{w}^*, \sigma_w^*) = (\overline{w}, \sigma_w)/U_\infty$, respectively. Positive $\overline{w}^*$ refers to upward flow and negative $\overline{w}^*$ refers to downward flow. As we mentioned in Sect. 3.1, we measured also u and v components.

Figure 3.2a1-a3 show the mean vertical velocity in the center of the canyon. In the Zero configuration (panel a1), the $\overline{w}^*$ field is organized in two symmetric zones of upward flow (around y/H=–1.5 and y/H=+1.5), and three zones of downward flow located at the edges and in the center of the canyon. The asymmetries in the upward flow regions, are due to tiny uncertainties in the arrangement of the building-like blocks (Garbero et al., 2010) and slight inclination of the external flow with respect to the wind tunnel axis (Nironi et al., 2015). Moreover, as for an aspect ratio of H/W_w=0.5 the wake interference flow regime occurs, we expect the presence of a secondary counter-rotating vortex in the upwind lower corner of the canyon (Di Bernardino et al., 2018), whose axis is not perfectly parallel to the canyon longitudinal axis. This misalignment could cause further asymmetries in the mean vertical flow along the canyon. In the Half configuration (panel a2) the succession of positive and negative zones is still present, but the spatial organization is different: we identify three zones

of positive $\overline{w}^*$ and two zones of negative $\overline{w}^*$. In the Full configuration (panel a3), positive $\overline{w}^*$ values prevail and the spatial pattern is more homogeneous. The mean flow within an urban canyon perpendicular to the external wind flow is governed by a recirculating cell (Gromke and Ruck, 2007; Fellini et al., 2022) as the external flow enters the canyon at the downwind wall and exit at the upwind wall. As a consequence, moving toward the downwind wall of the street canyon, we expect a downward flow to occur and the presence of trees to lead to a more heterogeneous pattern. Moreover, due to the recirculation we do not observe a decrease in the mean vertical velocity moving towards the ground level. The random shape, size, and orientation of the model trees produce further asymmetries, even if they are smaller than the different longitudinal patterns induced by the different tree spacing.

Conversely, vegetation does not induce peculiar spatial patterns in the vertical velocity standard deviation (Fig. 3.2b1-b3): σ_w^* remains fairly constant, both along the y and z axes, until the interface between the canyon and the external flow ($z/H = 0.98$) where it increases sharply, and it reaches the same value (about 0.08) in all configurations. On average, below the tree crowns, σ_w^* decreases with the increase in tree density: in the Full configuration, the spatial average of σ_w^* (calculated by weighting the single values by the area associated to each measurement point) is 40% lower than in the Zero configuration.

In panels c1-c3 of Fig. 3.2, we analyze the turbulent kinetic energy, estimated as $k^* = 0.5(\sigma_u^2 + \sigma_v^2 + \sigma_w^2)/U_\infty^2$. In the Zero and Full configurations (panels c1 and c3), k^* is homogeneous in the interval z/H=[0.2, 0.8]. In the Half configuration (panel c2) it is slightly heterogeneous moving along the vertical direction: higher close to the ground and lower in the interval z/H=[0.4, 0.8]. The enhanced values of k^* observed close to the ground are due to the fact that the dampening effect is mainly limited in correspondence of the tree crowns, while the large spacing between trunks allows the k^* to slightly recover the intensity it has in the empty canyon. As observed for σ_w^* (panels b1-b3), the presence of trees dampens k^*: on average, we observe a decrease of 60% between Zero and Full configurations. Moving to the rooftop of the canyon (z/H in the interval [0.8, 0.98]), we identify a sharp increase of k^*, regardless of the presence of trees. The increase of both k^* and σ_w^* reveals the presence of a shear layer of thickness $z/H \sim 0.2$, where the turbulence of the external flow is entrained in the cavity flow (Salizzoni et al., 2011; Fellini et al., 2020).

An evident imprinting of the trees can be noticed by comparing the mean vertical velocity patterns at the rooftop among the different configurations (Fig. 3.3a1-a3). In the non-vegetated canyon (panel a1), $\overline{w}^*$ has a quite homogeneous behavior along the y-axis: negative at the downwind wall, and positive at the upwind wall. Indeed the external flow enters the canyon at the downwind wall and leaves it at the upwind wall, following a recirculating flow structure (Gromke and Ruck, 2009). In the vegetated canyons, this pattern is maintained, but it is more heterogeneous at the upwind wall, as trees hinder the vertical flow motion: the upward flow occurs between adjacent trees, and its spatial periodicity increases with tree density (panels a2, a3).

On the other hand, the values of σ_w^* at the rooftop (Fig. 3.3b1-b3) are almost unaffected by the presence of trees. In the Zero and Half configurations (panels b1 and b2), σ_w^* values are almost homogeneous both in the longitudinal and streamwise directions. In the Full configuration (panel b3), some heterogeneities arise: σ_w^* decreases moving towards the edges of the canyon, mostly at the left upwind corner. In all configurations, σ_w^* values are significantly higher than the one inside the canyon.

To investigate the influence of trees on the scales of the turbulent structures involved in the energy motion at the rooftop of the canyon, we analyze the spectra of the vertical velocity signal, calculated with the Welch method. Once resampled the $w(t)$ signal at a constant sampling frequency of 1000 Hz, the Fourier transform was applied to windows of 500 samples (filtered with the Hamming filter), in order to obtain well-resolved spectra without losing information in the low-frequency range. The final spectrum is the mean of the spectra calculated in each window. In Fig. 3.4, we report the velocity spectra, calculated in three sampling points along the central profile at the rooftop of the canyon: two points in correspondence of the concentration peaks (y/H=–1.5 and y/H=2, as will be shown in section 3.2.2) and one point in the centre (y/H=0). The three different curves represent the velocity spectra (S_w) in the Zero, Half, and Full configurations, expressed as a function of the non-dimensional frequency $fH/\overline{u}$. To compare spectra in different vegetation configurations, we referred to the velocity signal normalized as $(w(t) - \overline{w})/\sigma_w$, so that the three curves have the same subtended area, equal to 1. Spectra show a decrease in the energy content of the large-scale structures (non-dimensional frequencies in the range 10^{-1}-10^{0}) when the canyon is vegetated, that are

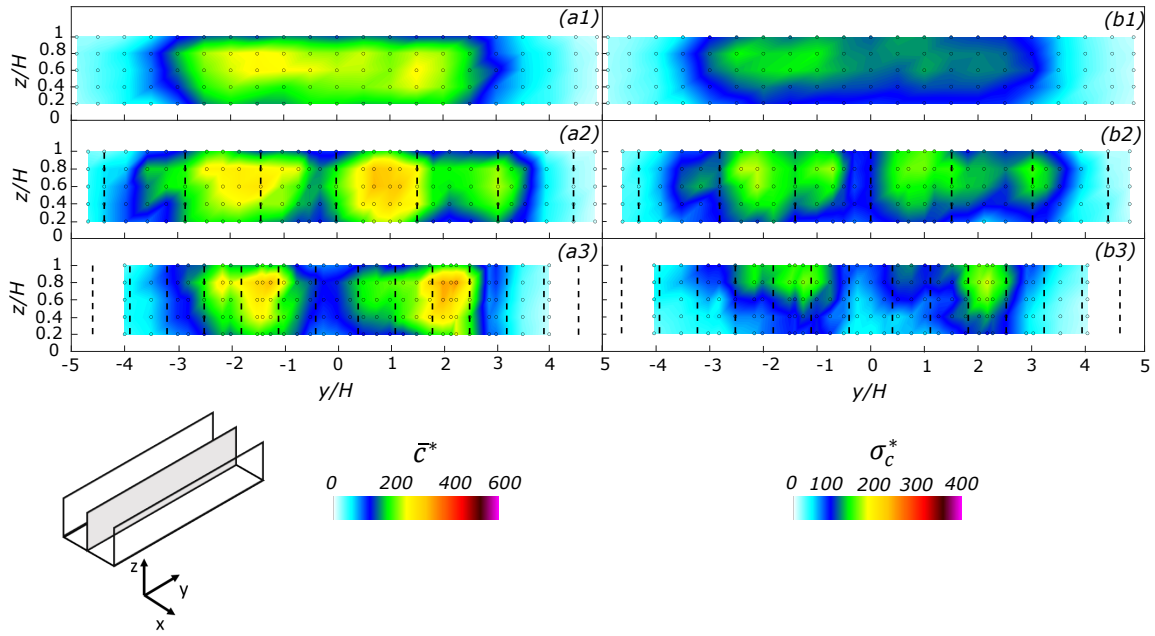


Figure 3.5 Two-dimensional sections of mean concentration (a1-a3) and concentration standard deviation (b1-b3), on the plane at x/H=1. The Zero (a1, b1), Half (a2, b2), and Full (a3, b3) configurations are shown. Black dashed lines indicate the position of the trees. Colored circles represent the measuring points. The shaded area in the sketch shows the position of the cross-section in the canyon.

likely be responsible for the reduced σ_w^* levels induced by high tree density at the canyon rooftop (pointed out in Fig. 3.3b3). The decrease in energy associated with large scales with tree density can be attributed to the fact that the characteristic length scales of turbulence are significantly influenced by the decreasing tree spacing observed in the Zero, Half, and Full configurations. Conversely, if we look at length scales of the order of magnitude smaller than the tree spacing (namely, non-dimensional frequencies larger than around 0.7 and 1.4 for the Half and Full configurations, respectively), the three curves overlap meaning that the effect of the vegetation density is no more detectable. Indeed, at intermediate scales ($fH/\overline{u} = 10^0$-10^1) the three spectra show an evident inertial region with constant slope proportional to -5/3 (the characteristic Kolmogorov inertial scaling), regardless of the tree density.

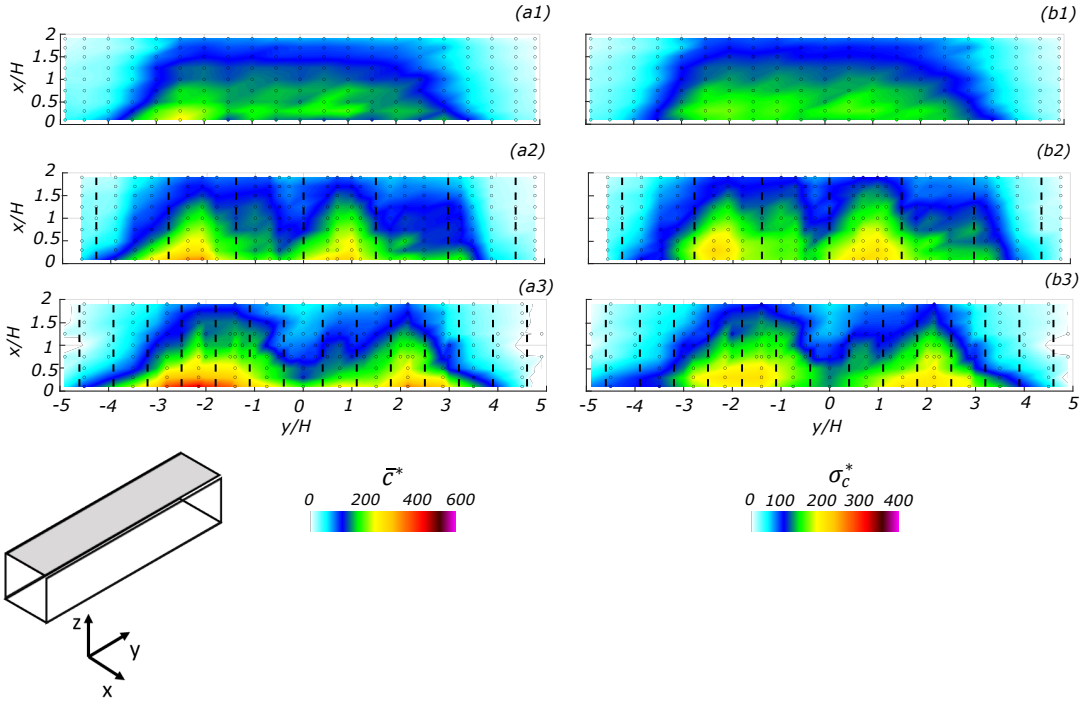


Figure 3.6 Two-dimensional sections of mean concentration (a1-a3) and concentration standard deviation (b1-b3), on the plane at z/H=1. The Zero (a1, b1), Half (a2, b2), and Full (a3, b3) configurations are shown. Black dashed lines indicate the position of the trees. Colored circles represent the measuring points. The shaded area in the sketch shows the position of the cross-section in the canyon.

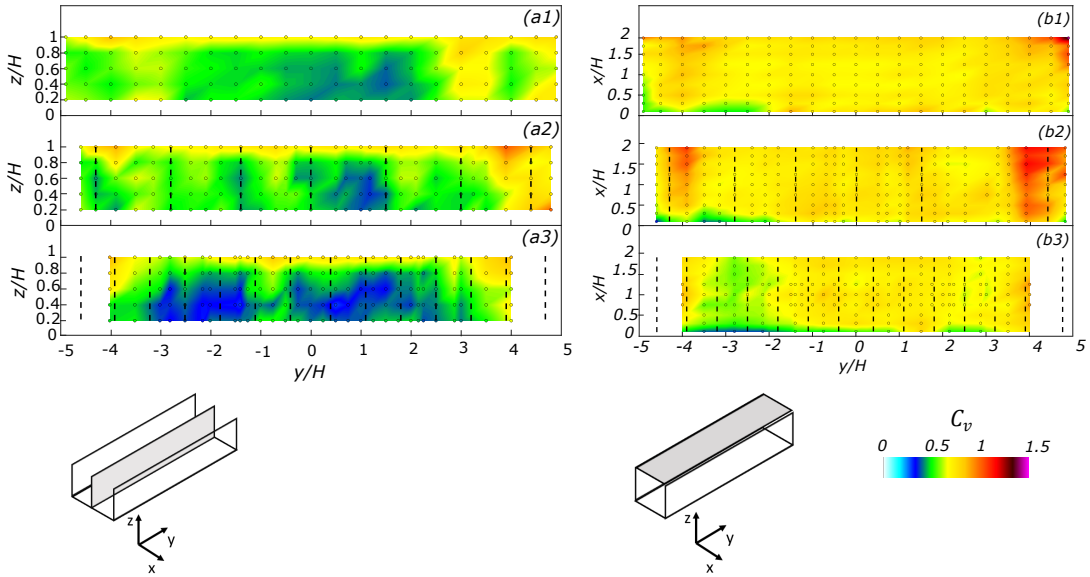


Figure 3.7 Two-dimensional sections of the coefficient of variation of the concentration on the plane at x/H=1 (left column) and z/H=0.98 (right column). The Zero (a1 and b1), Half (a2 and b2), and Full (a3 and b3) configurations are shown. Black dashed lines indicate the position of the trees. Colored circles represent the measuring points. The shaded area in the sketch shows the position of the cross-section in the canyon.

3.2.2 Concentration field

As a first step, we recall the main features of the mean concentration field (investigated in detail by Fellini et al., 2022) and, then, we analyze the concentration standard deviation and the coefficient of variation (Fig. 3.5-3.7). We use the non-dimensional form $(\overline{c}^*, \sigma_c^*) = (\overline{c}, \sigma_c)U_\infty \delta L_s / Q_{et}$, where $\overline{c}$ and σ_c are the mean and the standard deviation of the concentration time series, respectively, δ is the height of the boundary layer, L_s is the source length and Q_{et} is the ethane mass flowrate.

Inside the canyon, we notice that, in the range $y/H = [-3, 3]$, the presence of trees induces a transition from a rather homogeneous mean concentration field to a heterogeneous one (panels a1-a3 of Fig. 3.5), along the longitudinal axis. The Half configuration (panel a2) exhibits three zones of higher mean concentration, whilst the Full configuration (panel a3) is characterized by two nearly symmetric accumulation zones and a well-defined area of low concentration in the centre of the canyon: here, the concentration is approximately half the one measured in the accumulation zones. The increase in the spatial heterogeneity of pollutant concentration with tree density is in contrast with the behavior of the mean velocity field (shown in Fig. 3.2a1-a3), which tends to homogenize with the increase in tree density. Notice that, at the edges, $\overline{c}^*$ has very low values because the line source does not cover the entire length of the street canyon. Conversely, the mean concentration does not decrease going farther away from the ground-level source, as the pollutant is transported within the canyon by a recirculating structure. For a detailed analysis of the mean scalar field, see Fellini et al. (2022). The increased variability in the mean concentration field arises from the complex interaction between larger-scale motions and the smaller eddies within the canyon, which are generated by the presence of trees. Given this context, there are reservations about the suitability of relying on a single parameter, such as the bulk vertical exchange velocity (u_d), which requires averaging concentrations within the canyon, to assess the canyon's ventilation potential (the definition of the u_d parameter and its link with the ventilation potential are discussed in Chapter 6).

The standard deviation of the concentration (Fig. 3.5b1-b3) follows almost the same patterns observed for the mean concentration field: a quite homogeneous trend in the spatial range $y/H = [-3, 3]$ for the Zero configuration

(panel b1) and concentration fluctuation peaks when trees are added (panels b2 and b3). However, some differences can be pointed out: σ_c^* decreases slightly along the y-axis in the non-vegetated canyon and shows an increasing trend in the vertical direction, mostly in the correspondence of peaks in the Full configuration. Differently from σ_w^* (Fig. 3.2b1-b3), the average σ_c^* does not follow a well-defined decreasing trend with vegetation density: with respect to the Zero configuration, the spatial average of σ_c^* increases of 18% in the Half configuration and decreases of 6% in the Full configuration. However, the local maxima of σ_c^* are larger in the presence of trees (see green areas in Fig. 3.5b2,b3).

The mean concentration and the concentration standard deviation patterns are similar also at the rooftop (Fig. 3.6). Both show a clear positive gradient from the downwind wall to the upwind wall, which is almost constant along the y-axis in the non-vegetated canyon (panels a1 and b1), while it presents accumulation zones at the upwind wall in the Half and Full configurations (panels a2, b2, a3 and b3). These high concentration areas enhance the difference in $\overline{c}^*$ and σ_c^* between the two walls: in the Zero configuration, the spatial average of $\overline{c}^*$ at the upwind wall is 58% higher than the one at the downwind wall (note that this is computed by weighting the single value by the spacing between the measurement points along the profiles at x/H=0.1 and x/H=1.9, respectively), and this difference reaches 66% and 75% in the Half and Full configurations, respectively. For the concentration standard deviation, the difference between the walls is 52%, 57%, and 65% in the Zero, Half, and Full canyons, respectively. As we observed inside the canyon, the presence of vegetation increases the local maxima of σ_c^* (see yellow areas in panels b2 and b3).

In order to highlight differences between mean and standard deviation patterns, in Fig. 3.7, we investigate the spatial distribution of the coefficient of variation of the concentration, defined as $C_v = \sigma_c/\overline{c}$. As we will see in section 3.2.2, C_v is a key parameter in the analytical models for the probability density function of the scalar concentration in dispersing plumes (Orsi et al., 2021). Inside the canyon (panels a1-a3), the coefficient of variation shows very similar spatial distributions in the Zero and Half configurations, with lower values close to the centre (blue region) and increasing values moving toward the lateral edges of the canyon. Here, the mean and the fluctuating component of the

concentration are very low, as there is no scalar emission from the source, thus the evaluation of C_v is affected by large uncertainty. In the Full configuration (panel a3), we observe two regions characterized by weak C_v values, leading to an average decrease of 11% with respect to the Zero configuration. The vegetation-induced transition from a homogeneous field to a heterogeneous one is not as pronounced as for $\overline{c}^*$ and σ_c^* fields, where we observed local differences up to 50% in the Full configuration (see Fig. 3.5a3,b3), however, the high tree density slightly dampens the concentration fluctuations around the mean, leading to a more heterogeneous pattern with respect to Zero and Half configurations.

At the rooftop (panels b1-b3), C_v is almost homogeneous in all configurations, and 40% larger than within the canyon. However, some heterogeneities appear: higher C_v values at the edges of the canyon and an area of lower C_v around $y/H = -3$ in the Full configurations. Again, the heterogeneities are linked to the uncertainty in the C_v estimate due to the low concentration measured laterally.

Concentration probability density function

The characterization of the probability density function (pdf) of pollutant concentration has several applications including the evaluation of the health risks related to the exposure to high levels of toxic substances, odors assessment, or the estimation of the upcrossing probability. Indeed, these questions require the knowledge of the occurrence probability of instantaneous concentration values above critical thresholds, and, therefore, information about the pdf. Previous studies investigated the pdf of concentration fluctuations arising from localised releases in the atmospheric boundary layer (see the review of Cassiani et al., 2020). Nironi et al. (2015) carried out measurements of concentration fluctuations inside a plume released by a point source, considering different source sizes and elevations. They found that the empirical pdf changes shape with distance from the source, and is well modeled by a gamma distribution. Other studies report that the lognormal distribution is a suitable model for plume dispersion in neutral boundary layers (Yassin, 2008; Finn et al., 2010), while the two- and three-parameter Weibull distributions provide analytical formulations to estimate the percentiles of the concentration, who have important applications

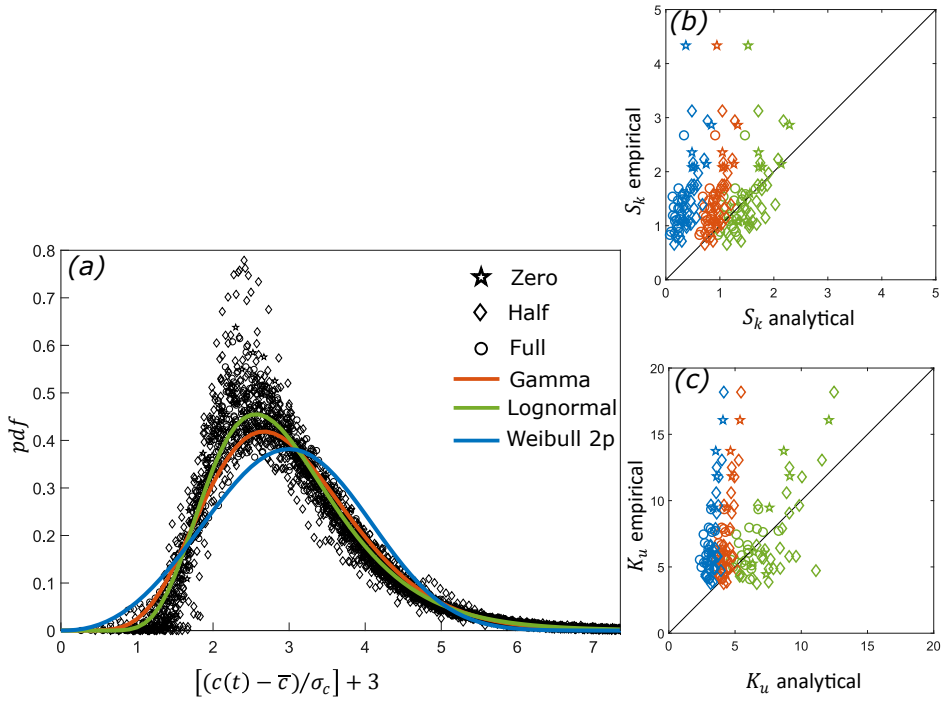


Figure 3.8 (a) Empirical pdfs fitted by the gamma (orange), lognormal (green), and Weibull 2p (blue) distributions. The Zero, Half, and Full configurations are considered. (b,c) Scatterplots that compare analytical and empirical skewness and kurtosis.

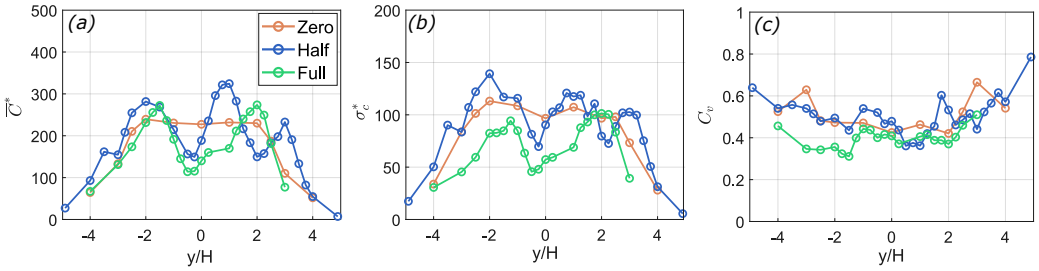


Figure 3.9 Longitudinal profile at x/H=1 and z/H=0.4 of (a) mean concentration, (b) concentration standard deviation, (c) coefficient of variation of the concentration, calculated from the long concentration time series. The Zero (orange), Half (blue), and Full (green) configurations are shown.

in the odor assessment (Oettl and Ferrero, 2017). Conversely, releases by linear sources were poorly investigated. Li and Bilger (1996) calculated the statistical moments of the scalar concentration behind a line source and they found that the empirical pdf is skewed to the right near the source and it is symmetrical and close to a Gaussian in the far field. Sawford and Stapountzis (1986) compared the pdf calculated from wind-tunnel measurements of concentration of heat, downstream of a line heating source (performed by Stapountzis et al., 1986), with a one-dimensional fluctuating model.

To fill this gap, we performed a statistical analysis of the pdf of long concentration time series, measured along longitudinal profiles in the centre of the canyon (see Section 3.1). To compare the pdfs calculated in different spatial points and different configurations, we adopt the sample space variable $\chi(t) = c(t)/\overline{c}$. By means of the method of moments (Kottegoda and Rosso, 1997), we fitted the empirical pdfs with the three analytical distributions mentioned above, that proved suitable to model the passive scalar concentration pdf in turbulent flows (as mentioned above): the gamma distribution, the lognormal distribution and the two-parameters Weibull distribution (Weibull 2p). The analytical pdfs can be commonly expressed as a function of the unique parameter, C_v:

1. gamma distribution:

$$F(\chi, \vartheta) = \frac{\vartheta^{\vartheta}}{\Gamma(\vartheta)} \chi^{\vartheta-1} \exp(-\vartheta\chi) \tag{3.1}$$

   where $\Gamma(\cdot)$ is the gamma function and ϑ is the the shape parameter, defined as $\vartheta = C_v^{-2}$.

2. lognormal distribution:

$$F(\chi, C_v) = \frac{1}{\chi\sqrt{2\pi \ln(1+C_v^2)}} \exp\Big\{ - \frac{\Big[\ln(\chi) + \ln\Big(\frac{1}{\sqrt{1+C_v^2}}\Big)\Big]^2}{2\ln(1+C_v^2)} \Big\} \tag{3.2}$$

3. Weibull 2p distribution:

$$F(\chi, C_v) = \frac{C_v^{-1.086}}{a_w} \Big(\frac{\chi}{a_w}\Big)^{C_v^{-1.086}-1} \exp\Big[- \Big(\frac{\chi}{a_w}\Big)^{C_v^{-1.086}} \Big] \tag{3.3}$$

where a_w is the scale parameter, which can be approximated as a function of C_v (Orsi et al., 2021):

$$a_w = \frac{1}{\Gamma(1 + C_v^{1.086})} \tag{3.4}$$

The goodness-of-fit between the empirical and analytical distributions was evaluated calculating the mean absolute error between the empirical cumulative distribution function (cdf) and the gamma, lognormal, and Weibull 2p cdfs. Comparing the mean absolute errors, we found that, in all spatial points and in all the tree density configurations, the largest absolute error is associated to the Weibull 2p distribution. This result was expected in the presence of a linear source, as the Weibull 2p distribution approximates the concentration pdf close to a point source where the meandering dominates the dispersion process (Orsi et al., 2021). Conversely, the lowest mean absolute error is associated to the lognormal distribution in 80% of the spatial points in the Zero configuration, in 70% in the Half configuration, and in 100% in the Full configuration. In the Zero and Half configurations, also the gamma distribution is a suitable model, indeed it shows a mean absolute error comparable to the one associated to the lognormal distribution in 60% of the spatial points in the Zero configuration and in 40% in the Half configuration.

The empirical pdfs together with the lognormal, gamma, and Weibull 2p distributions are reported in Fig. 3.8a. Here, the concentration time series were normalized as $[(c(t) - \overline{c})/\sigma_c] + 3$, to collapse all the distributions calculated along the longitudinal profiles into a single distribution with zero mean and unit variance. As the analytical distributions do not fit negative concentration fluctuations, the normalized concentration was shifted by a constant equal to 3. The empirical pdfs show a positive skewed bell-shaped behavior in all spatial points. The same shape is observed in the Zero, Half and Full configurations, hence it is not affected significantly by vegetation density. A qualitative observation of the overlap between analytical models and empirical pdfs confirms that the Weibull 2p distribution is the worst model, while both the gamma and lognormal distributions reproduce well the empirical pdfs, even though some discrepancies in the peak and in the left tail. The similarity among the pdfs is due to the fact that the longitudinal profiles of C_v (which is the only parameter that appears in equations 3.1-3.3) show variations of the

order of 6% (Fig. 3.9c), so they can be considered homogeneous along y-axis, as the variations are small compared to the local variations (up to 50%) found in the mean and turbulent concentration profiles (Fig. 3.9a,b).

We investigated the quality of the fitting also considering the third and fourth moments. The equations of the analytical skewness (S_k) and kurtosis (K_u) as a function of C_v are provided in Appendix A. In panels b and c of Fig. 3.8, we report the scatter plots of the analytical versus empirical skewness and kurtosis, respectively. The skewness is higher than zero, revealing that the pdfs are skewed to the right. The kurtosis is higher than 3, so the distributions have fatter tails than the Gaussian distribution. The empirical skewness and kurtosis are underestimated by the analytical functions provided by both the Weibull 2p and the gamma distributions. On the other hand, a non-biased estimation of the empirical moments is obtained from the lognormal distribution. Indeed, the scatter plot shows a good correlation between the empirical skewness and kurtosis with the analytical ones, mostly in the Full configuration. We can, therefore, conclude that the lognormal distribution performs a better fitting of the empirical skewness and kurtosis, and of the entire pdf, especially with high tree density.

3.2.3 Vertical mass transport

We decompose the vertical mass flux ($\overline{wc}$) into the mean component ($\bar{w}\bar{c}$) and the turbulent component ($\overline{w'c'}$) (Fischer et al., 1979). The latter corresponds to the cross-correlation between velocity and concentration fluctuations measured in the same control volume (see Sect. 3.1.1).

Figure 3.10 shows the non-dimensional mean, turbulent and total mass fluxes (where vertical velocity and concentration are normalised as defined in the previous sections), evaluated in the inner canyon. The behavior of the mean vertical fluxes (Fig. 3.10a1-a3) is similar to that of the mean vertical velocity (observed in Fig. 3.2a1-a3), characterized by a well-organized spatial pattern in the non-vegetated canyon, that is partially lost increasing the tree density. In the Zero configuration (panel a1 of Fig. 3.10), the mean mass flux is positive in two symmetric regions in the centre of the canyon and negative close to the edges. The Half configuration (panels a2) is characterized by three zones of

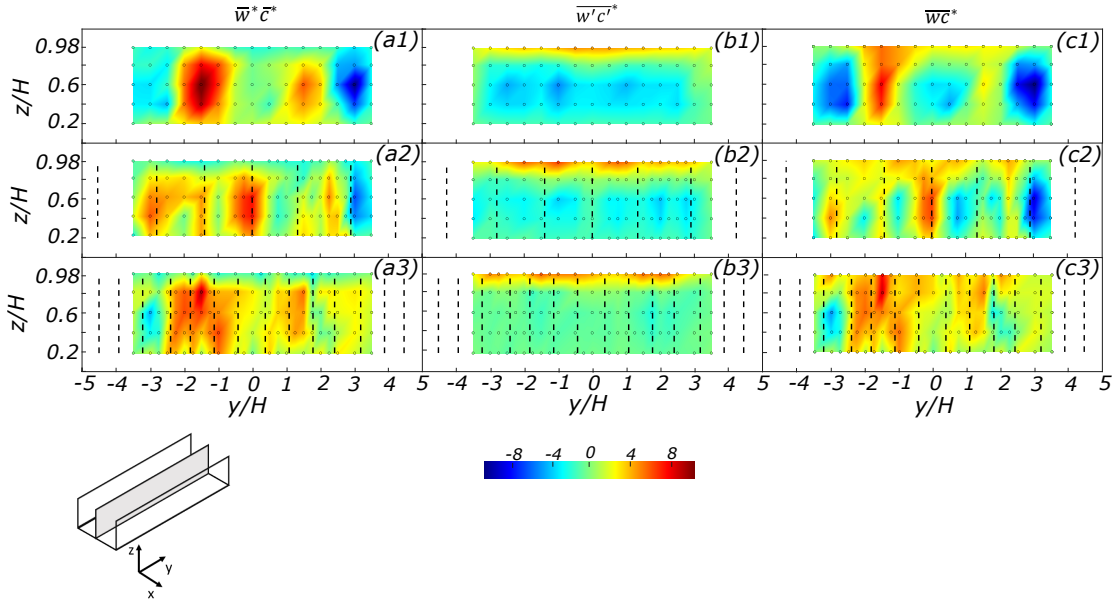


Figure 3.10 Two-dimensional sections of convective (a1-a3), turbulent (b1-b3), and total (c1-c3) mass fluxes on the plane at x/H=1. The Zero (a1, b1, c1), Half (a2, b2, c2), and Full (a3, b3, c3) configurations are shown. Black dashed lines indicate the position of the trees. Colored circles mark the measuring points. The shaded area in the sketch shows the position of the cross-section in the canyon.

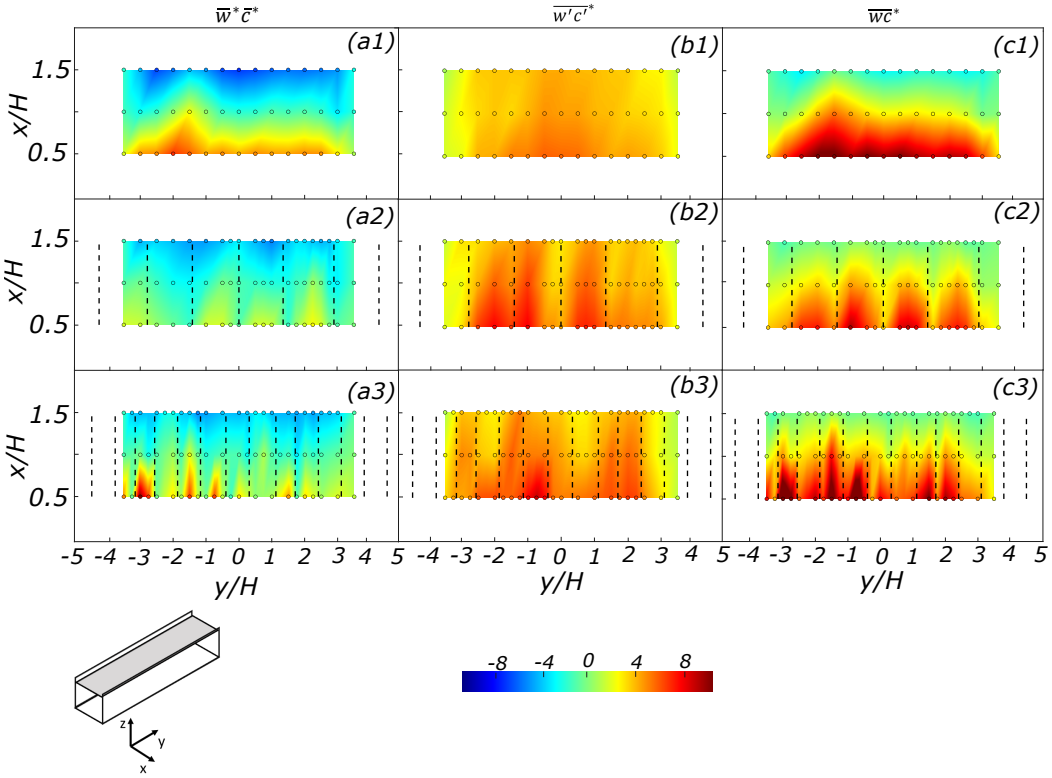


Figure 3.11 Two-dimensional sections of convective (a1-a3), turbulent (b1-b3), and total (c1-c3) mass fluxes on the plane at z/H=0.98. The Zero (a1, b1, c1), Half (a2, b2, c2), and Full (a3, b3, c3) configurations are shown. Black dashed lines indicate the position of the trees. Colored circles mark the measuring points. The shaded area in the sketch shows the position of the cross-section in the canyon.

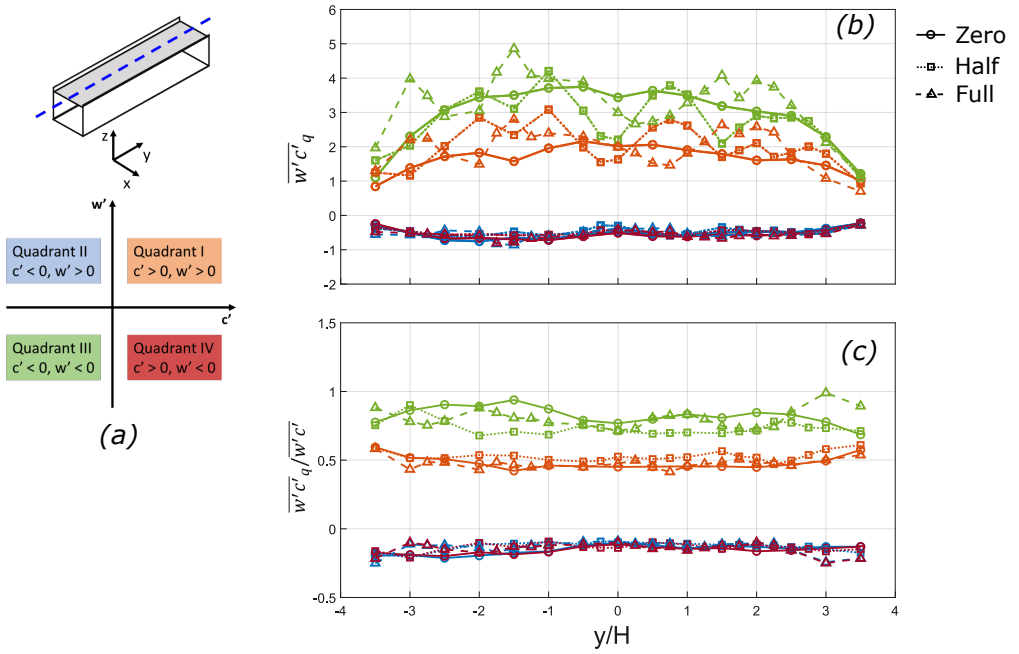


Figure 3.12 Quadrant analysis of $\overline{w'c'}$ at the rooftop of the canyon ($x/H = 1$, $z/H = 0.98$). (a) Schematic representation of the quadrants in the plane $\{c', w'\}$. (b) Local quadrant contributions to $\overline{w'c'}$. (c) Normalized quadrant contributions to $\overline{w'c'}$. The blue dotted line on the shaded plane in the top left inset represents the position where the quadrant analysis was performed.

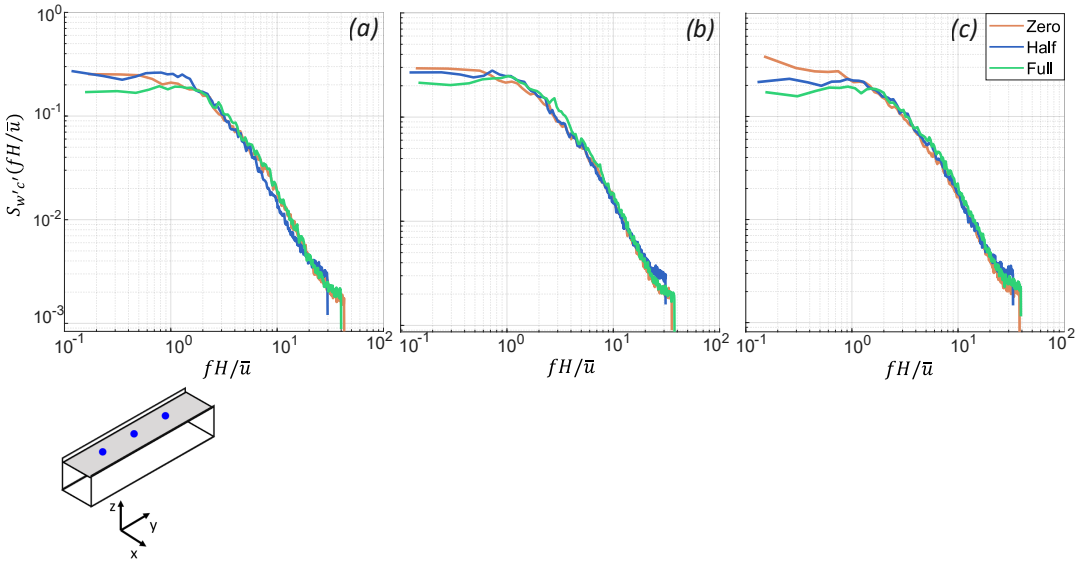


Figure 3.13 Spectra of $w'c'(t)$ calculated in three different sampling points along the central line (x/H=1) at the rooftop (z/H=0.98): (a) y/H=-1.5, (b) y/H=0, (c) y/H=2. The blue points on the shaded plane in the bottom inset represent the positions where the spectra were calculated.

positive mean flux, and three less extended zones of slightly negative flux. In the Full configuration (panels a3), the mean flux is positive almost in the whole section, except for an area close to the left edge where it is negative. Turbulent mass fluxes transport mass down homogeneously in the Zero configuration (panel b1) and in between the trees in the Half configuration (panel b2), while they uniformly approach zero in the Full configuration (panel b3). This reveals that $\overline{w'c'}^*$ is inhibited by an increasing tree density. Regardless of the presence of trees, $\overline{w'c'}^*$ at the interface between the canyon and the external flow (notably z/H=0.98) sharply increases to the same value (around 8), in line with σ_w^* and k^* (Fig. 3.2, panels b1-b3 and c1-c3, respectively). The total mass fluxes (3.2c1-c3) have the same spatial distribution of the advective fluxes, with lower tree density leading to higher heterogeneity along the y-axis. In the Zero and Half configurations, the contribution of the negative turbulent fluxes enhances the downward fluxes (blue areas in panels c1 and c2).

The mean mass flux and the mean vertical velocity (Fig. 3.11a1-a3 and Fig. 3.3a1-a3, respectively) follow the same behavior at the rooftop as well. In the non-vegetated canyon (panel a1 of Fig. 3.11), the mean flux is homogeneous and negative along the downwind wall (x/H=1.5), where the external flow (without pollutant) enters the canyon, and homogeneous and positive along the upwind wall (x/H=0.5), where the polluted air leaves the canyon. We detect the same streamwise pattern in the vegetated canyons (panels a2, a3), but the outgoing mean flux is broken into smaller flux segments by the presence of trees. Moreover, positive $\bar{w}^*\bar{c}^*$ fluxes are weaker in the Half configuration (panel a2), while their intensity is not homogeneous along y in the Full configuration (panel a3). Turbulent mass fluxes (panels b1-b3) are positive and quite homogeneous in all configurations with significantly larger values than inside the canyon (Marucci and Carpentieri, 2019), especially in the presence of trees (panels b2, b3). As already observed inside the canyon, the total vertical mass fluxes (panels c1-c3) follow the same trend of $\bar{w}^*\bar{c}^*$, but the strong positive contribution of the turbulent fluxes enhances the upward transport, and leads to slightly positive fluxes at the downwind wall. Therefore, the upward total mass fluxes at the upwind wall are significantly higher than the mean ones, and they are more heterogeneous with the increase in tree density.

In order to understand if the positive turbulent mass fluxes detected at the rooftop (Fig. 3.11b1-b3) are due to the entrance of clean external flow or to

the leaving of polluted air from the canyon, we perform the quadrant analysis (e.g. Di Bernardino et al., 2018). The time series of $w'c'(t)$ are decomposed on the four quadrants of the Cartesian plane $\{c',w'\}$. In Fig. 3.12a, we report a scheme of the quadrant division: quadrant I identifies outflow events with a concentration higher than the mean, while quadrant III inflow events with a concentration lower than the mean.

In Fig. 3.12b, we report for a longitudinal profile at the centre of the canyon rooftop ($x/H = 1$ and $z/H = 0.98$) the local contribution of each quadrant, defined as the sum of the turbulent fluxes in the quadrant ($\overline{w'c'_q}$, where q=I, II, III, IV). Regardless of the presence of trees, the contributions of quadrants II and IV, which represent negative turbulent mass fluxes, are negligible relative to the ones of quadrants I and III, as expected (see Fig. 3.11b1-b3). The contribution of quadrant III is higher than the one of quadrant I, meaning that the entrance of external clean air provides a higher contribution to the positive turbulent mass fluxes in the centre of the canyon rooftop than the exiting of polluted air. Comparing the different tree density configurations, we notice a clear distinction between the spatial homogeneity of the profiles of quadrant I and III in the Zero configuration (continuous lines), and their heterogeneity in the vegetated canyons (dashed lines). Thus, the presence of trees affects the local contribution of inflow and outflow events. Conversely, the normalized quadrant contributions to $\overline{w'c'}$ – expressed as the ratio between $\overline{w'c'_q}$ and the total contribution of all quadrants ($\overline{w'c'}$) – is uniform along the canyon axis, regardless of the presence of trees (Fig. 3.12c).

We performed the spectral analysis of $w'c'(t)$ signal, to investigate the turbulent scales involved in the turbulent mass transport at the rooftop of the canyon. Figure 3.13 shows the spectra of the normalized mass fluxes $(w'c'(t) - \overline{w'c'})/\sigma_{w'c'}$ (where $\sigma_{w'c'}$ is the standard deviation of $w'c'(t)$ signal), calculated at $y/H = [-1.5, 0, 2]$, along the central profile at the canyon rooftop. As we observed in the vertical velocity spectra (Fig. 3.4), the large-scale structures dominate the turbulent mass transport in the empty canyon, and the energy associated to them decreases with the increase in tree density.

3.3 Conclusions to Chapter 3

The aim of this chapter was to investigate the impact of tree-lined avenues on turbulent flow and concentration fields, and on the vertical mass transport in an urban street canyon, subject to an external boundary layer. This was addressed by performing concentration, velocity, and combined concentration-velocity measurements inside a large canyon (H/W_w=0.5) oriented perpendicular to the wind direction, in a wind tunnel. Three different tree densities were considered: an empty canyon (Zero configuration), a canyon with low tree density (Half configuration), and a canyon with high tree density (Full configuration).

The increase of vegetation density leads to a partial homogenization of the mean vertical velocity field and to a reduction of the turbulent kinetic energy, inside the canyon. However, at the rooftop, the presence of trees does not significantly smooth the intensity of velocity fluctuations, but, it partially hinders the mean vertical velocity at the upwind wall. The tree-induced reduction of turbulent fluctuations unveils a peculiar effect of high-density vegetation on turbulent dynamics inside a canyon. This effect deserves the attention of the scientific community as tree avenues with intersecting crowns are common in many European cities.

Concerning concentration fluctuations, we found that vegetation induces a transition from an almost homogeneous pattern (characteristic of the non-vegetated canyon), to a heterogeneous one, both inside the canyon and at the rooftop. On average, the intensity of concentration fluctuations is not significantly smoothed by the presence of trees, rather local maxima are exacerbated in the vegetated canyons than in the empty one. The coefficient of variation of the concentration does not show a significant spatial pattern with the tree density, even if we notice that it slightly decreases in the Full configuration. Within the canyon, the C_v assumes values that vary between 0.4 and 0.6.

The statistical analysis of the concentration time series reveals that the concentration pdf is skewed towards positive values, it has fatter tails with respect to the Gaussian distribution, and it maintains the same shape in the different tree density configurations. The gamma and the lognormal distributions perform a good fitting of the experimental pdf in the Zero and Half configurations, while in the Full configuration, the lognormal distribution

is the best model. In all configurations, the lognormal distribution provides the best estimate of the third and fourth moments.

The total mass fluxes are mainly governed by the mean mass fluxes, which in turn show almost the same pattern of the mean vertical velocity. The pattern of mean mass fluxes depends on vegetation: inside the canyon, the mean mass fluxes show a well-organized spatial pattern in the empty canyon, which is lost increasing the tree density and, at the rooftop, the upward mean mass fluxes are hindered by trees. Turbulent mass fluxes are homogeneous and negative inside the non-vegetated canyon, while they are reduced to almost zero with high vegetation density. The vegetation-induced decrease in the turbulent mass fluxes (as well as vertical velocity standard deviation and turbulent kinetic energy) may be responsible for a reduction of the mixing inside the canyon, leading to a more heterogeneous scalar field in the vegetated canyon. At the rooftop, turbulent fluxes are high and positive and their intensity is not affected by the presence of trees. The quadrant analysis reveals that, regardless of the presence of trees, the inflow events of clean air (quadrant III) provides an higher contribution to the positive turbulent mass fluxes at the rooftop than outflow events of polluted air (quadrant I). Moreover, we showed that the normalized contribution of inflow and outflow events to $\overline{w'c'}$ is homogeneous along the longitudinal direction of the canyon. On the contrary, in the presence of trees, the local contribution of outflow (quadrant I) and inflow events is heterogeneous along the longitudinal axis of the rooftop.

The spectral analysis of the vertical velocity and turbulent mass fluxes signals revealed that the energy content of large-scale structures decreases with the increase in tree density, or rather the decrease in tree spacing.

The wind-tunnel experimental campaign allowed us to highlight the complexity of the turbulent mass transport within an urban street canyon, with different vegetation densities. While high vegetation density has been shown to enhance thermal comfort and urban biodiversity, its impact on air quality remains a subject of debate. On one hand tree avenues increase pollutant deposition and regulate local temperature; on the other hand the tree crowns, especially the intersecting ones, hinder the vertical mean flow and dampen turbulent kinetic energy and turbulent mass fluxes. As a consequence of that, at the pedestrian level, the transport and the mixing is less efficient, mostly

close to the upwind wall, an issue which has to be considered together with the beneficial effects of high tree density.

A limit of the present study was that the experimental equipment employed to measure velocity and mass fluxes (LDA, mirror, LDA-FID system) was not suitable to perform measurements close to the canyon walls, due to the reflection of the laser beams on the miniatures of trees. This issue prevented us to capture the three-dimensionality of the turbulent flow and scalar transport within the canyon, thus to completely identify the flow dynamics leading to the formation of concentration peaks in a vegetated canyon. However, we provided high-resolution measurements of the mean and turbulent concentration, vertical flow velocity, and mass fluxes in the centre and at the rooftop of a canyon, perpendicular to the external flow. In the next chapters of this thesis, we analyse the turbulent flow fields within canyons, considering non-orthogonal wind directions.

Chapter 4

Turbulent flow within a wind-aligned street canyon

The work described in this chapter has been partially derived from Del Ponte et al. (2025).

While numerous studies have been conducted on perpendicular street canyons (Gromke and Ruck, 2007; Zhao et al., 2023b; Carlo et al., 2024), the case of canyons aligned with the wind direction has received limited attention, especially in experimental research, even though its relevance for modeling pollutant dispersion in urban environments. Assessing advective transport along the street axis is crucial, as it governs the longitudinal dispersion of pollutants (and, more generally, passive scalars) within urban canyons and influences pollutant spreading across street networks (Soulhac et al., 2013; Salem et al., 2015; Fellini et al., 2021). Previous studies (Soulhac and Salizzoni, 2010; Huang et al., 2019) have shown that, in the absence of vegetation, for sufficiently long streets, a wind direction parallel to the street axis can lead to pedestrian-level pollutant concentrations that may exceed those observed in perpendicular canyons. The presence of trees further complicates dispersion dynamics by altering both mean flow structures and turbulence characteristics, thereby affecting pollutant transport mechanisms.

To our knowledge, only Gromke and Ruck (2012) conducted wind tunnel experiments within vegetated urban canyons under non-orthogonal wind directions. Their study analysed the mean concentration field in an isolated

canyon with trees oriented at 0°, 45°, and 90° relative to the wind direction. The results revealed that, in canyons with trees and a low height-to-width ratio, a wind parallel to the canyon axis produced the lowest concentration levels among all tested wind orientations. The scarcity of experimental studies on vegetated street canyons aligned with the wind direction, in contrast to the abundance of studies on perpendicular configurations, highlights the need to deepen our understanding of the aerodynamics of the former through wind tunnel experiments. Such an experimental approach allows for a quantitative characterization of the phenomenon and provides valuable data to validate the numerous numerical simulations that have been conducted on this configuration (Buccolieri et al., 2011; Jeanjean et al., 2015, 2017; Maison et al., 2022). Furthermore, these experimental measurements not only support model validation but also enhance our understanding of urban canyon ventilation mechanisms, which can be parameterized in analytical models (Soulhac et al., 2008) of the flow, needed to simulate pollutant dispersion at the district scale (Soulhac et al., 2013).

To address this knowledge gap, in this chapter, we examine how the presence of vegetation influences the mean and turbulent flow fields within a canyon aligned with the external wind direction. After some preliminary assessments of the longitudinal homogeneity of the flow within the canyon (Sect. 4.2), we describe the mean and turbulent velocity fields in the canyon (Sect. 4.3) considering two different canyon geometries, notably, a square canyon (Sect. 4.3.1) and a large canyon (Sect. 4.3.2). Finally, in Sect. 4.4.1, we compare the experimental data with the analytical model developed by Soulhac et al. (2008), characterizing the mean flow along the longitudinal axis of a wind-aligned street canyon. In Sect. 4.4.2, we provide an estimate of the pressure loss coefficient associated with trees in the vegetated canyons, for varying canyon geometries. Conclusions to this work are drawn in Sect. 4.5.

4.1 Experimental details

Within the street network in Configuration 2 (Fig. 2.1d), we selected a longitudinal street canyon with a length of L=3.5 m and a height of H=0.1 m as the reference canyon (see the yellow area in figure 4.1a). The lateral edges of the

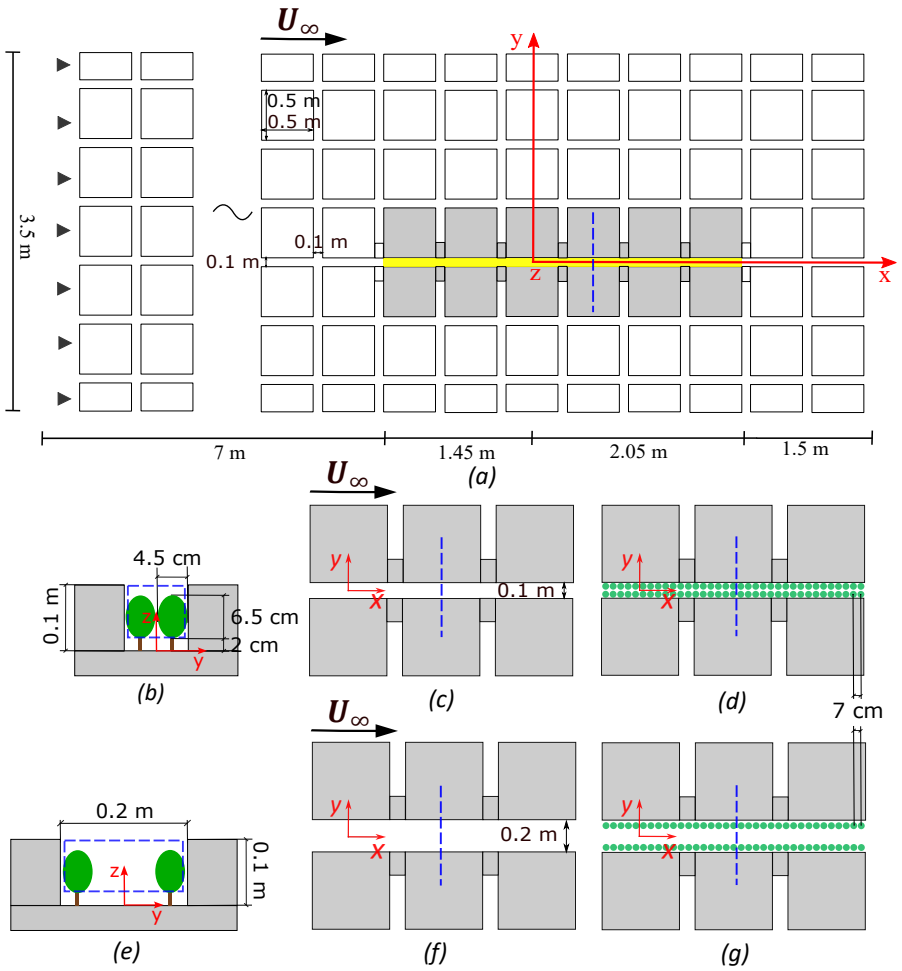


Figure 4.1 (a) Scheme of the urban canopy modeled in the wind tunnel. The black triangles indicate the Irwin spires at the entrance of the test section, the red arrows represent the reference system, the yellow line marks the reference canyon, and the blue dashed line indicates the longitudinal position of the measuring section. The blocks confining the reference canyon are coloured grey. (b) Front view of the square canyon with trees and planar view of the square canyon without (c) and with (d) trees. (e) Front view of the large canyon with trees and planar view of the large canyon without (f) and with (g) trees. The blue rectangles in panels (b) and (e) indicate the position of the measuring section in the transversal section of the canyon.



Figure 4.2 (a) Tree-lined boulevard in Paris. Source: *Avenue lined with trees in Paris* by K.G.Hawes/Flickr. (b) Tree-lined boulevard in Turin. (c) Tree-lined street canyon modeled in the wind tunnel.

reference canyon were confined to simulate an infinitely long two-dimensional canyon (i.e., with a length-to-height ratio of $L/H = 35$) and to prevent disturbances in the longitudinal flow due to transversal fluxes. Two different canyon widths were considered: W=0.1 m and W_w=0.2 m, creating a square canyon and a wider canyon, with height-to-width ratios of H/W=1 and H/W_w=0.5, respectively. Note that only the reference canyon width was modified, while the rest of the network was kept with an aspect ratio H/W equal to 1. The reference canyon begins approximately 7 m from the entrance of the test section (14 times the height of the vortex generators) to ensure the flow is fully developed (Salizzoni et al., 2008). The longitudinal homogeneity of the flow along the square and the large canyons and the absence of flow perturbation due to the change in the aspect ratio are discussed in Sect. 4.2. We defined the origin of the coordinate system on the longitudinal axis of the canyon, $15H$ far from the entrance of the reference canyon, with the vertical axis starting at ground level. The x-, y-, and z-axes are oriented in the streamwise, transversal, and vertical directions, respectively (see the red arrows in figure 4.1a).

To achieve a homogeneous vegetation cover, we arranged the model trees along the entire length of the lateral walls of the reference canyon in three different configurations: no trees in the canyon (Zero configuration, figure 4.1c,f), two parallel rows of trees spaced 14 cm apart (Half configuration), and two parallel rows of trees spaced 7 cm apart (Full configuration, figure 4.1d,g), with spacing measured along the x-axis. We used the canyon with H/W=1 to simulate dense vegetation cover with intersecting crowns, typical of European

cities (Fig. 4.2), and the canyon with H/W_w=0.5, to simulate large boulevards with sparser vegetation, easier to see in the majority of cities worldwide.

4.2 Longitudinal homogeneity along the street canyon

As a first step, we verified that the velocity statistics within the canyon are invariant along the longitudinal direction, by measuring in the square canyon the velocity statistics along three longitudinal profiles y/H={-0.25,0,0.25}, at z/H=0.4. We measured also three vertical profiles of $\overline{u}$ in the centre of the canyon (at $y/H = 0$), at different x-positions (at x/H={0,4.4,11}). We repeated the analysis in the Zero, Half, and Full configurations. In Fig. 4.3, we report the longitudinal profiles of the mean longitudinal velocity and the standard deviation of the longitudinal and transversal (σ_v) velocity, at y/H=0.25, i. e. close to the left line of trees in the vegetated configurations (the profiles at y/H={-0.25,0} are available in Appendix B). Both the mean and the standard deviation are normalized by the free-stream velocity (U_∞). In the empty canyon, $\overline{u}/U_\infty$, σ_u/U_∞, and σ_v/U_∞ are homogeneous along the street axis (see blue profiles, in panels 4.3a-c). By adding trees (see orange and green profiles), the profiles become noisy, mostly with low tree density (orange profiles), even if the spatial pattern of the fluctuations can hardly be associated to the tree position. The t-test (Montgomery et al., 2021) shows that, regardless of the tree density, the $\overline{u}/U_\infty$, σ_u/U_∞, and σ_v/U_∞ profiles do not exhibit (with significance level equal to 0.01) a well-defined trend along the x-axis of the canyon. The longitudinal homogeneity of the flow is also confirmed by the good overlap between the vertical profiles of $\overline{u}/U_\infty$ measured at different x-positions (panel 4.3d).

Note that doubling the vegetation density (i. e., moving from the Half to the Full configuration) produces small longitudinal variations of $\overline{u}/U_\infty$ (see the orange and green profiles in panels 4.3a and 4.3d) within the range [0, 0.1]. This variation is minimal compared to the substantial difference in mean velocity between a vegetated canyon (Half or Full configurations) and an empty canyon, where $\overline{u}/U_\infty$ is around 0.4. Therefore, while increasing tree density from Half to Full leads to minor changes in the intensity and spatial behavior

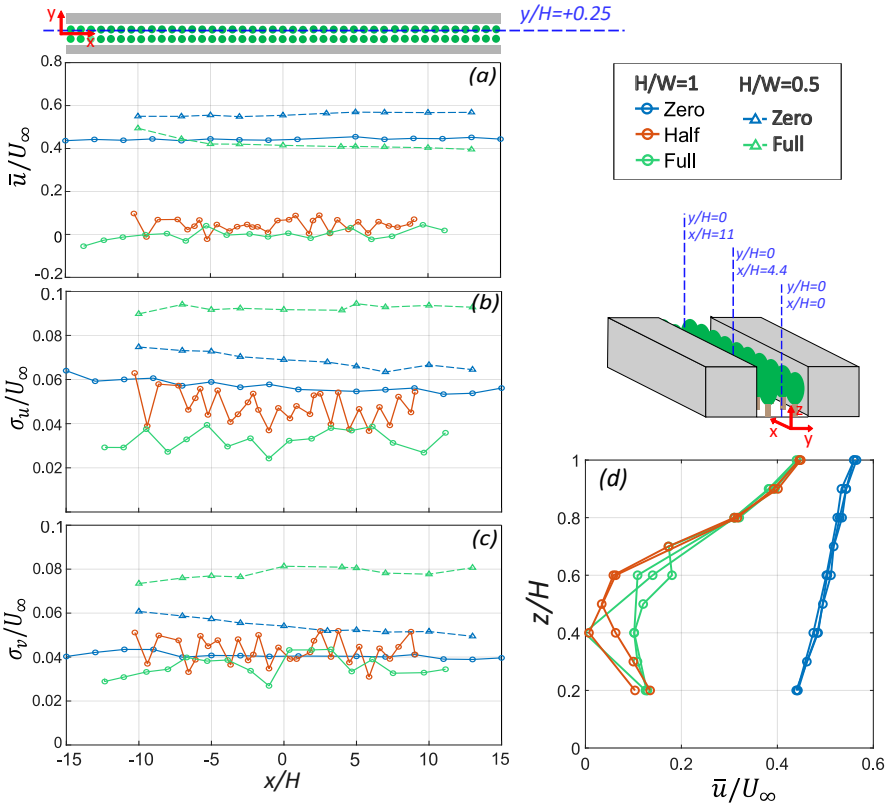


Figure 4.3 Longitudinal profiles, measured in the square (continuous line) and large (dashed line) canyons at y/H=+0.25 and z/H=0.4, of the mean longitudinal velocity (a) and standard deviations of the longitudinal velocity (b) and transversal velocity (c). The Zero (blue), Half (orange), and Full (green) configurations are shown. The green circles in the sketch at the top of the figure indicate the position of the trees inside the canyon, spaced 7 cm apart. The position of the trees in the Half configuration can be deduced alternately removing half circles symmetrically with respect to the centre. The blue dashed line reported in the sketch indicates the transversal position with respect to the tree lines of the longitudinal profiles. (d) Vertical profiles of the mean longitudinal velocity, measured in the square canyon, at different longitudinal positions around x/H={0,4.4,11} (at $y/H = 0$), in the Zero, Half, and Full configurations. The blue dashed line in the sketch provides an indicative representation of the positions of the vertical profiles.

of the mean flow, the difference is small compared to the contrast observed between the empty and vegetated canyons. Turbulent intensities show more pronounced differences between the Half and Full configurations. In the Half configuration, σ_u/U_∞ values consistently fall between those of the Zero and Full profiles, while σ_v/U_∞ exhibits fluctuations similar to the Zero configuration. For these reasons, and for the sake of brevity, we will focus on the mean and turbulent flow fields in the Zero and Full configurations only. Four different configurations will be analysed: a square canyon (i) without vegetation (Fig. 4.1c) and (ii) with two parallel rows of trees with touching crowns (Fig. 4.1d), and a large canyon (iii) without trees (Fig. 4.1f) and (iv) with two rows of trees spaced 0.14 m apart (Fig. 4.1g).

We verified the longitudinal homogeneity of the velocity statistics also in the large canyon, measuring longitudinal profiles of $\overline{u}/U_\infty$, σ_u/U_∞, and σ_v/U_∞ in the centre of the canyon ($y/H = 0$), in the Zero and Full configurations, only. In Fig. 4.3a-c (see the dashed lines) we can see that the profiles of both the mean longitudinal velocity and the turbulent velocity fluctuations show a small trend close to the entrance of the reference canyon (x/H in the range [-10,0]) due to the transition from aspect ratio $H/W = 1$ to $H/W = 0.5$. However, sufficiently far from the entrance of the canyon (i. e., $x/H > 0$), the longitudinal profiles of $\overline{u}/U_\infty$, σ_u/U_∞, and σ_v/U_∞ do not show any statistically significant trend, as demonstrated by the t-student test with significance level 0.01.

Since the flow is statistically uniform along the x-axis, in the following we present the results of the velocity measurements on a single cross-section, located $20H$ from the canyon entrance (see blue dotted line in Fig. 4.1a). The horizontal resolution of the measuring grid was 2 cm, while the vertical resolution was 2 cm in the range $0.2 \leq z/H \leq 0.8$ and 1 cm in the range $0.8 \leq z/H \leq 1$, in order to capture the flow dynamics at the interface between the canyon flow and the external flow. To prevent laser beam reflections on the walls, measurements were conducted no closer than 1 cm from the vertical walls and 2 cm from the floor.

4.3 Results: turbulent flow field within the street canyon

To examine the influence of vegetation density and street geometry on street-canyon flow, we analyse the first four statistical moments of the velocity pdf: specifically, the mean, standard deviation, skewness, and kurtosis of the longitudinal and transverse velocity time series, within the square (Sect. 4.3.1) and large (Sect. 4.3.2) canyons. For each geometry, we consider the empty (Zero) and the vegetated (Full) canyon configurations. Flow statistics are shown on the transversal section, by linearly interpolating the data. The mean and the standard deviation of the longitudinal and transversal velocity are normalized by the free-stream velocity U_∞.

4.3.1 Square street canyon: H/W=1

In the empty canyon, the mean longitudinal velocity $\overline{u}$ (panel 4.4a) shows a faster central core that decreases monotonically to zero towards the floor and the lateral walls. The mean transversal velocity $\overline{v}$ (panel 4.4b) is zero in the whole section – being the spatial average of $\overline{v}/U_\infty$ in the cross-section equal to 0.004 –, highlighting a good alignment of the canyon with the external flow. The longitudinal velocity standard deviation σ_u (panel 4.4c) exhibits a crosswise increase, but the difference between the centre and the sides of the canyon is less marked than that observed for $\overline{u}$. In the vertical direction, σ_u/U_∞ decreases monotonically from around 0.08 at the rooftop, to 0.055 close to the ground. The vertical pattern of the transversal velocity standard deviation σ_v (panel 4.4d) is divided into two zones of almost homogeneous intensity: around 0.065 at the rooftop (z/H=[0.9,1]) and 0.04 within the canyon (z/H=[0.2,0.8)), showing a slight decreasing pattern towards the lateral walls. The gradient of σ_v/U_∞ at the rooftop denotes the presence of a shear layer, where local t.k.e. production leads to an increase of flow velocity fluctuations (Salizzoni et al., 2011; Fellini et al., 2020). The skewness of u and v (panels 4.4e and 4.4f, respectively) are almost zero on the whole cross-section, indicating symmetric fluctuations around the mean. The kurtosis of u (panel 4.4g) is quite homogeneous, showing values around to 3. A zero skewness and a kurtosis around 3 suggest a Gaussian-

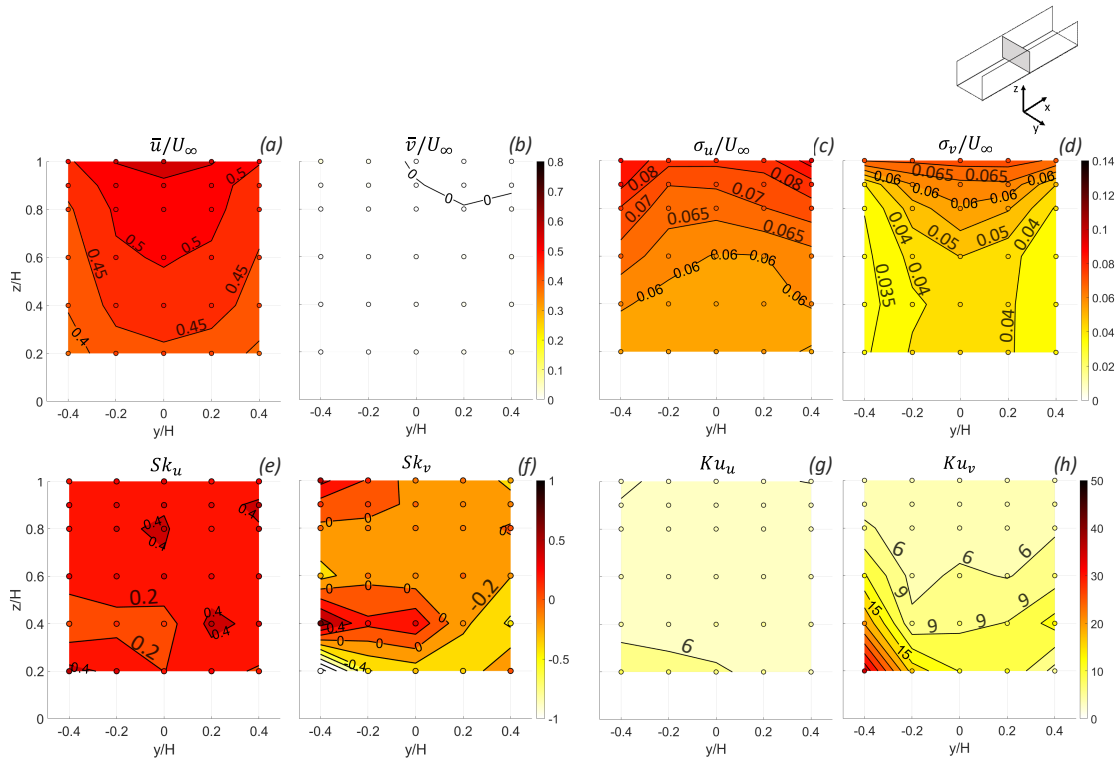


Figure 4.4 Transversal behaviour, in the square canyon and in the Zero configuration, of the mean longitudinal velocity (a), mean transversal velocity (b), longitudinal velocity standard deviation (c), transversal velocity standard deviation (d), longitudinal velocity skewness (e), transversal velocity skewness (f), longitudinal velocity kurtosis (g), and transversal velocity kurtosis (h).

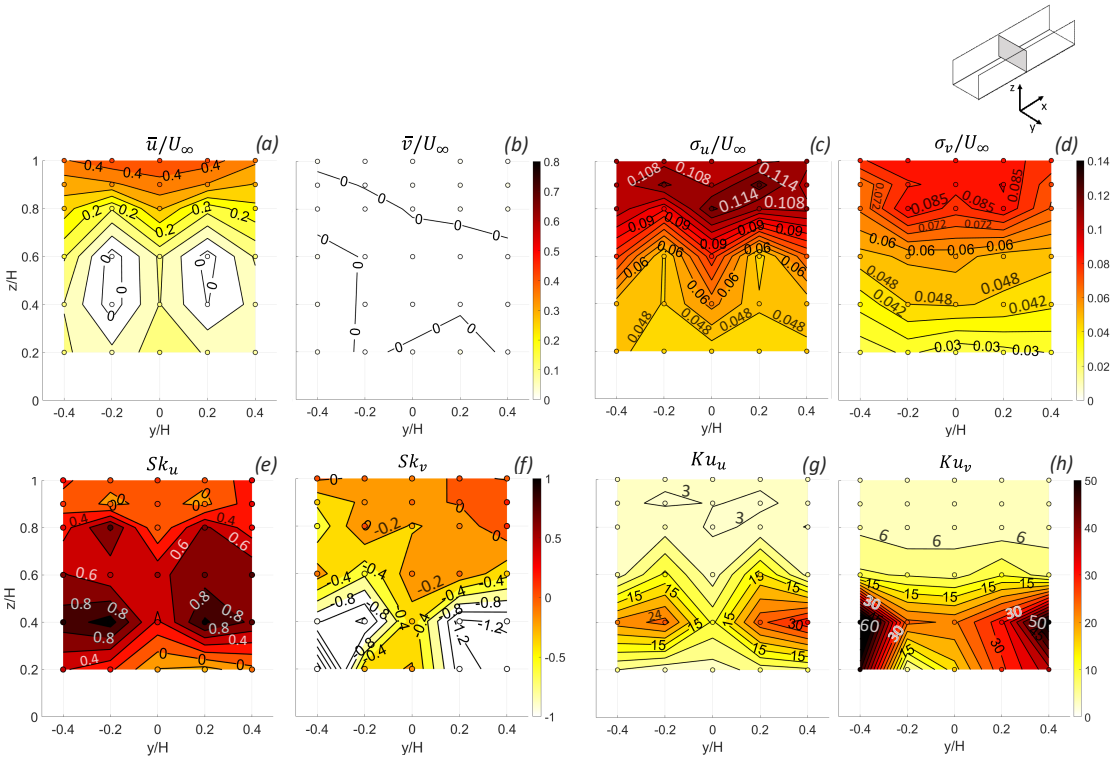


Figure 4.5 Transversal behaviour, in the square canyon and in the Full configuration, of the mean longitudinal velocity (a), mean transversal velocity (b), longitudinal velocity standard deviation (c), transversal velocity standard deviation (d), longitudinal velocity skewness (e), transversal velocity skewness (f), longitudinal velocity kurtosis (g), and transversal velocity kurtosis (h).

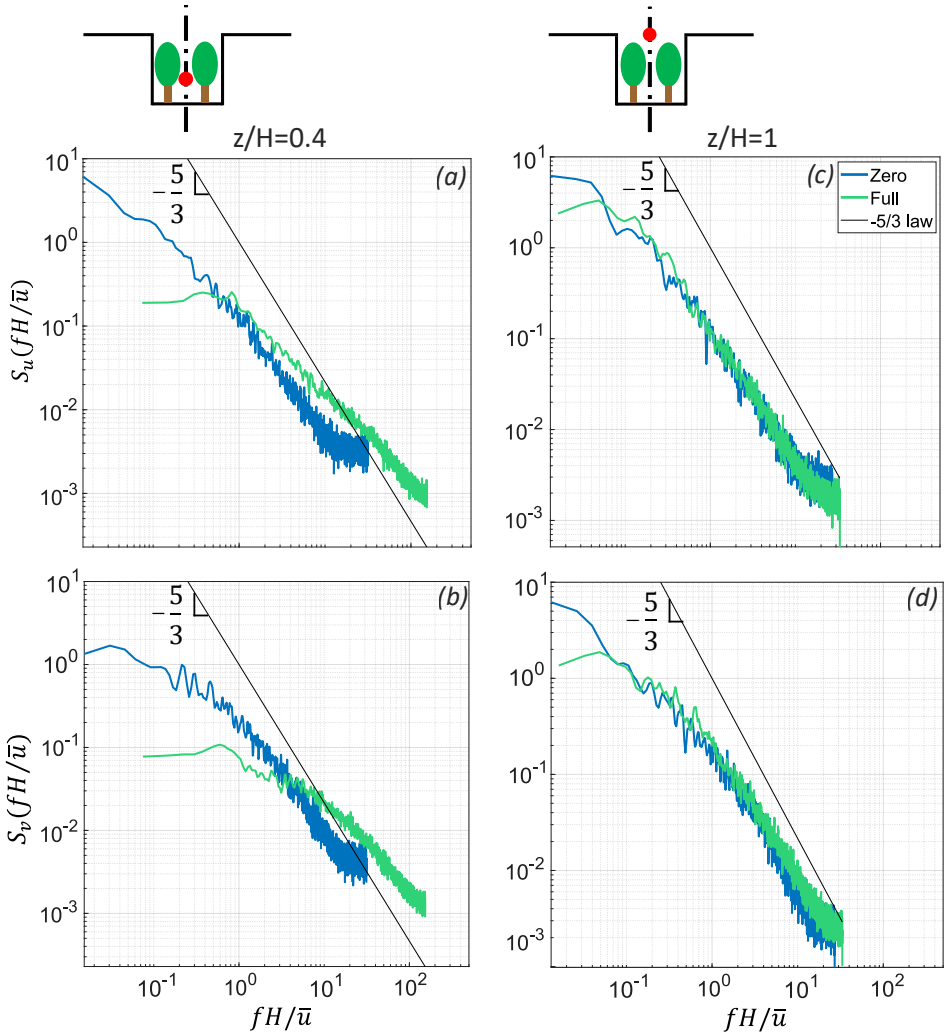


Figure 4.6 Spectra of $(u(t)-\overline{u})/\sigma_u$ and $(v(t)-\overline{v})/\sigma_v$, measured along the vertical axis of the canyon (y/H=0), at z/H=0.4 (a,b) and z/H=1 (c,d), in the square canyon. The black line refers to the -5/3 law. The positions where the spectra where calculated are represented with the red dot in the sketches above the panels.

like behaviour of the pdf of the longitudinal velocity fluctuations. We assessed the similarity with a Gaussian distribution, calculating the pdf of velocity time series acquired in the centre of the canyon and performing a Kolmogorov-Smirnov test with significance level 0.05. A deviation from the Gaussian arises in the lower left-hand corner of the cross-section, where Ku_u increases to 6. Conversely, the kurtosis of v (panel 4.4h) is not perfectly homogeneous across the measuring section, but it shows values around 9 along the transversal profiles at z/H=$\{0.2,0.4\}$, around 6 at $z/H = 0.6$, and a peak around 30 in the lower left corner, suggesting fatter tails of the pdf of the transversal velocity fluctuations with respect to a Gaussian distribution. The slight asymmetries observed may be attributed to the sensitivity of the fourth-order statistical moment to minor inaccuracies in the arrangement of the building-like obstacles within the wind tunnel (Garbero et al., 2010; Fuka et al., 2018), as well as to the potentially imperfect alignment of the external wind flow with the wind tunnel axis (Nironi et al., 2015; Carlo et al., 2024).

In the vegetated canyon, the flow channeling is significantly hindered. The spatial patterns of $\overline{u}/U_\infty$ (Fig. 4.5a) exhibit two symmetric zones of nearly-zero values around the silhouettes of the trees (i.e., z/H in the range [0.2,0.8] and y/H in the ranges [-0.4,0) and (0,+0.4] for the first and second tree, respectively) and a sharp increase in the mean velocity at the rooftop, where the external flow enters the canyon. Overall, the average mean longitudinal velocity in the cross-section $U_{tr,exp} = 0.76$ ms^{-1} ($U_{tr,exp}/U_\infty = 0.15$) – calculated averaging the $\overline{u}$ measurements resampled onto a 5 mm resolution grid using linear interpolation (subscripts 'tr' and 'exp' recall the presence of trees and the experimental evaluation, respectively) – is 70% lower than the one in the non-vegetated canyon ($U_{exp} = 2.39$ ms^{-1} and $U_{exp}/U_\infty = 0.48$). This substantial difference (found also by Maison et al., 2022) is primarily attributed to the obstruction caused by the trees. This is evident when quantifying the average mean longitudinal velocity in the region between the trees (evaluated considering $\overline{u}$ measurements in the range z/H=[0.2,0.6]) which is 80% lower than the value calculated in the empty canyon over the same area. At the rooftop level (z/H=[0.8,1]), however, this difference is reduced to 25%. The impact of the trees is also evident for σ_u (see Fig. 4.5c), which is amplified in the upper part of the tree crowns and above them, while being suppressed in the region surrounding the trees. Specifically, σ_u/U_∞ reaches intensities of

approximately 0.11 in the upper part of the canyon — 30% higher than in the empty canyon — and around 0.05 around the tree silhouette, which is 15% lower than in the empty canyon at the same height range. In contrast, the pattern of σ_v/U_∞ (Fig. 4.5d) is relatively uniform across the canyon width but decreases steadily with height, ranging from 0.08 above the tree crowns, representing a 20% increase compared to the empty canyon, to approximately 0.03 near the ground. The increased turbulence at the canyon rooftop is driven by the interaction between the tree crowns and the external flow. Closer to the ground, the presence of trees dampens turbulent fluctuations and impedes the mean flow, as evidenced by the low values of both mean and turbulent velocities along the transverse profile at z/H=0.2, in panels 4.5a-d). This interaction can trap pollutants emitted at pedestrian level and reduce street ventilation. In contrast with the empty canyon, the third and fourth order moments (Fig. 4.5e and 4.5f) exhibit slight heterogeneity across the cross-section. Around the tree silhouette, the skewness of u (Sk_u) shows slightly positive values around 0.8, while the skewness of v (Sk_v) shows slightly negative values, around -1. The correlation of this pattern with the vegetation silhouette suggests that skewness values different from zero could be induced by interaction between turbulent structures and vegetation elements. In the same region, the kurtosis of u (Ku_u) and v (Ku_v) reaches peaks up to 30 and 50, respectively (see panels 4.5g and 4.5h). Note that the spatial heterogeneity of Ku_u is more marked with respect to the one observed in the empty square canyon. However, the significant increase in kurtosis should be attributed to the reduction in velocity standard deviation between the trees, rather than to the presence of fatter tails in the velocity probability density function.

We can observe a quite similar spatial patterns of the mean and standard deviation of the longitudinal and transversal velocity within a canyon with half vegetation density (see the statistical moments measured in the Half configuration in Appendix C). Notably, we found a 80% decrease of $\overline{u}/U_\infty$ with respect to the empty canyon in between trees, as well as an amplification of σ_u/U_∞ and σ_v/U_∞ at the canyon rooftop, due to the interaction between the tree crowns and the external flow. We estimated a 15% difference in the average mean longitudinal velocity in the cross-section between the Half and Full configurations (being $U_{tr,exp}$=0.90 ms^{-1}, in the Half configuration), which is negligible with respect to the difference between the Zero and Full

configurations. The decrease in tree density leads to intensities of the skewness and kurtosis of u and v slightly higher in modulus with respect to the Full configuration. Notably, close to the ground Sk_u and Sk_v reaches maximum values around 5 and -6, respectively, and Ku_u and Ku_v around 60 and 80. Conversely, at the canyon rooftop (i.e., z/H=[0.8,1]), they recover values equal to zero and 3, respectively, as observed in the Full configuration. The difference in the intensity and spatial patterns of skewness and kurtosis, with respect to the Full configuration, arises probably due to the higher sensibility of these statistical moments to the displacement of the trees.

To investigate the turbulent scales involved in energy transport within both vegetated and non-vegetated canyons, we calculated the power spectral density of the longitudinal and transverse velocity time series. The Welch method was applied by resampling the velocity signals at a regular frequency of 1500 Hz and dividing them into 2500-point windows. In Fig. 4.6, we report the spectra of $u(t)$ and $v(t)$ calculated in two different positions along the vertical axis of the canyon (y/H=0): in between the tree crowns (at z/H=0.4, Fig. 4.6a,b) and above them (at z/H=1, Fig. 4.6c,d). In order to compare spectra among different positions and vegetation configurations, we forced all spectra to have the subtended area equal to 1, normalising the signals as $(u(t) - \overline{u})/\sigma_u$ and $(v(t) - \overline{v})/\sigma_v$. The spectra are plotted against the non-dimensional frequency $fH/\overline{u}$. Between tree crowns (panels 4.6a and 4.6b), the spectra in the vegetated canyon result shifted towards higher frequencies with respect to those calculated in the empty canyon. This suggests that the vegetation inhibits the formation of large-scale eddies. As a result, the energy transport is primarily driven by turbulent structures smaller than the transverse spacing between the tree rows W_{trees}, thus by length scales reflecting the canopy geometry (Poggi et al., 2004). The spectral content corresponding to W_{trees} can be read on the spectrum as the energy associated to the non-dimensional frequency $f'H/\overline{u} = 2.2$, where f' is the frequency corresponding to W_{trees}, calculated as $f' = \overline{u}/W_{trees}$. Moreover, in the presence of trees, the spectra do not exhibit a -5/3 Kolomogorov scaling in the inertial range. In the empty canyon, the spectra show an increase in energy associated with length scales larger than the canyon height (non-dimensional frequency smaller than 1), indicating that the turbulent flow is influenced by typical length scales of the inertial region of the external boundary layer (where the non-dimensional frequency associated with H is approximately

$f_H z/\overline{u} \simeq 4$, being $f_H = \overline{u}/H$, as shown in the spectra S_u, S_v, and S_w of Fig. 2.5). Additionally, the spectra reveal the presence of superstructures that develop along the longitudinal direction of the canyon. Also without trees, the slope of spectra deviates from the -5/3 law, due to possible local production of t.k.e. at intermediate scales, induced by the generation of velocity gradients at the canyon boundaries. Above the tree crowns (panels 4.6c and 4.6d), both S_u and S_v cover the same range of frequencies and their slope is approximately -5/3, regardless of the presence of trees. The superposition between spectra suggests that the effect of trees on the energy transport is no more detectable at the canyon rooftop.

4.3.2 Large street canyon: H/W_w=0.5

In the large ($W_w = 2H$) canyon without trees, the mean longitudinal velocity (Fig. 4.7a) is relatively uniform up to approximately $0.15W_w$ from the lateral walls. Beyond this distance, the velocity decreases due to the influence of the walls. The transversal velocity $\overline{v}/U_\infty$ (panel 4.7b) remains close to zero – with the spatial average of $\overline{v}/U_\infty$ in the cross-section equal to 0.006 –, indicating good alignment between the canyon and the external boundary layer. Values of σ_u/U_∞ (panel 4.7c) exhibit an almost symmetric spatial pattern, with intensities of 0.08 and 0.06 in the upper and lower corners, respectively, and around 0.07 in the center of the cross-section. The σ_v/U_∞ (panel 4.7d) shows a similar pattern to that observed in the square canyon (Fig. 4.4d), but with slightly higher values (around 0.05) at the centre of the canyon. The skewness values Sk_u and Sk_v are close to zero throughout the entire section (see panels 4.7e,f) and Ku_u (panel 4.7g) is homogeneous, with a value of 3, confirming the Gaussian distribution of u in the non-vegetated canyon, as observed in the square canyon. The skewness values Sk_u are close to zero throughout the entire section (see panel 4.7e), while Sk_v has slightly negative values around -1 in the lower left corner of the canyon (4.7f). The Ku_u (panel 4.7g) is 3 almost in the whole cross-section and 6 along the transversal profile at z/H=0.2, similarly to what found in the empty square canyon (Fig. 4.4g). The kurtosis of v (panel 4.7h) shows a heterogeneous pattern (similar to that observed in Fig. 4.4h). It is equal to 3 at the rooftop, while it peaks at approximately 30 in the lower left corner and around 15 in the lower right corner and along the lateral walls. The

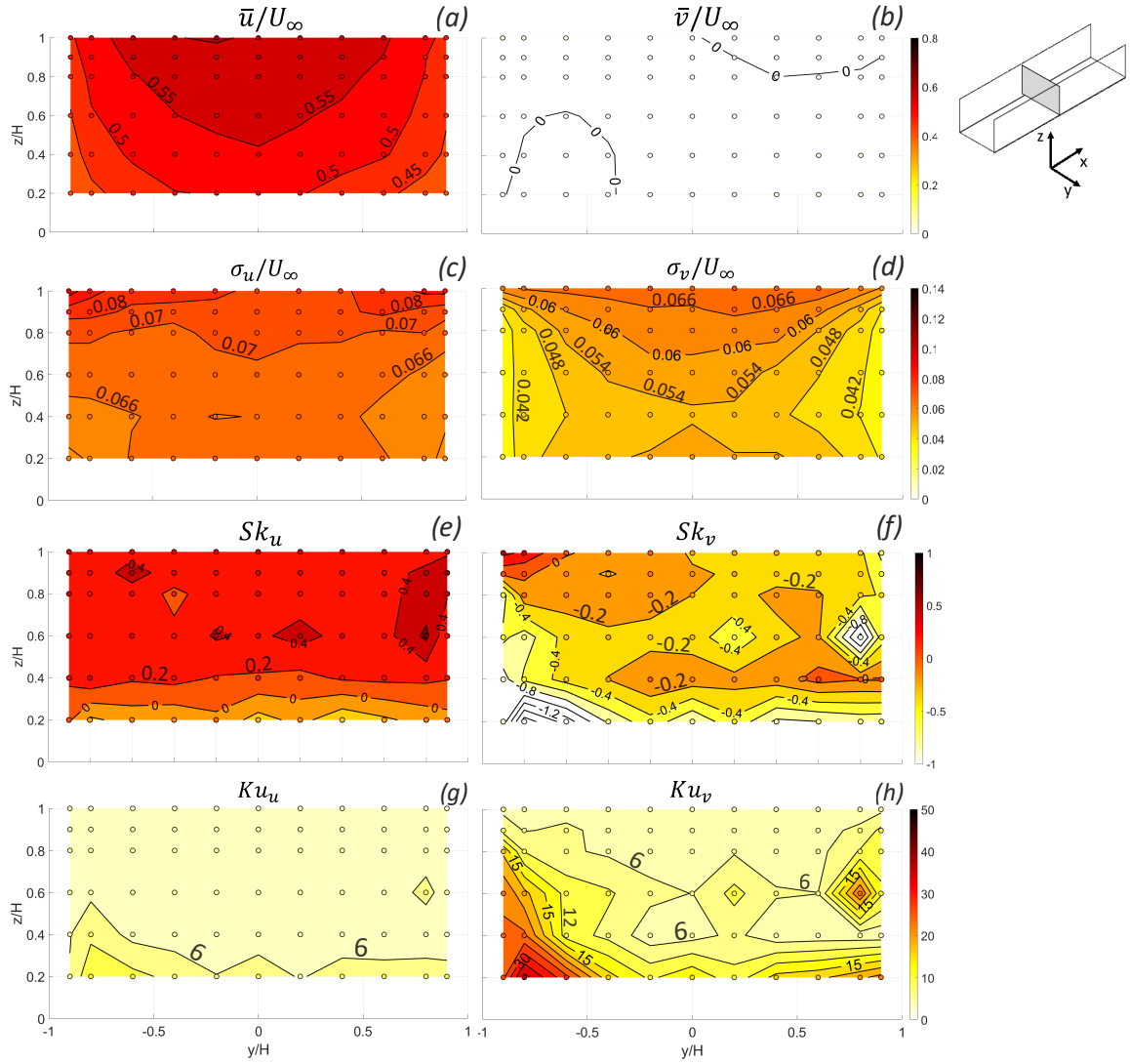


Figure 4.7 Transversal behaviour, in the large canyon and in the Zero configuration, of the mean longitudinal velocity (a), mean transversal velocity (b), longitudinal velocity standard deviation (c), transversal velocity standard deviation (d), longitudinal velocity skewness (e), transversal velocity skewness (f), longitudinal velocity kurtosis (g), and transversal velocity kurtosis (h).

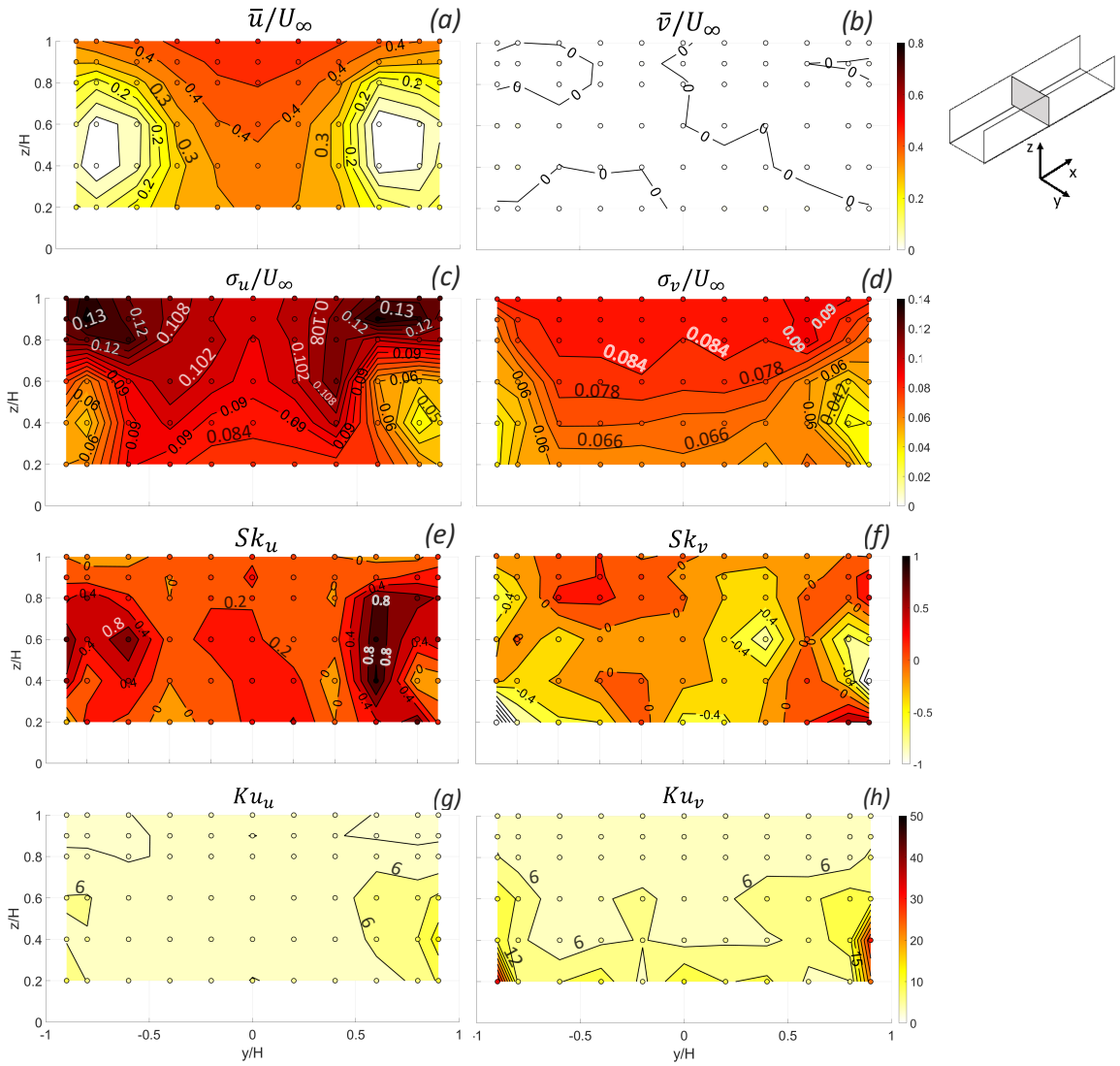


Figure 4.8 Transversal behaviour, in the large canyon and in the Full configuration, of the mean longitudinal velocity (a), mean transversal velocity (b), longitudinal velocity standard deviation (c), transversal velocity standard deviation (d), longitudinal velocity skewness (e), transversal velocity skewness (f), longitudinal velocity kurtosis (g), and transversal velocity kurtosis (h).

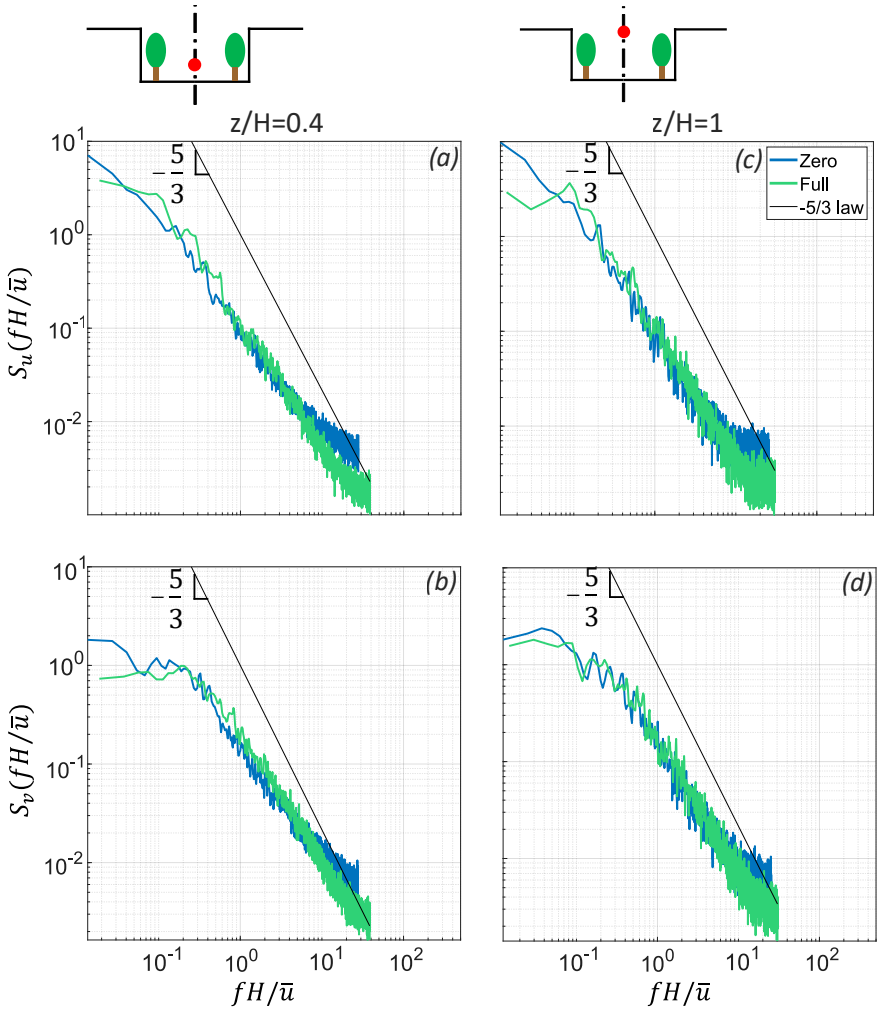


Figure 4.9 Spectra of $(u(t)-\overline{u})/\sigma_u$ and $(v(t)-\overline{v})/\sigma_v$, measured along the vertical axis of the canyon (y/H=0), at z/H=0.4 (a,b) and z/H=1 (c,d), in the large canyon. The black line refers to the -5/3 law. The positions where the spectra where calculated are represented with the red dot in the sketches above the panels.

high values of Sk_v, Ku_u, and Ku_v are reasonably linked to the sensibility of high-order statistics to the change in aspect ratio at the entrance of the reference canyon, to be added to the sensibility to tiny errors in the experimental setup, as already mentioned for the square canyon.

In the tree-lined large canyon, the trees do not occupy the entire transverse section, creating a vegetation-free corridor in the central area. In this corridor, the mean longitudinal velocity (Fig. 4.8a) is 25% lower than in the empty large canyon, and 70% higher than in the areas between the trees in the square canyon. Conversely, around the trees, $\overline{u}/U_\infty$ drops sharply to zero, as observed in the square canyon (see white areas in figure 4.5a). The spatial average of the mean longitudinal velocity in the vegetated large canyon $U_{tr,exp} = 1.39$ ms^{-1} ($U_{tr,exp}/U_\infty = 0.28$) is nearly half that of the empty large canyon ($U_{exp} = 2.63$ ms^{-1} and $U_{exp}/U_\infty = 0.53$). This difference is smaller than the one observed between the empty and vegetated square canyons. A considerable heterogeneous pattern also characterises the velocity standard deviation: both σ_u/U_∞ and σ_v/U_∞ are reduced around the trees but higher above the tree crowns and in the vegetation-free corridor compared to the empty large canyon. Above the tree crowns, σ_u/U_∞ (panel 4.8c) reaches 0.13, while in the centre of the canyon, it shows a monotonic vertical decrease from 0.1 at the rooftop to 0.08 at the ground. Examining the spatial pattern of σ_v/U_∞, the influence of the trees is again evident, with values of 0.04 near the canyon walls and 0.09 and 0.06 in the upper and lower parts of the vegetation-free corridor, respectively. The increase in velocity turbulent fluctuations, observed in the vegetation-free corridor, is likely due to sparser vegetation cover in the transverse direction, which enhances the surface roughness and hence turbulence generation within the large canyon (Zhao et al., 2023b; Peltola et al., 2025), resulting in more efficient turbulent mixing compared to the square canyon. The presence of trees has not a unique enhancing effect on the third and fourth moments, as we observed in the square vegetated canyon, since the presence of trees attenuates some high values of skewness and kurtosis caused by imperfections in the canyon geometry and wind-canyon misalignment. The skewness of u (Fig. 4.8e) increases to 0.8 around the trees, as we observed in the square vegetated canyon, while it is not possible to identify a clear imprint of trees in the Sk_v pattern (Fig. 4.8f). The kurtosis of u (Fig. 4.8g) shows values equal to 3 across the most of the cross-section and it slightly increases to 6 around the right-hand tree and in

a smaller area around the left-hand tree. The skewness and the kurtosis of u shows typical Gaussian distribution values in the vegetation free-corridor. The Ku_v (Fig. 4.8h) exhibits a quite heterogeneous pattern: it is equal to 3 and 6 at the rooftop and in between the trees, respectively, and it reaches approximately 10 at z/H=0.2 and around 15 in the lower left and right corners. In contrast to what observed in the square vegetated canyon, the Ku_v in the lower left corner of the large vegetated canyon is lower than in the empty large canyon and these intensities are comparable in the lower right corner.

In Fig. 4.9, we present the power spectral density of $(u(t) - \overline{u})/\sigma_u$ and $(v(t) - \overline{v})/\sigma_v$ calculated in the centre of the canyon, at z/H=0.4 (panels 4.9a,b) and z/H=1 (panels 4.9c,d). For both S_u and S_v, the spectra from the empty and vegetated canyons show good overlap at both z/H levels, in contrast to the differences observed at $z/H = 0.4$ in the square canyon (see Fig. 4.6a,b). This suggests that the influence of trees on the energy spectral content in a large canyon is confined to the lateral walls, becoming weaker toward the centre of the canyon. Regardless of the presence of trees, the largest energy content of S_u and S_v is associated to length scales larger than H, as observed in the empty square canyon. As we observed in the square canyon, the spectra show a slope different from -5/3 at z/H=0.4 and they get closer to the -5/3 Kolmogorov scaling at the rooftop.

4.4 Results: analytical modeling

The aim of this section is twofold. First (Sect. 4.4.1), we use data from the empty canyon to evaluate the predictions of the analytical model by Soulhac et al. (2008), which describes the spatial distribution of the mean velocity across the canyon section. This analytical model has been validated by comparison with results from numerical simulation performed with the Reynolds-Averaged Navier–Stokes model MERCURE. In the present study, we present the first comparison with experimental data. Next (Sect. 4.4.2), we apply data from the vegetated canyons to estimate the friction coefficients associated with the drag exerted by trees on the canyon flow. In this second analysis, we focus solely on the bulk flow velocity, averaged across the canyon section. The development

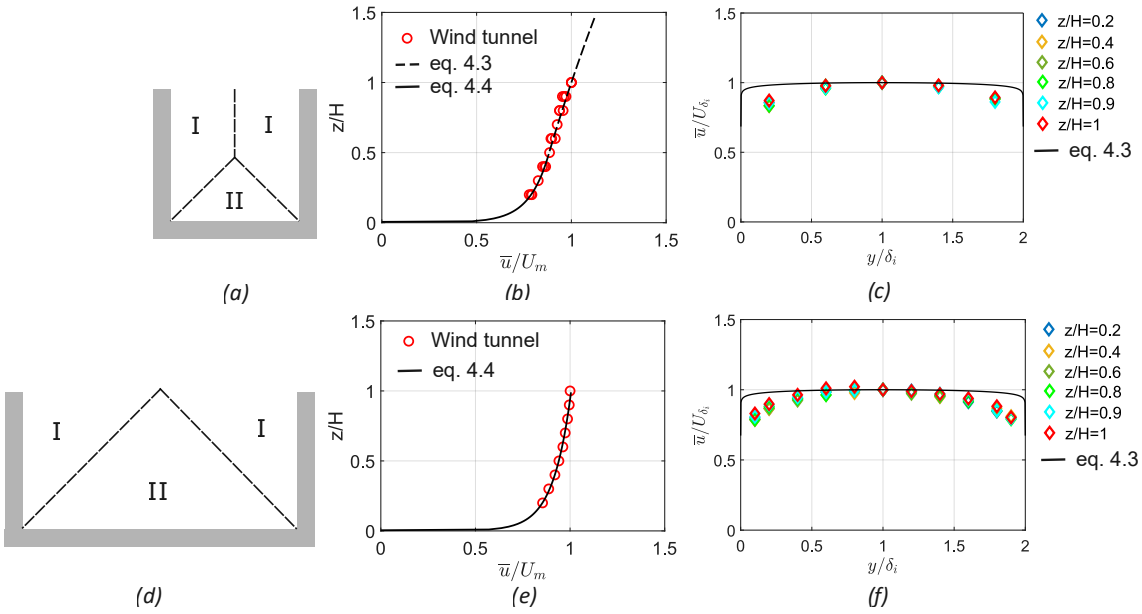


Figure 4.10 (a) Sketch of the partition of the flow in the square canyon according to the analytical model. Comparison between the vertical profiles of $\overline{u}/U_m$ acquired in the centre of the canyon (y/H=0), at the longitudinal positions x/H={0,4.4,11}, with Eqs. 4.3-4.4 (b) and of the horizontal profiles of $\overline{u}/U_{\delta_i}$ with equation (4.3) (c). (d) Same sketch as (a) for the large canyon. Vertical (e) and horizontal (f) experimental profiles, measured in the large canyon, overlapped with Eqs. 4.4 and 4.3, respectively

of a more detailed model for the mean velocity's dependence on the spatial coordinate within a vegetated canyon will be the subject of future work.

4.4.1 Empty canyon

The model by Soulhac et al. (2008) provides an analytical solution for the mean longitudinal velocity $\overline{u}(y, z)$ within an indefinitely long two-dimensional canyon parallel to the external flow, as a function of the canyon geometry and the roughness of the walls (z_i). The main assumptions of the model are: (i) the mean velocity field within a canyon, having height H and width W, is governed by turbulent entrainment at roof level of momentum from the external boundary layer, (ii) the longitudinal pressure gradient is negligible, i. e. $\partial p/\partial x = 0$, and (iii) no transverse components of the flow are considered. To model the spatial distribution of $\overline{u}(y, z)$, the flow within the canyon is divided into two regions (see Figs. 4.10a and 4.10d for the square and large canyons,

respectively): Region I, where the flow is influenced by the side walls, and Region II, where the flow is influenced by the ground. The flow dynamics in Region I and II are assumed independent of each other and influenced by the nearest rigid boundary, only. The no-slip condition is imposed on the canyon walls and floor, thus the interaction between the mean flow and the canyon walls generates boundary layers, whose thickness δ_i depends on the canyon geometry, according to the relation $\delta_i = \min(H, W/2)$. Based on assumptions (i), (ii), and (iii), the longitudinal component of the Reynolds-Averaged Navier-Stokes equation writes

$$\frac{\partial \overline{u'v'}}{\partial y} + \frac{\partial \overline{u'w'}}{\partial z} = 0. \tag{4.1}$$

By solving Eq. 4.1 using the gradient-diffusion approach to model Reynolds stresses and applying the method of separation of variables, the time-averaged longitudinal velocity in Region I (i.e., $z > \delta_i$) is given by:

$$\frac{\overline{u}(y,z)}{U_m} = f\Big(\frac{y + W/2}{\delta_i}\Big) g\Big(\frac{z}{\delta_i}\Big), \tag{4.2}$$

where U_m is the mean longitudinal velocity at the centreline of the rooftop (i.e., $y = \delta_i$ and $z = H$) and the g and f functions are the vertical and horizontal profiles of $\overline{u}/U_m$, respectively. The functions f and g read

$$\begin{cases} f\big(\frac{y+W/2}{\delta_i}\big) = \frac{J_1(C)Y_0\Big(\frac{C(y+W/2)}{\delta_i}\Big) - J_0\Big(\frac{C(y+W/2)}{\delta_i}\Big)Y_1(C)}{J_1(C)Y_0(C) - J_0(C)Y_1(C)} \\ g\big(\frac{z}{\delta_i}\big) = \exp\Big[\frac{C}{\sqrt{2}}\Big(\frac{z}{\delta_i} - \frac{H}{\delta_i}\Big)\Big] \end{cases} \tag{4.3}$$

where J_0, Y_0, J_1, and Y_1 are Bessel functions, C is a constant, H is the canyon height, and W is the canyon width. In Region II ($z \leq \delta_i$), the mean longitudinal flow is modeled as a boundary layer over a rough wall

$$\frac{\overline{u}(z)}{U_m} = \frac{u_*^s}{\kappa} \ln\Big(\frac{z}{z_i}\Big) \tag{4.4}$$

where κ=0.4 is the von Kármán constant, z_i is the wall roughness, and u_*^s is the friction velocity at ground level, obtained forcing the profile of Region II matching the one of Region I, at the interface between the two regions

$$u_*^s = \frac{\kappa}{\ln\big(\frac{\delta_i}{z_i}\big)} \exp\Big[\frac{C}{\sqrt{2}}\Big(1 - \frac{H}{\delta_i}\Big)\Big]. \tag{4.5}$$

By using Eq. 4.2-4.5, the average mean longitudinal velocity in the cross-section of the canyon

$$U_{an} = \frac{1}{HW}\int_0^H \int_{-W/2}^{W/2} \overline{u}(y,z)dydz, \tag{4.6}$$

reads (Soulhac et al., 2008)

$$U_{an} = U_m \frac{\delta_i^2}{HW}\Big[\frac{2\sqrt{2}}{C}(1-\beta)\Big(1-\frac{C^2}{3}-\frac{C^4}{45}\Big)+\frac{\beta(2\alpha-3)}{\alpha}+\Big(\frac{W}{\delta_i}-2\Big)\Big(\frac{\alpha-1}{\alpha}\Big)\Big] \tag{4.7}$$

where α and β are equal to

$$\begin{cases} \alpha = \ln\big(\frac{\delta_i}{z_i}\big) \\ \beta = \exp\big[\frac{C}{\sqrt{2}}\big(1-\frac{H}{\delta_i}\big)\big]. \end{cases} \tag{4.8}$$

The analytical model is here compared with the experimental vertical and horizontal profiles of $\overline{u}$, measured in the non-vegetated square and large canyons. We used three vertical profiles of $\overline{u}$, measured in the centre of the square canyon at different x-positions (i.e. the blue profiles in Fig. 4.3d), and one profile measured in the centre of the large canyon. The experimental vertical profiles of $\overline{u}$ are normalised by $U_m = \overline{u}(y/H = 0, z/H = 1)$. The horizontal profiles are extracted from the cross-sections (Fig. 4.4a and 4.7a) and normalised by the mean longitudinal velocity at $y = \delta_i$ at each z level (denoted as U_{δ_i}). The comparison is made by fitting the experimental profiles to the analytical ones, with the unknown parameters C and z_i, treated as free parameters.

In the square canyon (Fig. 4.10b), we found a good agreement between the experimental vertical profiles of $\overline{u}/U_m$ and the analytical model, with $C = 0.18$ and $z_i = 1.01 \cdot 10^{-5}$ m. Conversely, when maintaining the same C and z_i, the experimental horizontal profiles of $\overline{u}/U_{\delta_i}$ do not overlap with the model close to the canyon boundaries (Fig. 4.10c).

A possible explanation for these discrepancies is twofold: first, the canyon walls lack significant aerodynamic roughness, and second, the presence of slight pressure gradients. Both factors challenge the foundational assumptions of the model, as they prevent the application of the method of separation of variables used to solve the RANS equation (Eq. 4.1). This method, which establishes a relationship between the f and g functions through the constant C, may

not hold under the experimental conditions of this study. The smooth nature of the canyon walls is evident from the small value of the roughness length ($z_i = 1.01 \cdot 10^{-5}$ m), which provides the best fit to the experimental data. The Reynolds number based on the wall roughness $Re_r = u_*^s z_i/\nu \simeq 0.1$ (being u_*^s the friction velocity at ground level, modeled with Eq. 4.5) is indeed lower than the typical Re_r of a fully rough turbulent flow (Snyder and Castro, 2002). To investigate the presence of potential pressure gradients, we calculated the two terms of the divergence of the stress tensor $\partial\overline{u'v'}/\partial y$ and -$\partial\overline{u'w'}/\partial z$ (see Eq. 4.1) along a single vertical profile in the centre of the canyon. Our analysis revealed slight discrepancies between the two profiles, indicating the presence of a modest pressure gradient in the range $-0.6 < dp/dx < -0.05$ Pa m^{-1} along the wind tunnel. These findings align with the subtle variations in U_∞ observed along the wind tunnel axis (see Sect. 2.4).

By integrating the model across the entire cross-section of the canyon, Soulhac et al. (2008) derive an analytical equation for the average mean longitudinal velocity in the cross-section of the canyon U_{an}. Given the canyon geometry, along with the previously obtained values of U_m, C, and z_i, the analytical solution provides $U_{an} = 2.32$ ms^{-1} for the square canyon. This value is in close agreement with the experimental $U_{exp} = 2.39$ ms^{-1} (reported in Sect. 4.3.1), which is obtained by integrating the available point measurements across the cross-section, excluding data near the canyon walls that could not be measured due to instrument constraints. To improve the accuracy of U_{exp}, an attempt was made to extrapolate the missing data near the canyon boundaries using a logarithmic law, applying the no-slip condition at the walls. After this operation, the experimental U_{exp} becomes 1.96 ms^{-1}, which is 15% lower than the analytical U_{an}. This result indicates that the model provides a reliable estimate of the average mean longitudinal velocity in the cross-section of the canyon. The discrepancy between U_{exp} and U_{an} can be attributed to differences between the analytical and experimental horizontal profiles of $\overline{u}/U_m$ near the canyon walls, as well as uncertainties in the extrapolation of the missing experimental data.

With the same procedure, we tested the model in the large canyon. Figure 4.10e shows a good overlap between the experimental $\overline{u}/U_m$ profile and the analytical model with $z_i = 2.4 \cdot 10^{-5}$ m, which is slightly larger than the value estimated for the square canyon. The excellent match between the experimental

Table 4.1 Estimated pressure loss coefficients from different literature studies. The values are reported at full scale

References	λ_t [m^{-1}] H/W=1	λ_t [m^{-1}] H/W=0.5
This study	0.014	0.004
Majumdar et al. (2025)	0.0085	0.0025
Gromke and Ruck (2012)[a]	[0.53,1.33]	[0.53,1.33]
Jeanjean et al. (2015)[b]	[0.11,0.65]	[0.11,0.65]

[a]This study provides values of λ_t varying the vegetation porosity.
[b]This study provides values of λ_t varying the Leaf Area Density.

and analytical vertical profiles supports further the assumption that the flow within the canyon can be divided into two regions: Region I, influenced by the side walls, and Region II, influenced by the floor. Furthermore, it confirms that the thickness of the internal boundary layers depends on the canyon's aspect ratio. However, when examining the horizontal profiles of $\overline{u}/U_{\delta_i}$ (Fig. 4.10f), we observe that the experimental data do not align with the analytical model near the lateral walls (the possible reasons are the same as those indicated above for the square canyon).

The analytical U_{an} in the large canyon is 2.42 ms^{-1}, which is only 5% higher than the experimental $U_{exp} = 2.30$ ms^{-1}, calculated after having extrapolated the missing data near the canyon walls using a logarithmic law. The agreement between the experimental and analytical spatially-averaged mean longitudinal velocity is better in the large canyon compared to the square canyon. This is likely because, as the H/W ratio decreases, the discrepancy between the model and experimental mean velocity near the lateral walls becomes less significant in influencing the overall mean velocity across the entire cross-section

4.4.2 Vegetated canyon

To quantify the global impact of trees on airflow, we assess the bulk momentum balance—considering averaged quantities across the canyon section—per unit length along the canyon axis. This evaluation follows the methodology outlined by Soulhac et al. (2008). Specifically, under the assumptions (i), (ii), and (iii)

detailed in Sect. 4.4.1, the momentum budget is expressed as:

$$W\tau_H - \frac{1}{2}HW\rho_a\lambda_w U_{tr,exp}^2 - \frac{1}{2}HW\rho_a\lambda_t U_{tr,exp}^2 = 0 \tag{4.9}$$

where $\tau_H = u_*^2\rho$ is the shear stress exerted by the external flow at $z = H$, ρ_a is the air density, λ_w is the pressure loss coefficient of the building walls, λ_t is the pressure loss coefficient of the trees (Buccolieri et al., 2009; Gromke and Ruck, 2012; Zhao et al., 2023a), and $U_{tr,exp}$ is the average mean longitudinal velocity in the cross-section of the vegetated canyon, calculated averaging measurements linearly interpolated on a 5 mm resolution grid, to which zero velocity values were added at the canyon wall. The parameter λ_w, in Eq. 4.9, can be estimated from the momentum balance equation for the empty canyon (thus setting $\lambda_t = 0$ m^{-1} and U_{exp} equal to 1.96 ms^{-1} and 2.30 ms^{-1} in the square and large canyons, respectively):

$$\lambda_w = \frac{2u_*^2}{HU_{exp}^2} \tag{4.10}$$

providing λ_w equal to 0.32 m^{-1} for the square canyon and 0.24 m^{-1} for the large canyon. The parameter λ_t characterising our model trees cannot be retrieved from the experiments, thus we estimate it as a function of $U_{t,exp}$, u_*, and H. Rearranging terms in the momentum balance (4.9), we obtain the following expression for the parameter λ_t:

$$\lambda_t = \frac{2u_*^2 - HU_{tr,exp}^2\lambda_w}{U_{tr,exp}^2 H} \tag{4.11}$$

where $u_* = 0.25$ ms^{-1} and $U_{tr,exp}$ is equal to 0.64 ms^{-1} and 1.12 ms^{-1}, for the square and large canyons, respectively. Substituting these values, we obtain $\lambda_t = 2.73$ m^{-1} in the square canyon and $\lambda_t = 0.76$ m^{-1} in the large canyon. We observe that λ_t decreases with decreasing fraction of the cross-section of the canyon occupied by trees. In Table 4.1, we compare our estimates of λ_t with those reported in other studies. To do this, we need to convert our results at full-scale (Gromke and Ruck, 2012; Zhao et al., 2023a). Since the scale of the experiment is 1:200, we obtain $\lambda_t = 0.014$ m^{-1} in the square canyon and $\lambda_t = 0.004$ m^{-1} in the large canyon.

The experimental estimate of λ_t can be compared to those calculated applying the analytical model by Majumdar et al. (2025) to our vegetation

canopy in the canyons. This model estimates the drag exerted by trees on a turbulent flow. It accounts for the horizontal momentum balance within a homogeneous vegetation canopy, considering velocity and pressure gradients, as well as the drag from the vegetation. According to Majumdar et al. (2025), in a longitudinally homogeneous flow, λ_t can be expressed as

$$\lambda_t = \frac{2c}{l_d}, \tag{4.12}$$

where l_d is the length of the tree drag, $c = \langle \overline{u}^2 \rangle_{yz} / U_{t,exp}^2$ and $\langle \overline{u}^2 \rangle_{yz}$ indicates the spatial average over the cross-section of the vegetated canyon of the mean longitudinal velocity squared. Assuming a same form for the advective term and longitudinal pressure gradient, the parameter l_d can be directly expressed as a function of the aerodynamic porosity:

$$l_d \Big[1.27 + 0.55 \Big(\frac{WH}{l_d^2} \Big)^{0.33} \Big] = -\frac{2L_T}{\ln(\alpha_t^2)} \tag{4.13}$$

where L_T is the length of the tree canopy and α_t is the aerodynamic porosity. To compare our estimates to those provided by Eq. 4.12, we assume that the cross-sections of the vegetated square and large canyons are similar to a homogeneous vegetation canopy of unit length, characterized by an homogeneous aerodynamic porosity. Since the aerodynamic porosity could not be estimated directly, we calculated the optical porosity ($\alpha_{op,c}$) of the vegetated cross-section and we exploited the empirical relation $\alpha_t = \alpha_{op,c}^{0.4}$, obtained by Guan et al. (2003) for infinitely long three-dimensional windbreaks. The optical porosity of the vegetated cross-section was then estimated as

$$\alpha_{op,c} = \frac{HW - [2(1 - \alpha_{op,t}) H_T W_T]}{HW} \tag{4.14}$$

where H_T is the height of the model tree crown, W_T is the crown width, and $\alpha_{op,t} = 0.05$ is the optical porosity of the single model tree used in this study (Fellini et al., 2022). We obtained $\alpha_t = 0.72$ and $\alpha_t = 0.88$, for the square and large canyon, respectively. According to Eq. 4.13, we obtain $l_d = 2.29$ m and $l_d = 5.82$ m in the square and large canyons, respectively, and with Eq. 4.12 we evaluated $\lambda_t = 1.7$ m^{-1} and $\lambda_t = 0.5$ m^{-1} (with $c = 1.93$ in square canyon and $c = 1.48$ in the large canyon). These values (reported at full-scale in Table 4.1) are very similar to our experimental estimates, even though the trees being

placed within an urban canyon. The discrepancies between the two estimates are likely due to uncertainties in the aerodynamic porosity estimate, as well as the fact that we neglected possible pressure and velocity gradients along the street canyon.

Other useful comparisons can be made with the results from Gromke and Ruck (2012) and Jeanjean et al. (2015). Gromke and Ruck (2012) modeled the aerodynamic effects of trees in wind-tunnel experiments using a porous foam material, assessing the material's aerodynamic characteristics through the pressure loss coefficient. They found a pressure loss coefficient at full-scale equal to 0.53 m^{-1} for a pore volume fraction of 97.5% and equal to 1.33 m^{-1} for a pore volume fraction of 96%. Jeanjean et al. (2015) conducted CFD simulations to assess the effect of trees on pollution dispersion in the city of Leicester. They expressed the pressure loss coefficient at full scale as the product of the drag coefficient and the Leaf Area Density of real trees, obtaining a value of 0.4 m^{-1}. The values of λ_t found in this study are significantly smaller than those reported by Gromke and Ruck (2012) and Jeanjean et al. (2015). However, λ_t values from this study and that of Gromke and Ruck (2012) cannot be directly compared, as they are estimated with different approaches. In particular, in Gromke and Ruck (2012), the λ_t is determined placing a foam material in a tube, thus forcing the flow passing through the material (Gromke, 2011). Conversely, in our study the trees are placed within a street canyon and the flow can pass trough the tree crowns or above them, therefore providing a pressure loss coefficient significantly lower than that estimated in forced flow conditions.

4.5 Conclusions to Chapter 4

This chapter presents the results of a wind-tunnel study designed to quantify the aerodynamic effects of trees on the turbulent flow field within a street canyon, aligned with the external wind. Flow velocity measurements were conducted in both an empty canyon and a canyon with two rows of trees along the lateral walls. Additionally, we investigated the influence of the canyon aspect ratio, considering both a square canyon H/W=1 and a large canyon H/W_w=0.5.

In the vegetated square canyon, the mean longitudinal velocity decreases by 80% around the tree crowns and by 25% above them, compared to the empty canyon. Consequently, the average mean longitudinal velocity in the cross-section U_{exp} drops by 70% from the empty to the vegetated canyon. In contrast, in the upper part of the canyon, the interaction between the trees and the external flow leads to a 30% increase in longitudinal velocity fluctuations and a 20% increase in transversal velocity fluctuations, while both are dampened around the trees. Additionally, the presence of trees causes local kurtosis values significantly greater than 3, particularly in the lower corners of the canyon. As the aspect ratio of the canyon decreases, a vegetation-free corridor forms between the tree rows, where the mean longitudinal velocity and turbulent velocity fluctuations are 70% and 40% higher than in the center of the vegetated square canyon, respectively. Additionally, the difference in U_{exp} between the vegetated and non-vegetated large canyons is reduced to 50%. The spectra of the longitudinal and transversal velocity signals, calculated in the square canyon, show that, within the tree rows, energy transport is dominated by turbulent structures smaller than the transversal spacing between the tree lines. Furthermore, the spectra in this region do not resemble Kolmogorov spectra. In contrast, in the centre of the large canyon, the effect of the trees on the energy spectral content is less pronounced, and the energy associated with different length scales is similar, regardless of the presence of trees.

The data measured in the empty square (H/W=1) and large (H/W_w=1) canyons were compared with the analytical model developed by Soulhac et al. (2008). A good agreement was found between the experimental vertical profiles of the mean longitudinal velocity and the model equations. However, even though using the same fitting parameters, the horizontal profiles of $\overline{u}$ did not match the analytical model near the canyon boundaries. Nevertheless, the difference between the experimental and analytical average mean longitudinal velocity in the cross-section was around 15% for the square canyon and 5% for the large canyon. Finally, we derived an expression for the pressure loss coefficient due to trees, which depends on the average mean longitudinal velocity in the cross-section of the vegetated canyon, the canyon height, and the friction coefficient of building walls. The coefficient λ_t was found to be 2.73 m^{-1} in the square canyon and to 0.76 m^{-1} in the large canyon. These values were derived by considering a momentum balance to the flow in the street canyon with

miniatures of trees, evaluating experimentally the average mean longitudinal velocity along the canyon. The obtained λ_t deviates from other literature studies due to the absence of the canyon walls in their models, different types of vegetation, and possible longitudinal pressure or velocity gradients, neglected in the momentum balance.

We reported the first comparison of the analytical model by Soulhac et al. (2008) with experimental data. The positive outcomes of the comparison regarding the spatial average mean longitudinal velocity along the canyon are an important results of this work. In fact, they reinforce the validity of using this analytical relation in the operational urban dispersion model SIRANE, to parameterize the advective flux along the street axis (Soulhac and Salizzoni, 2010; Soulhac et al., 2011). Furthermore, the SIRANE model does not account for the presence of obstacles within the streets (i.e., trees), thus our estimate of the pressure loss coefficient by means of experimental data may be a step forward to parametrize the mean advective flux along a vegetated streets.

From the analysis of the turbulent flow field, we can conclude that high-density tree boulevards, where the crowns are in close contact crosswise, significantly impede both the mean and turbulent flow within the canyon. This challenges the idea that a wind direction perpendicular to the canyon axis is the worst-case scenario for air quality in urban canyons. By reducing the height-to-width ratio, a sparser vegetation cover increases the surface roughness, leading to higher turbulent fluctuations and more efficient turbulent mixing in the centre of the larger canyon compared to the narrower one. These findings can be included in urban design strategies, to ameliorate the ventilation of urban street canyons. However, it is not possible to assess the effect of trees and canyon geometry on the efficiency of vertical momentum transport between the canyon and the external flow, as this study does not provide a characterization of the vertical velocity field. This limitation arises from the difficulty of introducing the Laser Doppler Anemometry system coupled with a mirror (necessary for measuring the vertical velocity component, w) into the vegetated canyon. In addition to vegetation density, several other factors influence ventilation within urban canyons, including street geometry, the presence of street intersections, and wind direction. The next chapter is aimed at exploring these aspects.

Chapter 5

Turbulent flow within a canyon with intersections for different wind directions

In the previous chapter, we questioned the idea that the orthogonal wind is the worst condition for the air quality. For example, we showed that, with street-axis parallel wind direction, the presence of trees reduces by 80% the mean longitudinal velocity within the vegetated canyon with respect to an empty canyon. This tree-induced effect may have consequences on the pollutant dispersion along the canyon. In this chapter, we extend our investigation to the turbulent flow field within vegetated canyons with oblique wind directions and in the presence of street intersections.

To our knowledge, only Gromke and Ruck (2012) conducted concentration measurements within an isolated street canyon with trees, considering wind directions of 0°, 45°, and 90° with respect to the canyon axis. They showed that, in a canyon with trees and small height-to-width ratio, a 45° wind direction causes average concentrations higher than those found within perpendicular and parallel canyons. However, this study investigated the effect of vegetation in simplified two-dimensional urban geometries, without considering street intersections. The complex three-dimensional flow within street intersections and its effects on the ventilation of street canyons without vegetation were analysed experimentally by few authors. The studies of Carpentieri et al. (2009)

and Carpentieri and Robins (2010) focused on a street intersection in London and they revealed that the complex three-dimensional flow field within the intersection influences the distribution of pollutant concentration within the streets, the horizontal pollutant fluxes between the intersection and the streets, and the vertical fluxes between the canopy and the external flow. Another wind-tunnel study by Garbero et al. (2010) showed that the wind direction and the street aspect ratio affect mass fluxes at the intersections, thereby the pollutant spreading within a street network. These results highlighted the necessity of including the flow dynamics in street intersections in operational urban dispersion models (Soulhac et al., 2009). However, these experimental works do not consider the presence of trees within the urban geometry.

The simultaneous influence of vegetation, wind direction, and street geometry on the pollutant dispersion within realistic urban neighborhoods was investigated in few studies, by RANS simulations (Buccolieri et al., 2011; Jeanjean et al., 2015). They highlighted that the aerodynamic influence of trees on the air quality within street canyons strongly depends on the wind direction, since it governs the interaction between the external flow and the buildings, thus the flow structure in the vegetated urban canopy (Buccolieri et al., 2018; Zhang et al., 2021). To our knowledge, when focusing on experimental approaches, only Carlo et al. (2024) have considered a realistic street with intersections and various types of vegetation. They performed mean concentration measurements within a canyon with intersections, perpendicular to the external wind, with obstacles of different size and porosity, including vegetation. Trees were found to weaken corner eddies more significantly than small obstacles (like cars or vegetation hedges), leading to peaks in the mean concentration at the pedestrian level. Confirmation of these results requires velocity measurements to accurately characterise the turbulent flow field within a vegetated canyon with intersections. Moreover, in this study, information about the effects of non-orthogonal wind directions is completely missing.

Therefore, in this chapter, we present the results of a wind tunnel experimental campaign performed to analyse the effects of vegetation, wind direction, and street intersections on the mean and turbulent flow field within a street canyon. The chapter is organized as follows. Section 5.1 presents the technical details of the experiment. Section 5.2 analyses the velocity field within the canyon without street intersections for different wind directions. Section 5.3

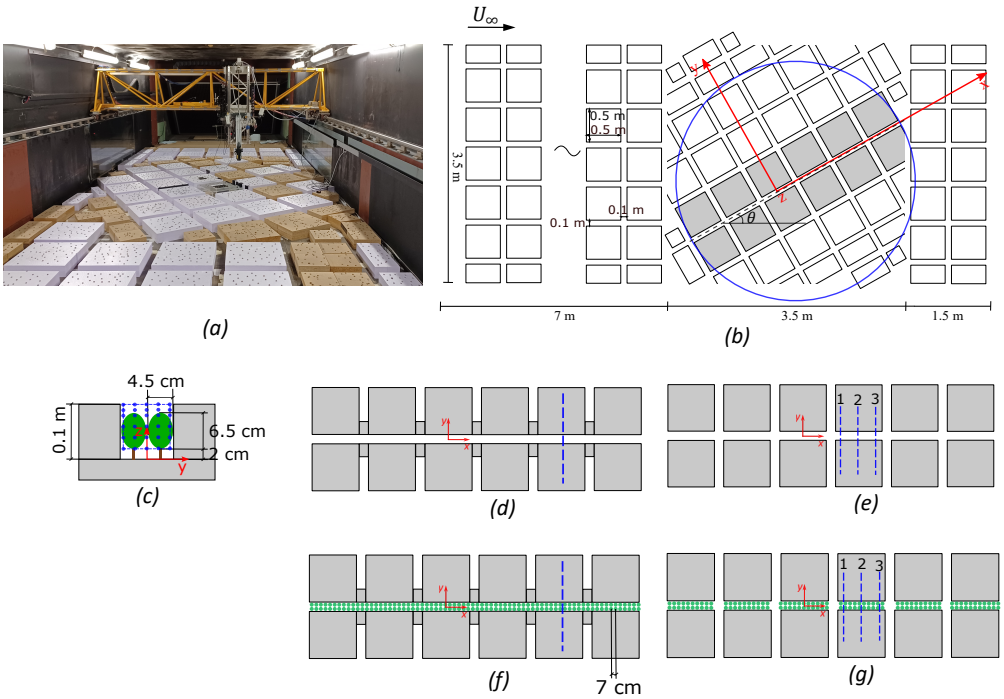


Figure 5.1 (a) Street network modeled in the wind tunnel (b) Scheme of the urban canopy in Configuration 2, with the reference street canyon rotated of 30° with respect to the external wind. The blocks confining the reference canyon are coloured grey. The red arrows represent the reference system of the reference street canyon and the blue circle the rotating platform. (c) Front view of the squared canyon with trees. Planar view of the empty canyon without intersections (d) and with intersections (e). Planar view of the vegetated canyon without intersections (f) and with intersections (g). The blue rectangle in panel (b) indicates the position of the measuring section in the transversal section of the canyon. The blue dotted line indicates the longitudinal position of the measuring cross-sections.

presents the velocity field within the street canyon with intersections. Finally, Section 5.3.4 provides insights into the ventilation within a street network. Conclusions are drawn in Section 5.4.

5.1 Experimental details

The urban street network modeled in the wind tunnel is reproduced according to the obstacle Configuration 2 (Fig. 2.1d). To investigate different wind directions, we selected a reference street canyon on the rotating platform, mounted on the floor of the test section of the wind tunnel (see blue circle in Fig. 5.1a). This

reference canyon is characterised by a square cross-section and it is $L = 3.5$ m long, thus it occupies the entire length of the rotating platform (canyon confined by grey blocs in Fig. 5.1b). Two geometries were investigated, maintaining a height-to-width ratio equal to H/W=1: an infinitely-long street canyon with confined lateral boundaries (with a length-to-height ratio of $L/H = 35$) and a street canyon composed of short streets bounded by street intersections (each of them with $L/H = 5$). We considered wind directions θ=0°, θ=30°, and θ=60°, being θ the angle between the approaching flow and the longitudinal axis of the reference canyon. Notice that only the reference canyon and the neighboring blocks which lay on the rotating platform are oriented with different angles with respect to the external wind (see panel 5.1a). The coordinate system were defined on the longitudinal axis of the reference canyon, $15H$ far from the entrance of the canyon, with the vertical axis starting at ground level. The x-, y-, and z-axes are oriented in the streamwise, transversal, and vertical directions, respectively (see the red arrows in Fig. 5.1b).

To simulate the aerodynamic effects of a homogeneous vegetation cover, we arranged the model trees along the entire length of the lateral walls of the reference canyon, leaving empty the street intersections in the laterally-opened configuration. For each canyon geometry, we considered an empty canyon (Zero configuration, Figs. 5.1d-e) and a vegetated canyon, with two parallel rows of trees spaced 7 cm apart (Full configuration, Figs. 5.1f-g). The Full configuration reproduces a high density tree boulevard with intersecting crowns, which is often found in European cities (Fig. 4.2).

Velocity measurements were acquired with the LDA, in different spatial points on vertical cross-sections of the canyon, with a horizontal resolution of 2 cm and a vertical resolution of 2 cm in the range $0.2 \leq z/H \leq 0.8$ and 1 cm in the range $0.8 \leq z/H \leq 1$. The velocity field within the canyon with closed lateral boundaries was analysed on a single cross-section, as the mean and turbulent flow fields result homogeneous along the x-axis (this is verified within the wind-aligned canyon in Sect. 4.2). This cross-section is located at a distance of about $20H$ from the entrance of the canyon, to avoid flow disturbances due to the misalignment of the blocks at the junction between the floor of the wind tunnel and the rotating platform, when investigating oblique wind directions (i.e., θ={30°,60°}). To investigate the effect of street intersections, we identified a street canyon of length $5H$ between two intersections, along the reference

canyon with opened lateral boundaries. In this laterally-opened canyon, flow velocity statistics were analysed on three cross-sections along the x-axis: cross-section 1 next to the upwind intersection, cross-section 2 in the middle of the street, and cross-section 3 next to the downwind intersection (the positions of the cross-sections are indicated in Fig. 5.1e and 5.1g).

5.2 Velocity field in a street canyon without intersections for different wind directions

We investigate the effects of the wind direction on the spatial patterns of flow velocity statistics and on the spatial average of the advective velocity, within empty and vegetated canyons, with closed lateral boundaries. In Sects. 5.2.1 and 5.2.2, we describe the mean and turbulent flow fields in the canyon, considering wind directions θ=0°, θ=30°, and θ=60°. For sake of comparison, we recall the main characteristics of the mean and turbulent flow fields within the wind-aligned square canyon, described in detail in the previous chapter (Sect. 4.3.1). The mean and the standard deviation of the longitudinal and transversal velocity are reported on two-dimensional cross-sections, obtained by linearly interpolating point measures. The velocity statistics are normalised by the free-stream velocity U_∞. In Sect. 5.2.3, we present the variation of the mean longitudinal velocity along the canyon as a function of the external wind direction.

5.2.1 Cross-sectional velocity field in the street canyon

Street axis-parallel wind direction

As described in detail in Sect. 4.3.1, when the wind is aligned with the empty street canyon, the mean velocity field is dominated by a longitudinal, axis-parallel flow. This flow reaches its maximum in the centreline of the rooftop and monotonically decreases to zero moving towards the lateral walls and the floor (Fig. 5.2a). The mean transversal velocity is zero on the whole cross-section of the canyon (Fig. 5.2b). Velocity turbulent fluctuations exhibit a symmetrical pattern with respect to the vertical axis of the canyon, with high intensity

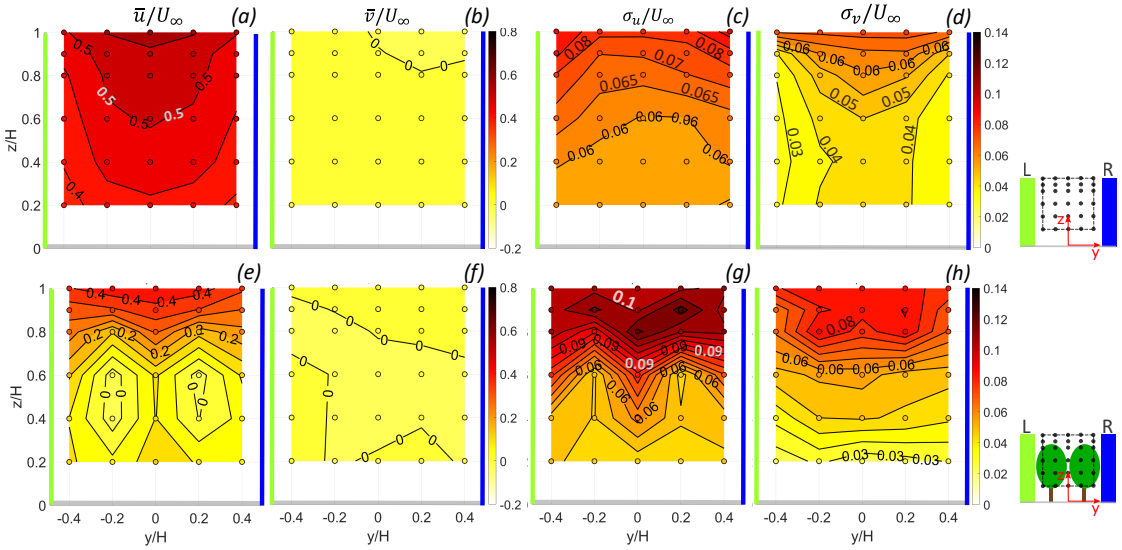


Figure 5.2 Transversal behaviour of the mean longitudinal velocity (a), mean transversal velocity (b), longitudinal velocity standard deviation (c), and transversal velocity standard deviation (d), within the empty canyon, with wind direction θ=0°. (e-h) Same as (a-d), but in the vegetated canyon. Green and blue colors indicate the left and right walls of the canyon (see sketches on the right).

at the rooftop and low intensity in the inner canyon. Notably, the σ_u/U_∞ (Fig. 5.2c) monotonically decreases from 0.08 at the rooftop to 0.055 close to the ground. The σ_v/U_∞ (Fig. 5.2d) is divided into two areas of almost homogeneous intensity: an upper area of intensity 0.07 and an area of intensity 0.04 inside the canyon, with lower values around 0.03 along the lateral walls. The high σ_v/U_∞ intensity at the rooftop of the canyon corresponds to a shear layer of about $0.1H$.

As discussed in Chapter 4, the aerodynamic effect of trees on the canyon flow is twofold: on the one hand, it hinders the mean longitudinal velocity inside the canyon, and on the other hand, it enhances surface roughness and promotes turbulence generation above the tree crowns. In fact, in correspondence of trees (at z/H=[0.2,0.6]), $\overline{u}/U_\infty$ (Fig. 5.2e) is almost zero, while above the tree crowns (z/H=[0.8,1]) it increases to 0.4, which is 25% lower than at the rooftop of the empty canyon. In panels 5.2g and 5.2h, we see that the interaction between the external flow and the top of tree crowns enhances σ_u/U_∞ and σ_v/U_∞ by 30% and 20%, respectively, with respect to the empty canyon. Conversely, the packed configuration of the vegetation inside the canyon leads to around 25% decrease of turbulent fluctuations with respect to the non-vegetated canyon.

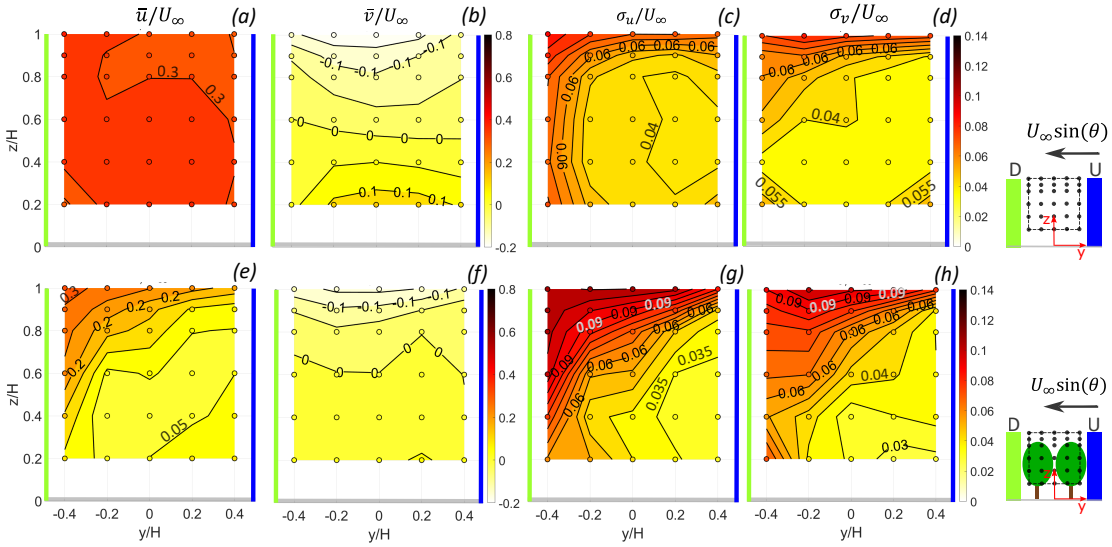


Figure 5.3 Transversal behaviour of the mean longitudinal velocity (a), mean transversal velocity (b), longitudinal velocity standard deviation (c), and transversal velocity standard deviation (d), within the empty canyon, with wind direction θ=30°. (e-h) Same as (a-d), but in the vegetated canyon. Green and blue colors indicate the downwind and upwind walls of the canyon (see sketches on the right).

Oblique wind direction

When the external wind is not aligned with the street axis, the flow field is characterised by the coexistence of a longitudinal and a transversal flow, that generates a helicoidal flow motion (Nakamura and Oke, 1988; Dobre et al., 2005; Soulhac et al., 2008; Zhang et al., 2021). The transversal flow exhibits a anti-clockwise recirculating structure, consisting of a transverse flow from the downwind wall (y/H=-0.5) to the upwind wall (y/H=+0.5) at the rooftop, which promotes the entrance of external air in the canyon at the downwind wall, and a reverse flow at the ground, followed by an upward flow along the upwind wall. The helicoidal flow structure is evident from Figs. 5.3a-b: with wind direction θ=30°, $\overline{u}/U_\infty$ (Fig. 5.3a) shows homogeneous values equal to 0.3, on the whole cross-section of the non-vegetated canyon and $\overline{v}/U_\infty$ (Fig. 5.3b) is characterised by a negative flow with velocity -0.1 at the rooftop, a positive flow with velocity +0.1 close to the ground, and zero mean transversal velocity in the canyon centre (at z/H=[0.4,0.6]). The transversal flows with opposite sign at the top and at the bottom of the cross-section confirm the presence of a recirculating flow structure which occupy the whole cross-section

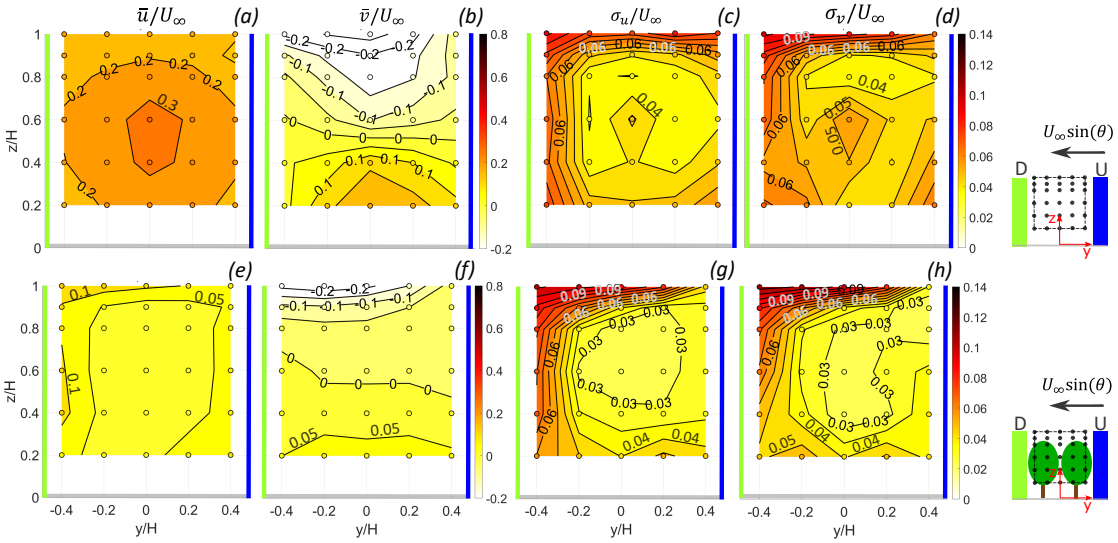


Figure 5.4 Transversal behaviour of the mean longitudinal velocity (a), mean transversal velocity (b), longitudinal velocity standard deviation (c), and transversal velocity standard deviation (d), within the empty canyon, with wind direction θ=60°. (e-h) Same as (a-d), but in the vegetated canyon. Green and blue colors indicate the downwind and upwind walls of the canyon (see sketches on the right).

of the canyon. This structure plays a key role in the ventilation of the street canyon, since it conveys fresh air from the external flow into the canyon and transports pollutants to the upwind wall, where part of them exits the canyon (Salizzoni et al., 2009; Gromke and Ruck, 2007; Fellini et al., 2022). However, in the canyon centre the flow field is dominated by an axis-parallel flow which could be responsible for an accumulation of pollutants along the canyon axis (Soulhac and Salizzoni, 2010; Gromke and Ruck, 2012; Zhang et al., 2021). With oblique wind direction, turbulent fluctuations exhibit a spatial pattern that is asymmetric with respect to the vertical axis of the canyon, contrary to what observed in the wind-aligned street canyon (Figs. 5.2c,d). The σ_u/U_∞ (Fig. 5.3c) distribution reveals two layers along the rooftop and the downwind wall, with thickness $0.1H$ and $0.2W$, respectively, where the intensity is equal to 0.06. Inside the canyon, σ_u/U_∞ sharply decreases to 0.04. The high longitudinal velocity fluctuations at the canyon rooftop, followed by a sharp decrease (equal to 30%) of them within the canyon, suggests the development of a shear layer of thickness $0.1H$, as observed with wind direction θ=0° (Fig. 5.2d). Moreover, the interaction between the canyon flow and the downwind wall may be responsible for turbulence generation along the downwind wall (Salizzoni et al., 2011). The

fluctuations of σ_v/U_∞ show intensities comparable to those of the longitudinal velocity fluctuations, but with a markedly different spatial pattern (see Fig. 5.3d). The shear layer is still detectable, as well as the homogeneous area of fluctuation intensity equal to 0.04 below the shear layer, but σ_v/U_∞ increases to 0.055 in the lower upwind and downwind corners of the cross-section.

In the vegetated canyon, trees hinder the mean flow between the tree crowns (i.e., $z/H<0.8$), thereby disrupting the helicoidal motion. The mean longitudinal velocity (panel 5.3e) shows an asymmetric pattern, in contrast to what is observed in the empty canyon. Notably, in the upper part of the cross-section, there is an area, of thickness $0.6H$ along the downwind wall, that progressively decreases to $0.1H$ moving towards the upwind wall, where $\overline{u}/U_\infty$ is equal to around 0.2, while inside the canyon $\overline{u}/U_\infty$ decreases to 0.05, thus 80% lower than in the non-vegetated canyon. The $\overline{v}/U_\infty$ (panel 5.3f) is maintained equal to -0.1 above the tree crowns (as observed at the rooftop of the empty canyon, in panel 5.3b), thanks to the influence of the external flow, but the reverse flow at ground level is inhibited. The spatial patterns of the longitudinal and transversal velocity standard deviation are similar to each other: they exhibit high fluctuation intensity at the rooftop and in correspondence of the downwind tree (y/H=[-0.4,0) and z/H=[0.2,0.8]) and low intensity in correspondence of the upwind tree (y/H=(0,0.4] and z/H=[0.2,0.8]). In particular, σ_u/U_∞ (Fig. 5.3g) is equal to 0.1 in the downwind upper corner (around 40% higher than in the empty canyon - panel 5.3c) and it decreases to 0.09 in the upwind upper corner and to 0.06 in the downwind lower corner. Inside the canyon, σ_u/U_∞ is equal to 0.06 around the downwind tree and to 0.03 around the upwind tree. The same spatial pattern and intensity are found for σ_v/U_∞ (Fig. 5.3h), except for lower intensity around 0.09 in the downwind upper corner. The high values of σ_u/U_∞ and σ_v/U_∞ in correspondence of the downwind tree with respect to the upwind tree suggest an interaction between the tree crowns and the external flow entering the canyon.

When the wind angle is increased to θ=60°, $\overline{u}/U_\infty$ exhibits a fast core at the canyon centre with a velocity of 0.3, decreasing by about 20% toward the edges of the cross-section (see Fig. 5.4a). The $\overline{v}/U_\infty$ (Fig. 5.4b) is two times faster than with θ=30° (Fig. 5.3b): $\overline{v}/U_\infty$ is equal to -0.2 at the rooftop and +0.2 close to the ground. In the central core of the canyon, the mean transversal velocity is equal to zero, thus an accumulation of pollutants along the x-axis of the canyon

could occur, due to the longitudinal velocity component. The spatial pattern of the statistics of the turbulent fluctuations is quite heterogeneous. The σ_u/U_∞ (Fig. 5.4c) shows two shear layers, at the rooftop and along the downwind wall, where the fluctuation intensity is similar to that found with θ=30° (Fig. 5.3c), while inside the canyon we see a central core of intensity 0.05 outside of which there is an area of intensity equal to 0.04 and a transversal profile of intensity equal to 0.05 close to the ground (at z/H=0.2). High fluctuation intensity in the central core can be detected also when analysing σ_v/U_∞ (Fig. 5.4d), while around it the spatial pattern is slightly different from that of σ_u/U_∞: the σ_v/U_∞ decreases to around 0.04 in the upper part of the cross-section (at z/H=0.8) and it slightly increases to 0.06 in the lower downwind and upwind corners of the cross-section.

When θ=60°, the presence of trees in the canyon also alters the helicoidal motion. The velocity $\overline{u}/U_\infty$ (Fig. 5.4e) is homogeneous and equal to 0.03 across the whole cross-section, thus 90% lower than in the empty canyon in the central core and 85% around it. At the cross-section edges we observe a slight increase of $\overline{u}/U_\infty$ to 0.1 in the upper downwind corner and along the downwind wall, and to 0.07, along the upwind wall. This asymmetry could be linked to small flow canalisation between the canyon walls and the trees of heterogeneous shape. The mean transversal velocity (Fig. 5.4f) is equal to around -0.2 above the tree crowns, with a slight decrease to -0.1 in the upwind upper corner, while it is zero within the canyon. However, a weak transversal flow towards the upwind wall, equal to around +0.07, is visible in correspondence of the tree trunks (i.e., along the transversal profile at z/H=0.2). Both σ_u/U_∞ (Figs. 5.4g) and σ_v/U_∞ (Figs. 5.4h) show a layer $0.1H$ thick with values equal to 0.09, at the rooftop, and a layer $0.2W$ thick with values around 0.06 along the downwind wall. Within the canyon, the presence of trees dampen the central core with high fluctuation intensity, observed in the empty canyon (Fig. 5.4c,d), and homogenizes σ_u/U_∞ and σ_v/U_∞ to values equal to 0.03 (40% lower than in the empty canyon). Slightly higher fluctuation intensity (around 0.045) can be detected in correspondence of tree trunks.

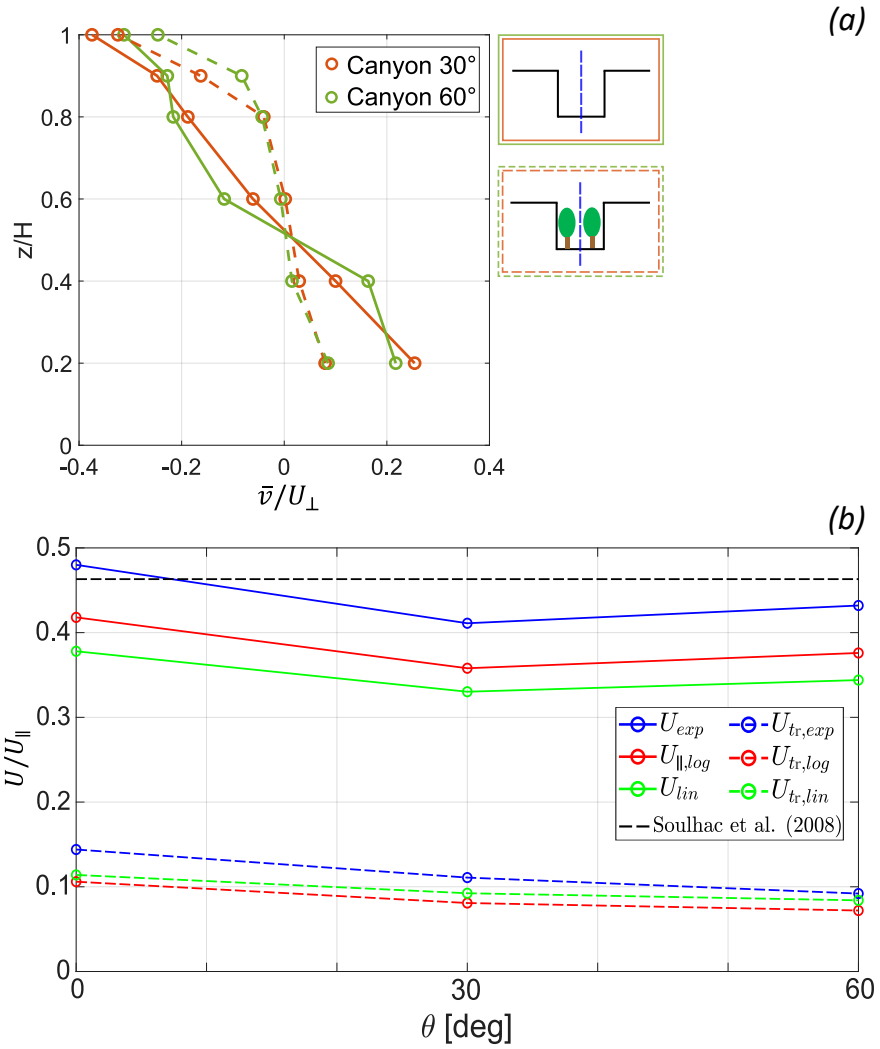


Figure 5.5 (a) Vertical profiles of the mean transversal velocity normalized by $U_\perp$ ($U_\perp = U_\infty \sin(\theta)$), measured in the centre of canyon. Continuous and dashed lines refer to the empty and vegetated canyon configurations, respectively. The different colors indicate to wind directions θ=30°(orange) and θ=60° (green). (b) Variation of the spatial average of the mean longitudinal velocity on the cross-section of the canyon (normalised by $U_\parallel = U_\infty \cos(\theta)$) with the wind direction. Continuous and dashed lines differentiate the U values obtained in the empty and vegetated canyon, respectively. The different colors refer to different spatial averaging methods.

5.2.2 Transversal velocity profiles

This section investigates how the vertical profile of the transversal velocity, which drives cross-canyon recirculation, depends on wind direction and vegetation configuration. In Fig. 5.5a, we report vertical profiles of the mean transversal velocity $\overline{v}$, measured in the centre (y/H=0) of the non-vegetated and vegetated canyons. The mean transversal velocity is normalized by the component of the free-stream velocity projected on the y-axis of the canyon ($U_\perp = U_\infty \sin(\theta)$). Only wind directions θ=30° and θ=60° are shown, since in the wind-aligned street canyon (θ=0°) the transversal velocity component is zero.

Without trees, the profiles collapse on a single curve, demonstrating that $\overline{v}$ scales with $U_\perp$, thereby that the transversal recirculation within the canyon is driven by the cross-wind component of the external flow (in line with the numerical simulations by Soulhac et al. 2008 and field measurements by Dobre et al. 2005). The vertical distribution of the profiles highlights a anti-clockwise recirculation in the canyon cross-section: the mean transversal velocity exhibits similar magnitude but opposite direction at the top and bottom of the profile and zero value in the centre (at y/H=0 and z/H=0.5), where the central core of the recirculating structure is located.

In the vegetated canyon, the scaling of $\overline{v}$ with $U_\perp$ is less evident above the tree crowns (z/H=[0.9,1]), due to the influence of the shape and spatial arrangement of trees, which may be sensitive to the wind direction. Conversely, the profiles show zero values between trees (z/H=[0.4,0.8]). A weak deviation from zero of the profiles can be detected in correspondence of the tree trunks (z/H=0.2), where $\overline{v}/U_\perp$ is equal to +0.08 with wind directions θ=30° and θ=60°. The large difference in the modulus of $\overline{v}/U_\perp$ between the top and the bottom of the profiles (around 70%), suggests that the recirculation is significantly dampened by the trees. At the canyon rooftop, the absolute values of $\overline{v}$ increases by 20% from θ=30°to θ=60°, approximately 20% lower than those at the rooftop of the empty canyon.

5.2.3 Cross section-averaged mean longitudinal velocity

This section is dedicated to the analysis of the variation of the transversally-averaged mean longitudinal velocity (U) with the wind direction θ, in the empty

and vegetated canyons. This quantity constitutes a key parameter in urban dispersion models, to model the advective flux along a urban canyon (Soulhac et al., 2011, 2013). In the previous chapter (Sect. 4.4), we evaluated U within a canyon parallel to the external flow (θ=0°), whilst in this section we provide an estimate of U with wind directions θ=0°, θ=30°, and θ=60°. The experimental value of U was calculated by averaging the $\overline{u}$ data, over the cross-sections of the empty and vegetated canyons. Three different averaging methods were applied:

(i) spatial average of the $\overline{u}$ measurements resampled onto a 5 mm resolution grid using linear interpolation and weighted by the cell associated to each measurement point – we denote by U_{exp} and $U_{tr,exp}$ the U in the empty and vegetated canyon, respectively –,

(ii) cell-weighted spatial average of the resampled $\overline{u}$ measurements adding the missing data close to the canyon boundaries by extrapolation with logarithmic law ($U_{\parallel,log}$ and $U_{tr,log}$),

(iii) cell-weighted spatial average of the resampled $\overline{u}$ measurements adding the missing data close to the canyon boundaries by extrapolation with linear law (U_{lin} and $U_{tr,lin}$).

To apply methods (ii) and (iii) the no-slip condition is considered at the walls.

The results obtained with methods (i), (ii), and (iii), normalized by the component of the free-stream velocity projected along the longitudinal axis of the canyon ($U_{\parallel} = U_{\infty}\cos(\theta)$), are reported in Fig. 5.5b. Regardless of the presence of trees, the three averaging methods exhibits the same behaviour of U, normalized by $U_{\parallel}$, with the wind angle θ. Nevertheless, methods (ii) and (iii) provide lower values with respect to method (i), since low velocity values at the canyon boundaries are added to the experimental data. Without trees, the discrepancy between method (i) and (ii) is around 13% and it slightly increases to 20% comparing method (i) and (iii). A slightly larger difference (of around 10%) was found between methods (ii) and (iii), compare to the non-vegetated case. The discrepancy between the three methods is significantly less than the difference in U between non-vegetated and vegetated canyons (found equal to about -75% with the three methods), confirming that all methods are valid to detect the effects of wind direction and vegetation on U.

Looking at the trend of $U_{\parallel,log}/U_{\parallel}$ with θ, we found that, in the empty canyon, $U_{\parallel,log}/U_{\parallel}$ decreases by 15% from θ=0° to θ=30° and it increases by 5% from θ=30° to θ=60° (see the red continuous curve in Fig. 5.5b). These differences suggest that $U_{\parallel,log}/U_{\parallel}$ does not show a well defined trend with θ, thus for any wind direction the longitudinal advective flux along the canyon scales with the street-axis parallel component of the external wind. In the presence of trees (red dashed curve in Fig. 5.5b), $U_{tr,log}/U_{\parallel}$ monotonically decreases with the increase of the wind angle. However, the decreasing rate is not constant: there is 27% difference between θ=0° to θ=30° and 12% between θ=30° to θ=60°. By comparing the values of U found in the empty and vegetated canyons, we found that the trees induce 75% decrease in $U_{tr,log}/U_{\parallel}$ with wind directions θ=0° and θ=30° and this difference increases to 82% with θ=60°.

Finally, we compare the experimental U with the predictions provided by the analytical solution proposed by Soulhac et al. (2008). They provided an analytical equation for the spatial average of the mean longitudinal velocity in the cross-section of a street canyon (U_{an}), for any wind direction. This solution was obtained from a momentum balance between the turbulent entrainment at the canyon rooftop and the tangential stresses on the canyon walls, neglecting longitudinal pressure gradients and transverse components of the flow. Soulhac et al. (2008) demonstrated that U_{an} is proportional to the cosine of the wind angle. Under these assumptions, the analytical expression (4.7) becomes

$$U_{an,\theta} = \cos(\theta) U_{an} \tag{5.1}$$

They validated this model by comparison with results of numerical simulations performed using the Reynolds-Averaged Navier–Stokes model MERCURE, adopting a k-ε closure model. Here, we provide a comparison between the analytical model and the U evaluated from the experimental data collected in the empty canyon.

The unknown parameters C and z_i in Eq. 4.7 were estimated from the best-fit between the analytical equations for vertical and horizontal profiles of $\overline{u}$ in the canyon and the experimental horizontal and vertical profiles of $\overline{u}$, measured in the empty canyon with wind direction θ=0° (further details about this procedure are reported in Sect. 4.4). In the wind-aligned street canyon, we obtained $U_{an,\theta}$ equal to 2.32 ms^{-1} and we report this solution with a black

dashed line in Fig. 5.5b. Comparing this result with the U_{exp} calculated with θ=0°, we found a small difference equal to 4%, whilst, with the same θ, the differences between the analytical solution and $U_{\parallel,log}$ and U_{lin} are equal to 9% and 17%, respectively. Although method (i) provides the lowest discrepancy between the analytical and experimental U, the value of U_{exp} overestimates the averaged mean longitudinal velocity in the cross-section of the canyon, since small velocity values close to the canyon boundaries are not considered. A more precise estimate of U can be reached applying methods (ii) and (iii) and among them the best agreement between the analytical model and the experimental U was obtained with method (ii). One of the possible explanation for the discrepancy between $U_{\parallel,log}$ and $U_{an,\theta}$ is the presence of slight pressure gradients along the wind tunnel (see Sect. 4.4). The effects of the pressure gradients, projected along the longitudinal axis of the canyon, could be the reason for the enhancement of this discrepancy to 22% and 17%, with θ=30° and θ=60°, respectively. Moreover, also uncertainties in the extrapolation method of the missing experimental data could be responsible for the disagreement between the model and the experimental $U_{\parallel,log}$.

5.3 Velocity field in a street canyon with intersections for different wind directions

To analyse the influence of street intersections, we investigated flow velocity statistics on cross-sections 1, 2, and 3 (indicated in panels 5.1e and 5.1g), along the x-axis of the canyon. We performed the analysis in the empty and vegetated canyons, with three different wind directions. For sake of brevity, in Figs. 5.6-5.8, we display the results on cross-sections 1 and 3, being the cross-section 2 a transition between the two behaviours.

5.3.1 Cross-sectional velocity field in the street canyon

Street axis-parallel wind direction

The turbulent flow within a street canyon with intersections is governed by the entrainment of the overlying flow at the rooftop and the lateral entrainment

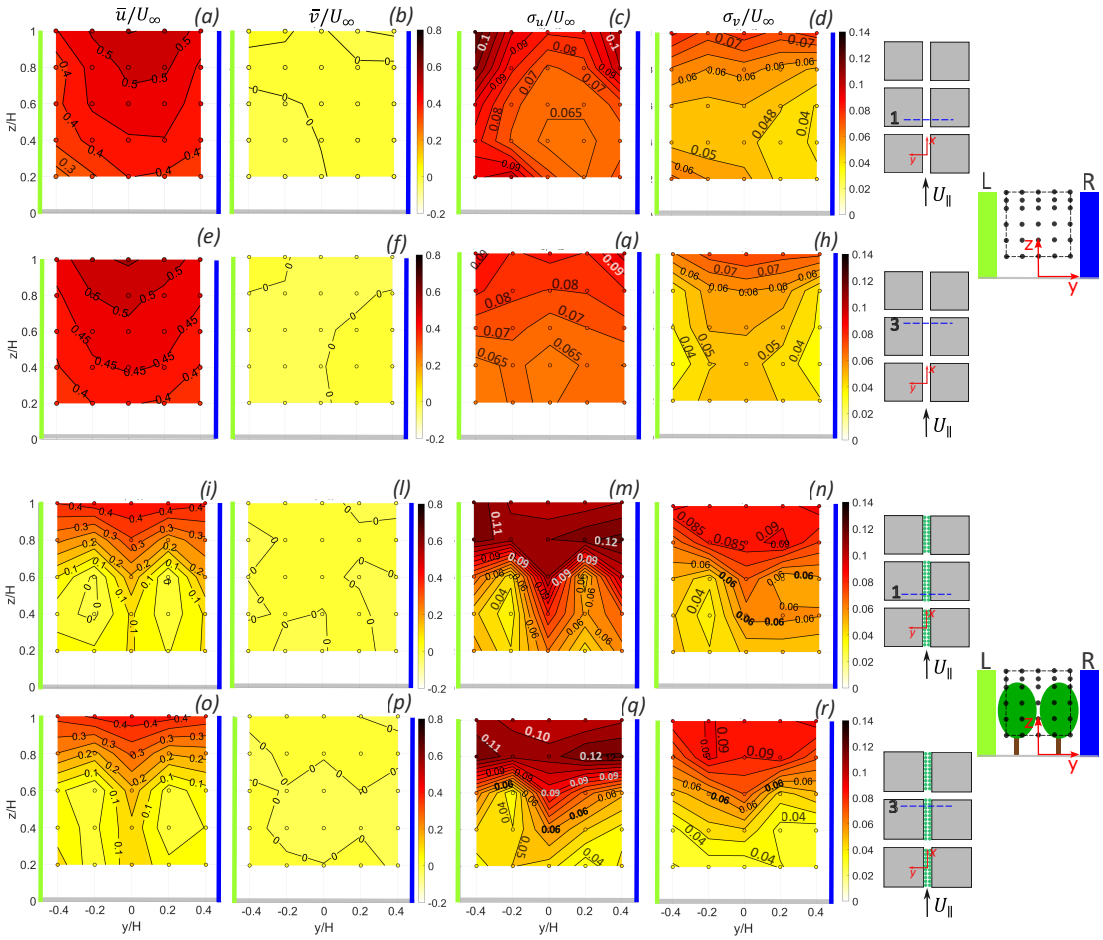


Figure 5.6 Transversal behaviour of the mean longitudinal velocity, mean transversal velocity, longitudinal velocity standard deviation, and transversal velocity standard deviation within the empty canyon, close to the upwind intersection (a-d) and close to the downwind intersection (e-h), with wind direction θ=0°. (i-r) Transversal behaviour of flow velocity statistics within the vegetated canyon, close to the upwind intersection (i-n) and close to the downwind intersection (o-r). The sketches to the right indicate the position of the measuring cross-section with respect to the intersection (planar view) and the canyon left and right walls (front view).

of air from the transversal streets at the canyon edges (Soulhac et al., 2009; Li et al., 2021). The lateral flows modify the longitudinal homogeneity of flow velocity statistics along the canyon. However, when the external wind is parallel to the longitudinal axis of the canyon, intersections have limited effects on the mean flow along the canyon. Indeed, close to the upwind intersection (see cross-section 1 in Fig. 5.6a), $\overline{u}/U_\infty$ exhibits a spatial behaviour similar to that in the canyon without intersections (Fig. 5.2a): notably, it reaches its maximum values at the rooftop and monotonically decreases moving towards the lateral edges and the bottom of the cross-section. A slight asymmetry of $\overline{u}/U_\infty$ arises at the bottom of the canyon, where values equal to 0.3 in the lower left-hand corner and to 0.4 in the lower right-hand corner are detectable, probably due to the sensitivity of the flow to small misalignment of the blocks. The $\overline{v}/U_\infty$ is zero in the whole cross-section (see Fig. 5.6b), indicating the absence of transversal flows within the canyon. The influence of street intersections can be detected looking at velocity turbulent fluctuations, as we note that they show quite different patterns and higher intensity with respect to what found in the empty canyon without intersections (Figs. 5.2c-d). The σ_u/U_∞ (Fig. 5.6c) is 0.1 in the upper corners of cross-section 1 and 0.09 along the left wall, which implies an intensity 20% and 30% higher than that observed in the corners and at the laterally-closed canyon wall respectively. In the region below the shear layer, the σ_v/U_∞ (panel 5.6d) becomes slightly asymmetrical with respect to the vertical axis, showing values equal to 0.05 along the left wall, and to 0.06 in the lower left corner, thus around 25% higher than at the right wall. Close to the downwind intersection (cross-section 3 in panels 5.6e-h), the mean and turbulent flow fields recover a symmetric spatial pattern and the same intensity found in the canyon without intersections (Fig. 5.2a-d). This reveals that, with wind direction θ=0°, the effects of the upwind intersection are attenuated at a distance $4H$ from the entrance of the canyon and the second downwind intersection does not significantly affect the canyon flow.

The presence of trees within the wind-aligned street canyon homogenizes the mean flow along the x-axis. Indeed, in cross-sections 1 and 3 (Figs. 5.6i and 5.6o), the $\overline{u}/U_\infty$ is zero between the trees and it increases to 0.4 at the canyon rooftop (as observed in the canyon without intersections Fig. 5.2e). Conversely, between trees, the spatial pattern of longitudinal and transversal velocity fluctuations is slightly different in cross-sections 1 and 3, while it is

homogenized above the tree crowns. Close to the upwind intersection, the σ_u/U_∞ and σ_v/U_∞ (see cross-section 1 in Figs. 5.6m-n) show asymmetric intensity in correspondence of trees: they are around 0.04 in correspondence of the left tree (y/H=(-0.4,0] and z/H=[0.2,0.6]) and 0.06 in correspondence of the right tree (y/H=[0,0.4] and z/H=[0.2,0.6]). This asymmetry is attenuated in cross-section 3 (Fig. 5.6q-r), where we see values of σ_u/U_∞ and σ_v/U_∞ equal to 0.03 in correspondence of both trees (at z/H=[0.2,0.6]), similar to what observed in the canyon without intersections (Fig. 5.2g-h). At the rooftop, the interaction between the tree crowns and the external flow leads to a sharp increase in σ_u/U_∞ to 0.1 and in σ_v/U_∞ to 0.09.

Oblique wind direction

With oblique wind direction, the flow within the intersection splits between the main canyon and the transversal streets. The flow bifurcation generates flow separation at the corners of the intersection and the formation of vertical-axis recirculating flow structures at the two ends of the main canyon (Carpentieri et al., 2009; Soulhac et al., 2009; Balogun et al., 2010). These complex local flow structures are responsible for a strongly three-dimensional spatial pattern of the mean and turbulent flow fields along the laterally-opened canyon. With θ=30°, the spatial homogeneity of $\overline{u}/U_\infty$, observed on the cross-section of the laterally-closed canyon (Fig. 5.3a), is altered by the incoming flow from the upwind intersection. Indeed, on cross-section 1 (Fig. 5.7a), $\overline{u}/U_\infty$ is equal to 0.1 along the upwind wall of the canyon, and it increases to 0.2 along the transversal profile at z/H=0.2 and to 0.3 in the remaining portion of the cross-section. The low $\overline{u}/U_\infty$ along the canyon upwind wall is caused by the flow separation at the upwind corner of the intersection, due to the incoming flow from the transversal street. The $\overline{v}/U_\infty$ (Fig. 5.7b) depicts a transversal flow towards the downwind wall at the rooftop, with asymmetric velocity values: $\overline{v}/U_\infty$ is equal to -0.1 at y/H=[-0.4,0] and to -0.2 in the upper upwind corner. At ground level, we do not detect a positive transversal flow towards the upwind wall, suggesting that the recirculation is not established. However, there is a weak negative flow equal to -0.06, probably induced by the entrainment of flow from the transversal streets. As observed in the wind-aligned canyon with intersections, turbulent fluctuations are higher than in the configuration without intersections

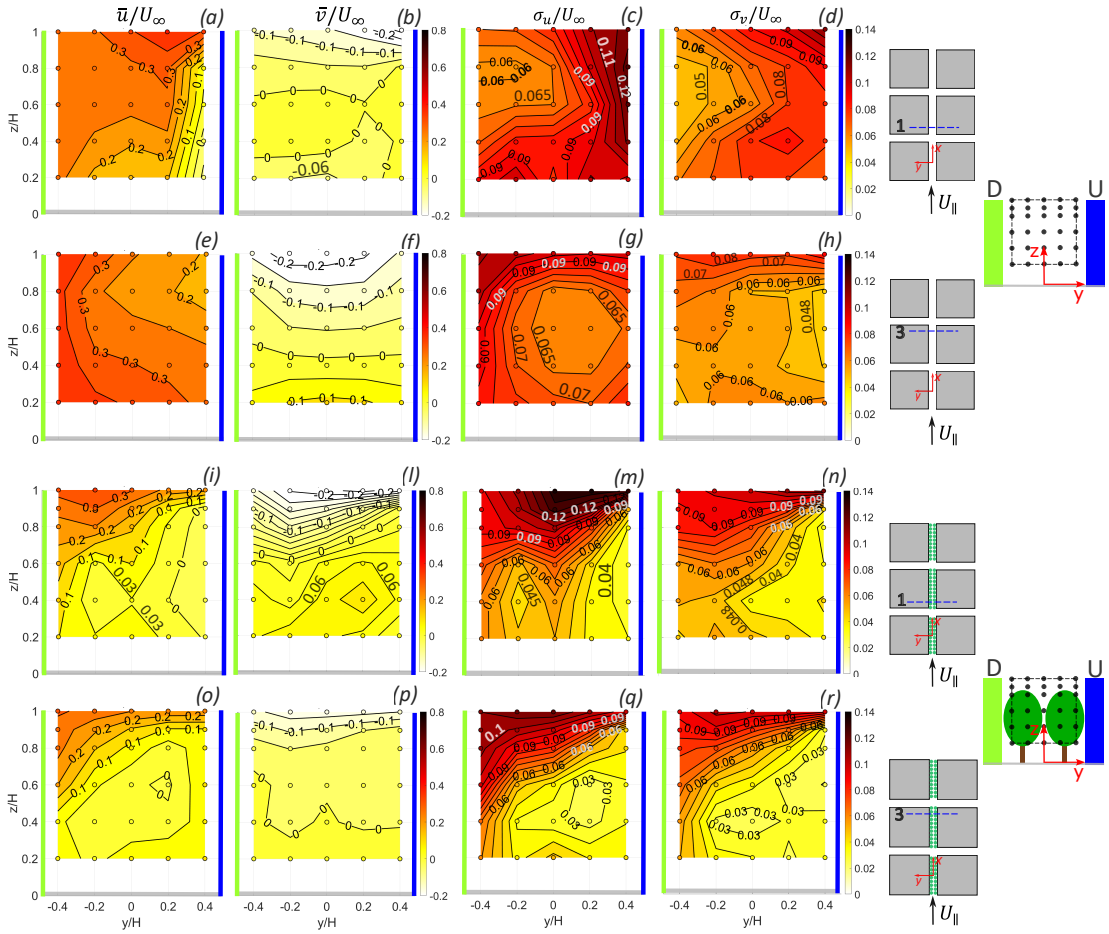


Figure 5.7 Transversal behaviour of the mean longitudinal velocity, mean transversal velocity, longitudinal velocity standard deviation, and transversal velocity standard deviation within the empty canyon, close to the upwind intersection (a-d) and close to the downwind intersection (e-h), with wind direction θ=30°. (i-r) Transversal behaviour of flow velocity statistics within the vegetated canyon, close to the upwind intersection (i-n) and close to the downwind intersection (o-r). The sketches to the right indicate the position of the measuring cross-section with respect to the intersection (planar view) and the canyon downwind and upwind walls (front view).

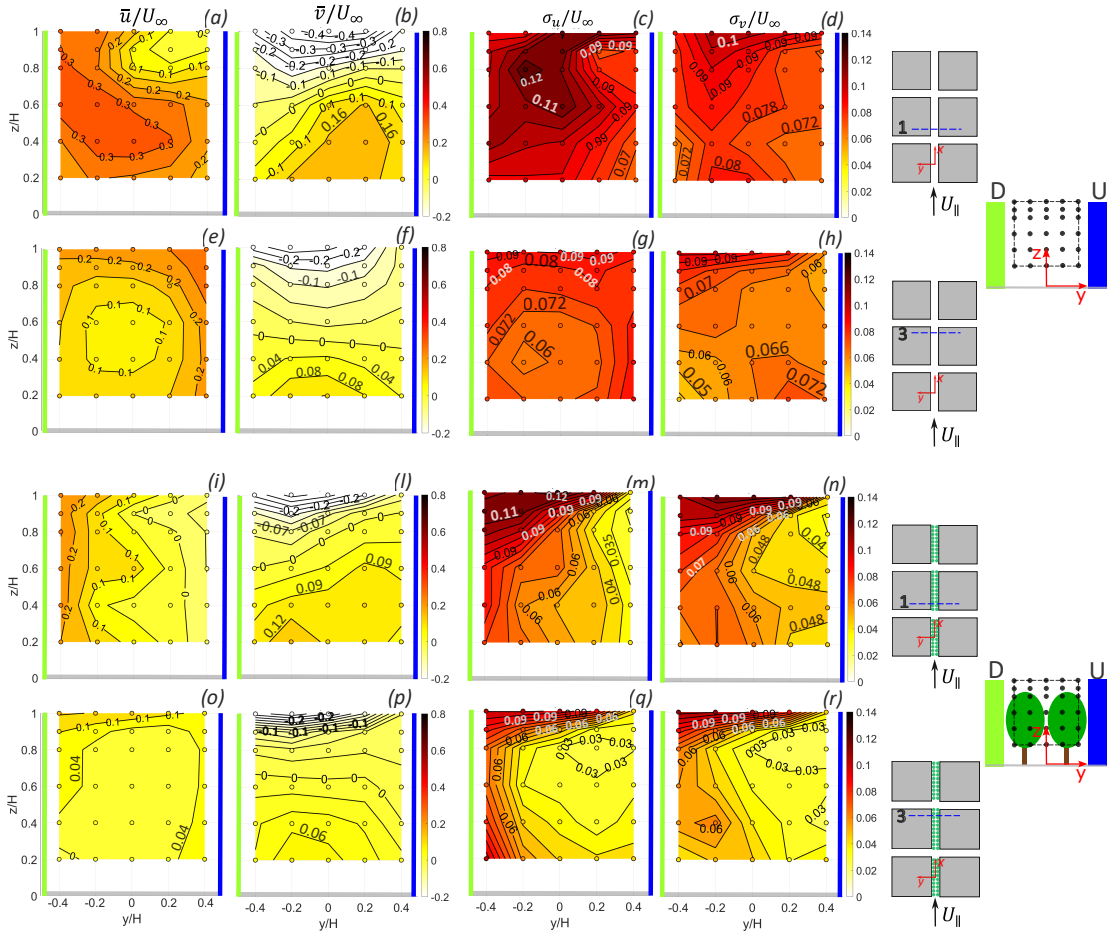


Figure 5.8 Transversal behaviour of the mean longitudinal velocity, mean transversal velocity, longitudinal velocity standard deviation, and transversal velocity standard deviation within the empty canyon, close to the upwind intersection (a-d) and close to the downwind intersection (e-h), with wind direction θ=60°. (i-r) Transversal behaviour of flow velocity statistics within the vegetated canyon, close to the upwind intersection (i-n) and close to the downwind intersection (o-r). The sketches to the right indicate the position of the measuring cross-section with respect to the intersection (planar view) and the canyon downwind and upwind walls (front view).

(shown in Fig. 5.3c,d) and show a different spatial pattern. In particular, the generation of turbulence in the wakes of the upwind building leads to high σ_u/U_∞ and σ_v/U_∞ intensities close to the upwind wall of the canyon, from where they monotonically decrease by about 50% moving transversely toward the downwind wall (panels 5.7c,d). Close to the downwind intersection, we found mean and turbulent flow fields different from those observed close to the upwind intersection. The $\overline{u}/U_\infty$ (cross-section 3 in panel 5.7e) monotonically increases from 0.2 to 0.4, moving transversally from the upwind to the downwind wall. The transversal recirculation is re-established, as we see two opposite flows at the top and at the bottom of the canyon, with velocity $\overline{v}/U_\infty$ equal to -0.2 and +0.1, respectively (see panel 5.7f). The behaviour of σ_u/U_∞ (Fig. 5.7g) is similar to that found within the canyon without intersections (Fig. 5.3g), with high intensity at the rooftop and along the downwind wall and reduced intensity in the centre of the canyon. However, in both areas the values are 30% higher than in the previous street geometry. The σ_v/U_∞ (Fig. 5.7h) shows a homogeneous intensity around 0.08 at the rooftop and it decreases to 0.06 within the canyon and to 0.05 along the upwind wall, denoting 30% higher intensity compared to the inner canyon without intersections (Fig. 5.3d).

The longitudinal heterogeneity of the mean and turbulent flow fields along the laterally-opened canyon is attenuated in the presence of trees, since these trees limit the entrance of air from the street intersections, as well as the formation of recirculating structures at the canyon ends. On cross-sections 1 and 3, the $\overline{u}/U_\infty$ (see panels 5.7i and 5.7o) shows an asymmetrical spatial pattern similar to that in the vegetated canyon without intersections (Fig. 5.3e), with high mean longitudinal velocity at the canyon rooftop and along the downwind wall and almost zero mean longitudinal velocity in the remaining part of the cross-section. The spatial pattern of $\overline{v}/U_\infty$ is slightly different in cross-sections 1 and 3. Notably, close to the upwind intersection, the mean transversal velocity is equal to -0.2 above the tree crowns and +0.06 in correspondence of tree trunks (Fig. 5.7l). The non-zero $\overline{v}/U_\infty$ at the bottom of the cross-section suggests the possible entrainment of flow from the cross-wind street at ground level, but it is too weak to demonstrate the presence of a transversal recirculation. This positive flow is no more detectable in cross-section 3 (Fig. 5.7p). Small heterogeneity along the x-axis are also evident looking at the spatial behaviour and intensity of the longitudinal and transversal velocity

standard deviation. Close to the upwind intersection, σ_u/U_∞ (Fig. 5.7m) and σ_v/U_∞ (Fig. 5.7n) show asymmetric intensity between the trees, notably they are 20% higher in correspondence of the downwind tree than of the upwind tree. In cross-section 3 (Figs. 5.7q and 5.7r), σ_u/U_∞ and σ_v/U_∞ recover the same spatial pattern observed in the laterally-closed canyon (i.e., two layers of high fluctuation intensity at the rooftop and along the downwind wall and low fluctuation intensity between the trees), demonstrating that the influence of street intersections is attenuated.

Finally, we analyse the influence of the intersections on the mean and turbulent flow fields within the canyon, with wind direction θ=60°. On cross-section 1, we see almost zero $\overline{u}/U_\infty$ in the upper upwind corner of the canyon (see Fig. 5.8a), revealing flow detachment in this area. Outside this low velocity area, the $\overline{u}/U_\infty$ increases to 0.2 along the upwind wall and close to the ground (at z/H=0.2) and to 0.3 in the centre of the canyon and along the downwind wall, at z/H=[0.6,1]. The spatial pattern of $\overline{v}/U_\infty$ (shown in panel 5.8b) depicts a transversal recirculation, with negative mean velocity equal to -0.4 at the rooftop and positive velocity equal to +0.2 at ground level and to +0.1 in the centre of the canyon. However, the heterogeneity of $\overline{u}/U_\infty$ and the difference of about 50% in the modulus of $\overline{v}/U_\infty$ from the top to the bottom of the cross-section do not guarantee a persistent helicoidal structure close to the upwind intersection. Concerning turbulent fluctuations, we found that σ_u/U_∞ (Fig. 5.8c) shows values equal to 0.09 along the upwind wall and higher values equal to 0.12 in the downwind half of the canyon (i.e., y/H=[-0.4,0] and z/H=[0.2,1]). Both intensities are around 40% higher than those observed in the same zones in the empty canyon without intersections (Fig. 5.4c), due to the interaction between the flow in the main canyon and the incoming flow from the cross-wind streets. The σ_v/U_∞ (Fig. 5.8d) also shows a different spatial pattern from that observed in the canyon without intersections (Fig. 5.4d), with 40% higher values in the centre of the cross-section and close to the upwind wall, while lower differences, around 30%, are visible along the downwind wall. Close to the downwind intersection, the $\overline{u}/U_\infty$ (Fig. 5.8e) shows two layers of thickness $0.2H$ at the rooftop and along the upwind wall of velocity equal to 0.2 and an area of mean longitudinal velocity equal to 0.1 in the centre of the canyon. The deceleration of the flow in the centre of the canyon highlights a possible deviation of the flow into the transversal

canyons. The $\overline{v}/U_\infty$ (Fig. 5.8f) shows a difference of 60% in the modulus of the velocity at the top and at the bottom of the cross-section, which hardly suggests the presence of a recirculating structure. The σ_u/U_∞ (Fig. 5.8g) exhibits a core with values equal to 0.07 within the canyon and it increases to 0.08 along the upwind wall and it reaches 0.09 at the rooftop. Therefore, inside the canyon, σ_u/U_∞ reaches an intensity 40% higher than in the canyon without intersections (Fig. 5.4c). The σ_v/U_∞ (Fig. 5.8h) exhibits highly asymmetric intensities in the corners of the cross-section: notably, σ_v/U_∞ decreases by 33% moving from the upper downwind corner to the upwind one, while in the lower corners it increases by 17% moving transversely in the same direction. It is interesting to notice that, at the rooftop, σ_v/U_∞ is equal to 0.09, as observed at the rooftop of cross-section 3 with θ=30° (Fig. 5.7h), demonstrating that close to the downwind intersection the turbulent exchange between the canyon and the external flow scales with U_∞. Similar conclusions can be achieved from the comparison of σ_u/U_∞ at the rooftop of cross-section 3 between θ=60° and θ=30° (Fig. 5.7g).

With wind direction θ=60°, the presence of trees does not homogenise the mean and turbulent flow fields along the x-axis. Close to the upwind intersection, $\overline{u}/U_\infty$ (Fig. 5.8i) is almost zero along the upwind wall and it monotonically increases to 0.2 moving towards the downwind wall, denoting a mean longitudinal flow with double velocity with respect to that observed at the downwind wall of the canyon without intersections (Fig. 5.4e). The non-zero $\overline{u}/U_\infty$ along the downwind wall suggests flow canalisation between the tree crowns and the wall. The transversal circulation is not dampened by the trees, as we see a negative $\overline{v}/U_\infty$ equal to -0.25 above the tree crowns and an opposite flow equal to around +0.1 between tree trunks (at z/H=0.2) and to +0.06 close to the centre of the canyon (Fig. 5.8l). Turbulent fluctuations (Fig. 5.8m and 5.8n) show a pattern very similar to that in the vegetated canyon with wind direction θ=30° (Fig. 5.7m and 5.7n), namely, high intensity at the rooftop and around the downwind tree and 50% lower intensity in correspondence of the upwind tree. The effects of the street intersections are less marked close to the downwind intersection (as observed with θ=30°) and the spatial patterns of the mean and turbulent flow fields are similar to those in the vegetated canyon without intersections. Concerning the mean flow, we see almost zero $\overline{u}/U_\infty$ in cross-section 3 (Fig. 5.8o), while $\overline{v}/U_\infty$ (Fig. 5.8p) is equal to -0.2 above

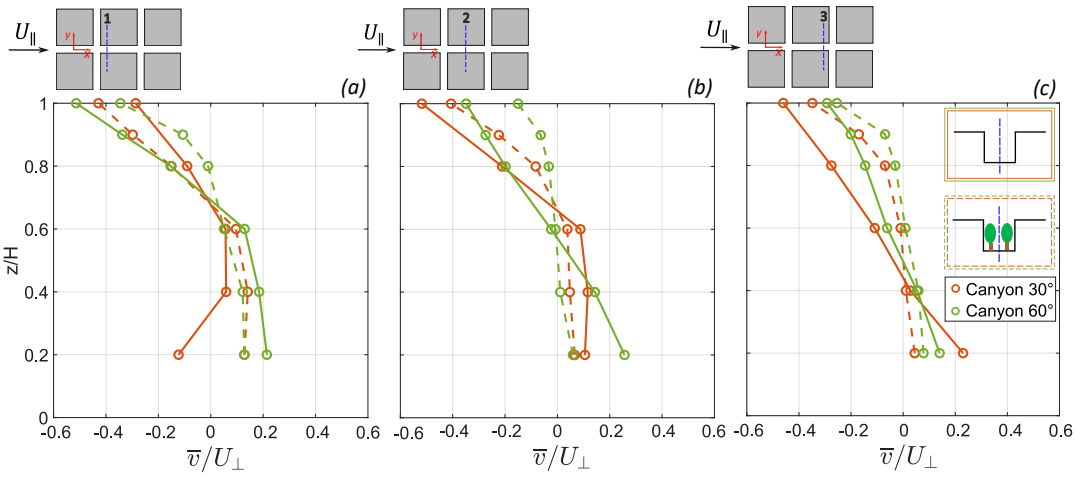


Figure 5.9 vertical profiles of the mean transversal velocity measured in the centre (y/H=0) of the laterally-opened canyon, close to the upwind intersection (a), in the centre (b), and close to the downwind intersection (c). Continuous and dashed lines refer to the empty and vegetated canyon configurations, respectively. The different colors indicate to wind directions θ=30°(orange) and θ=60° (green).

the tree crowns and to +0.06 at ground level. The difference of 60% in $\overline{v}/U_\infty$ between the top and the bottom of the cross-section reveal the absence of a well-defined transversal recirculation. The σ_u/U_∞ (Fig. 5.8q) exhibits similar pattern to the vegetated canyon without intersections (Fig. 5.4g), i.e., it is equal to 0.09 at the rooftop and to 0.08 along the downwind wall, and it sharply decreases to 0.03 within the canyon. A similar spatial pattern characterises σ_v/U_∞ (Fig. 5.8r), but in the downwind part of the cross-section (i.e., y/H=[-0.4,0] and z/H=[0.2,0.6]) the intensity of σ_v/U_∞ is two times the intensity in correspondence of the upwind tree (y/H=[-0.4,0] and z/H=[0.2,0.8]).

5.3.2 Transversal velocity profiles

To investigate the evolution of the mean transversal velocity along the vertical axis of the canyon with intersections, in Fig. 5.9, we report vertical profiles of $\overline{v}/U_\perp$ measured in the centreline of the cross-sections located close to the upwind intersection (cross-section 1), in the canyon centre (cross-section 2), and close to the downwind intersection (cross-section 3), with wind directions θ={30°,60°}.

In the non-vegetated canyon (Fig. 5.9a-c), the profiles of the mean transversal velocity measured in the three cross-sections do not scale with the component of the external wind perpendicular to the canyon axis. This occurs due to the formation of vertical-axis recirculating structures at the canyon edges, whose size and orientation depend on the wind direction (Garbero et al., 2010; Soulhac et al., 2013). Close to the upwind intersection (see panel 5.9a), the profiles depict a transversal mean flow from the upwind wall to the downwind wall at the rooftop, with an increase in mean velocity of 40% from θ=30° to θ=60°. The bottom part of the profile measured in the 30° rotated canyon shows a negative transversal velocity equal to -0.1, reasonably induced by the incoming flow from the cross-wind streets. With θ=60°, $\overline{v}/U_{\perp}$ is equal to +0.2 close to the ground, thus 60% lower in modulus with respect to the rooftop, revealing an irregular transversal recirculation. Also in the centre of the canyon the profiles shows different shapes with the two wind directions (panel 5.9b). At the rooftop, $\overline{v}/U_{\perp}$ is equal to -0.5 with θ=30° and decreases to -0.35 with θ=60°. Close to the ground the profiles show a positive transversal flow, as expected in the presence of a recirculating structure, whose velocity doubles with the increase of the wind angle θ. Finally, close to the downwind intersection (panel 5.9c), the profiles show a quite regular shape in the empty canyon, regardless of the wind direction, with two opposite flow at the top and the bottom of the canyon, whose velocity decreases with the increase of the angle θ. This behaviour is typical of a transversal recirculation governed by the external flow and not significantly affected by lateral incoming flows. However, the influence of the vertical-axis recirculating structures at the edges of the canyon is evident from the lack of overlap between the $\overline{v}/U_{\perp}$ profiles as θ varies.

Although trees dampen the vertical-axis recirculation at the canyon edges, the vertical profiles of $\overline{v}/U_{\perp}$ do not overlap with wind directions θ=30° and θ=60°. This is evident particularly above the tree crowns, due to the effects of the shape and spatial arrangement of trees on the transversal mean flow that are sensitive to the wind direction (as already pointed out analysing vertical profiles of $\overline{v}/U_{\perp}$ in the canyon without intersections). The effect of the wind direction on the interaction between trees and transversal flow are smoothen inside the canyon (at z/H=[0.2,0.8]), where $\overline{v}/U_{\perp}$ profiles overlap to a constant value along the z-axis, both close to the intersections and in the centre. Looking at the $\overline{v}/U_{\perp}$ profiles close to the upwind intersection (dashed lines in panel

5.9a), we observe that the transversal flow towards the downwind wall at the rooftop shows higher velocity with θ=30° than with θ=60°, while between trees (at z/H=[0.2,0.6]) the profiles collapse around +0.1. The positive flow within the canyon suggests the presence of the transversal recirculation, favoured by lateral entrainment of flow. In the centre of the canyon (panel 5.9b), $\overline{v}/U_{\perp}$ with θ=30° is 50% higher than with θ=60°, while inside the canyon all the profiles overlap at a value close to zero within the canyon, demonstrating that the transversal flow towards the upwind wall is dampened. Similar pattern with θ is observed close to the downwind intersection (panel 5.9c), but with lower discrepancy in $\overline{v}/U_{\perp}$ with θ=30° and θ=60° at the canyon rooftop.

5.3.3 Cross section-averaged mean longitudinal velocity

After having investigated the influence of street intersections and wind direction on the spatial pattern of flow velocity statistics along the canyon, we are interested in analysing how much the spatial average of the mean longitudinal velocity U in cross-sections 1, 2, and 3, varies. Also in the laterally-opened canyon, the spatial average of the mean longitudinal velocity in cross-sections 1, 2, and 3, evaluated with the averaging methods (i), (ii), and (iii) – defined in Sect 5.2.3 – shows similar trends with the wind direction. Moreover, the differences among the U values obtained with the different averaging methods are smaller than 20%, as we found in the laterally-closed canyon. Thus in this section we refer to the U calculated with method (ii). In particular, $U_{\parallel,log}$ and $U_{tr,log}$ were calculated averaging the $\overline{u}$ measurements collected along the empty and vegetated canyons, close to the upwind intersection (in cross-section 1), in the canyon centre (in cross-section 2), and close to the downwind intersection (in cross-section 3). We repeated the analysis with wind directions θ={0°, 30°, 60°}. Moreover, we investigate the variation of $U_{\parallel,log}$ and $U_{tr,log}$, calculated in the canyon centre, with the cosine of θ.

Without trees and under the wind direction θ=0° (blue continuous line in Fig. 5.10a), the $U_{\parallel,log}$ is almost constant along the x-axis. The value of $U_{\parallel,log}$ close to the upwind intersection, slightly lower than those calculated in cross-sections 2 and 3, reflects the low $\overline{u}$ values in the lower left-hand corner of cross-section 1 (see Fig. 5.6a). With θ=30° and θ=60° (orange and green curves in Fig. 5.10a), the variation of $U_{\parallel,log}$ along the canyon is more visible. Indeed, with θ=30°,

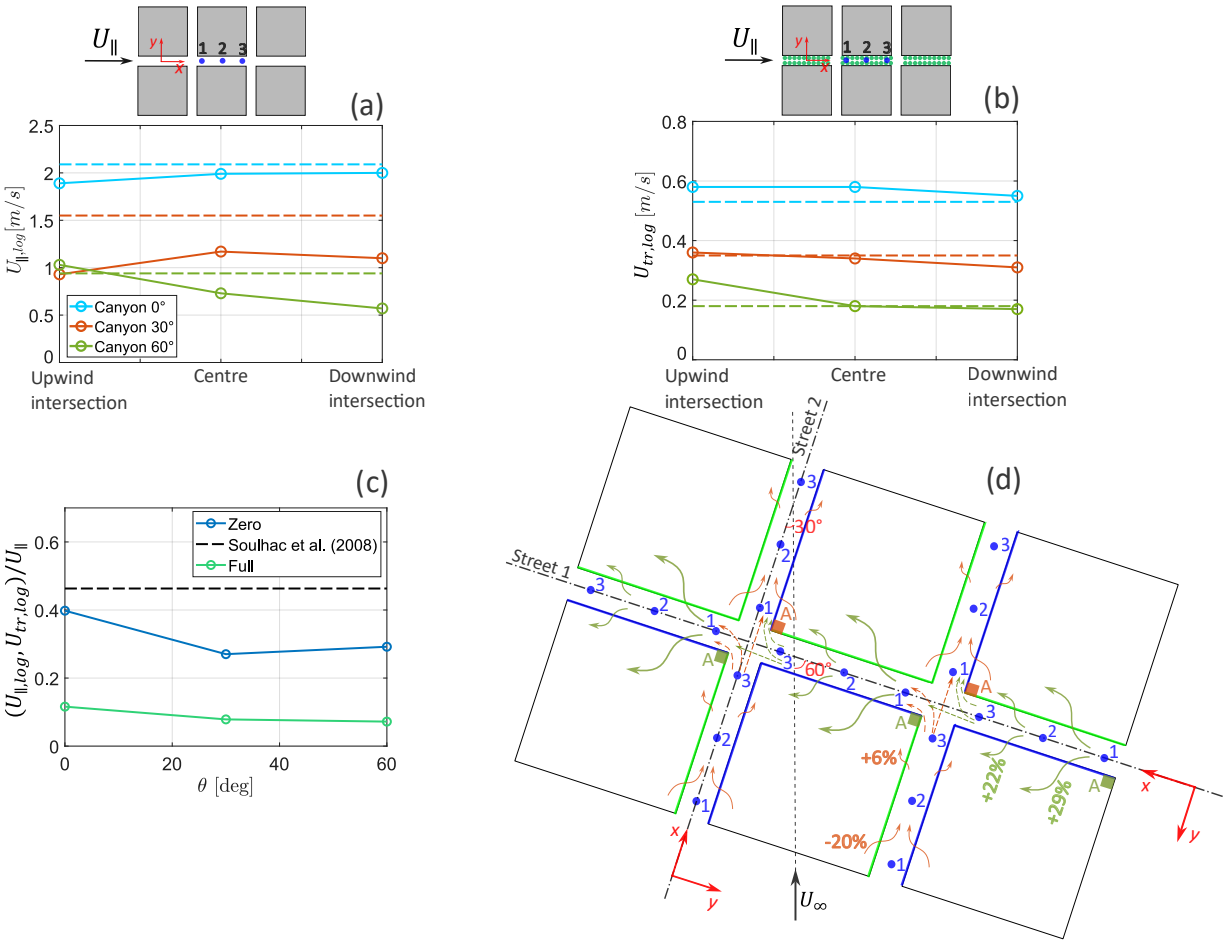


Figure 5.10 variation of the spatial average of the mean longitudinal velocity (indicated as $U_{\parallel,log}$ in the non-vegetated case and $U_{tr,log}$ in the vegetated case) in the cross-sections close to the upwind intersection (cross-section 1), in the canyon centre (cross-section 2), and close to the downwind intersection (cross-section 3), in the Zero (a) and Full (b) configurations. The different colors refer to wind directions of θ=0° (blue), θ=30°(orange), and θ=60° (green) with respect to the canyon axis. The dashed lines represent the spatial average of the mean longitudinal velocity in the cross-section of the canyon without intersections. (c) Variation of the spatial average of the mean longitudinal velocity in cross-section 2 with the wind direction, for the Zero ($U_{\parallel,log}$) and Full ($U_{tr,log}$) configurations. The black dashed line indicates the analytical model of Soulhac et al. (2008). (d) Sketch of the three dimensional flow structure within a street network. The blue circles represent the positions of the measuring cross-sections 1, 2, and 3 along the street segments. Orange and green arrows indicate inward or outward flows in the 30° and 60° rotated canyons, respectively. The sizes of the arrows are proportional to the relative difference among $U_{\parallel,log}$ values, calculated on the three cross-sections along the x-axis. The green and blue lines indicate the downwind and upwind walls of the canyon, respectively.

$U_{\parallel,log}$ close to the upwind intersection is 20% lower than in the canyon centre and close to the downwind intersection. On the contrary, with θ=60°, $U_{\parallel,log}$ shows a decreasing behaviour along the canyon with differences of 30% between the upwind intersection and the centre and of 20% between the centre and the downwind intersection. If we estimate as $U_{\parallel,log}HW$ the flow rate across the canyon cross-section, the increase of $U_{\parallel,log}$ along the 30° rotated canyon entails the entrainment of air from the external flow into the canyon. Vice versa, within the 60° rotated canyon, a mean vertical flux towards the external boundary layer is the result of the along-canyon decrease in $U_{\parallel,log}$. Comparing the values of $U_{\parallel,log}$ between the canyons with and without intersections (the later represented with dashed lines in Fig. 5.10a), we observe that $U_{\parallel,log}$ in the laterally-opened canyon is lower than that in the canyon without intersections, with the greatest discrepancies (around 40%) close to the upwind intersection with θ=30° and close to the downwind intersection with θ=60°. This result is in line with that obtained by Soulhac et al. (2009) with numerical simulations, which links the decrease in U in the canyon with intersections compared to the one without, with the presence of recirculation structures at the canyon edges, which hinder longitudinal mean flow.

In the presence of trees, $U_{tr,log}$ is quite homogeneous along the canyon, with all the wind directions (see Fig. 5.10b), since the trees hinder the formation of recirculating structures at the edges of the canyon. Thus, the $U_{tr,log}$ is similar to that calculated in the canyon without intersections, with all wind directions. However, with θ=60°, we notice that $U_{tr,log}$ close to the upwind intersection is 40% higher than in the centre of the canyon, and 33% higher than in the canyon without intersections. This results from the high $\overline{u}$ found at the downwind side of cross-section 1 (visible in Fig. 5.8i), induced by a flow canalisation along the downwind wall of the canyon.

Finally, in Fig. 5.10c, we report the variation of $U_{\parallel,log}/U_{\parallel}$ and $U_{tr,log}/U_{\parallel}$ with the wind angle. The $U_{\parallel,log}$ and $U_{tr,log}$ refer to the $\overline{u}$ data collected in cross-section 2 in the centre of the canyon. Without trees (blue curve), $U_{\parallel,log}/U_{\parallel}$ is independent from the wind angle, as observed in the canyon without intersections (red continuous curve in Fig. 5.5b), but larger difference between θ=0° and θ=30° are evident in the laterally-opened canyon with respect to the laterally-closed one, as well as a larger deviation from the analytical $U_{an,\theta}$. The $U_{\parallel,log}/U_{\parallel}$ decreases by 30% from wind direction θ=0° to θ=30°, a difference

twice as that in the configuration without intersections. The differences between $U_{\parallel,log}/U_{\parallel}$ and $U_{an,\theta}$ are of 14% with θ=0° and 40% with θ=30° and with θ=60°, almost twice that in the canyon without intersections. This large discrepancy from the analytical model confirms the reduction of U in the laterally-opened canyon with respect to the laterally-closed one, due to lateral air entrainment. This phenomenon prevents the application of Eq. 4.7 to evaluate the spatial average of the mean longitudinal velocity within a canyon with intersections (Soulhac et al., 2009, 2013).

The significant variation of U with the wind angle θ is not attenuated by the trees: $U_{tr,log}/U_{\parallel}$ decreases by 40% from θ=0° to θ=30° and by 47% from θ=30° to θ=60°. Comparing $U_{tr,log}/U_{\parallel}$ with $U_{\parallel,log}/U_{\parallel}$ we found that the presence of trees reduces by 70% the transversally-averaged mean longitudinal velocity, with all the wind directions, similar to what found in the canyon without intersections.

5.3.4 Discussion about the flow field within a street network without vegetation

The results for the flow fields within a street canyon with intersections, oriented at θ=30° and θ=60° with respect to the wind, can be combined to reconstruct the flow topology within and above a street network. Figure 5.10d shows a schematic of a street network, featuring a street inclined at 60° to the external wind ("street 1") and two transverse streets inclined at 30° (with θ=30° and θ=60° being complementary angles). The longitudinal behaviour of the flow rate across the canyon cross-section (discussed in Sect. 5.3.3) shows an increasing trend along the 30° rotated canyon and a decreasing one along the 60° rotated canyon. It should be noted that the two trends are not monotonic but, with θ=30°, we found a 20% increase in flow rate between cross-sections 1 and 2 and a small decrease of 6% between cross-sections 2 and 3 (orange arrows in Fig. 5.10d) and, with θ=60°, the decrease is 29% and 22% between cross-sections 1-2 and 2-3, respectively. These results suggest the presence of a vertical advective flux from the external flow into the 30° rotated canyon and a vertical flux from the 60° rotated canyon towards the external flow. Therefore, it appears that the ventilation of the street network is governed by two opposite

mechanisms; the vertical transport of air from the 60° rotated canyon towards the external atmosphere and the entrainment of fresh air from the external flow into the transverse streets. These patterns are in line with the results of numerical simulations by Soulhac et al. (2013), who found downwards mean fluxes along wind-aligned streets and fluxes towards the external atmosphere along perpendicular streets.

Certain features of the flow within the intersections can be identified from the spatial patterns of the mean longitudinal and transversal velocities measured on the surrounding cross-sections. The flow patterns within the two intersecting canyons are driven by helicoidal motions, whose orientation depends on the wind direction. In the intersection, these two flows interact and generate bifurcations or recirculating structures (Carpentieri et al., 2009; Carpentieri and Robins, 2010; Balogun et al., 2010). In particular, within the intersection, the flow along the 30° rotated canyon (see "street 2") separates into a flow that continues along the same canyon and a flow that deviates into the 60° rotated canyon (see orange dashed arrows in panel 5.10d). Therefore, a separation region establishes in correspondence of the upwind corner of the block downwind of the intersection (indicated with the green letter A in panel 5.10d), as highlighted by the almost zero mean longitudinal velocity detected in the upwind corner of cross-section 1 in the 60° rotated canyon (visible in Fig. 5.8a). Moreover, the lateral entrainment of air from the intersection is also proved by the asymmetric distribution of the mean transversal velocity in cross-section 1 (see Fig. 5.8b), which was not found in the canyon without intersections (Fig. 5.4b). The most of the flow along the 60° rotated canyon (see "street 1") is deflected into the 30° rotated canyon (see green dashed arrows in panel 5.10d), forced by the flow along the 30° rotated canyon (Soulhac et al., 2009). This trajectory is coherent with the results found for the mean longitudinal and transversal flows. Notably, we identify a sharp decrease in the mean longitudinal velocity (due to flow detachment at the orange angle A) along the upwind wall of cross-section 1 in the 30° rotated canyon (Fig. 5.7a) and a weak negative transversal mean flow from the upwind wall to the downwind wall, at ground level (Fig. 5.7b). Moreover, in cross-section 3, in the 60° rotated canyon (placed upwind the intersection), the mean longitudinal velocity in the central core of the canyon is nearly zero, indicating a deceleration of the mean longitudinal flow (see Fig. 5.8e), due to the deviation of the flow into "street 2". However, complex

mechanisms generated by the interactions between the flows along the two intersecting streets could lead part of the flow to continue along the 60° rotated canyon (Carpentieri and Robins, 2010). The higher $\overline{u}$ along the upwind wall of cross-section 3 in the 60° rotated canyon, with respect to the central core, may confirm a longitudinal flow along "street 1".

5.4 Conclusions to Chapter 5

In this chapter, we analysed the influence of wind direction, presence of vegetation, and street intersections on the mean and turbulent flow within a square canyon. We performed flow velocity measurements within canyons without (L/H=35) and with (L/H=5) intersections, both subjected to the neutrally-stratified boundary layer modeled above the obstacle Configuration 2. An empty canyon configuration and a vegetated canyon with two rows of trees were reproduced, considering three different wind directions θ={0°,30°,60°}.

In the wind-aligned street canyon without intersections, the flow field is governed by a flow canalisation along the canyon longitudinal axis, while with oblique wind direction the coexistence of a longitudinal flow and a transversal recirculation generates a helicoidal flow structure. This is quite known from previous experimental and numerical studies, but the experiments performed in this study revealed that, with all the wind directions considered, the flow structure and velocity turbulent fluctuations inside the canyon are significantly affected by the presence of trees. The following conclusions can be drawn from the experiments in the canyon without intersections:

- between the trees, the mean longitudinal velocity decreases by 80% with respect to the non-vegetated canyon, regardless of the wind direction. In the oblique wind cases, trees dampen also the transversal recirculation: they lead to a transversal flow towards the upwind wall at ground level 70% lower than the reverse flow at the canyon rooftop.

- The interaction between the external flow and the tree crowns enhances turbulent fluctuations with respect to the empty canyon. With θ=0°, this happens only at the rooftop, while with oblique wind direction a tree-induced increase in turbulent fluctuations with respect to the empty

canyon (up to 40%) verifies also within the canyon, along the downwind wall.

- The mean transversal velocity $\overline{v}$ scales with the sine of θ in the non-vegetated canyon, implying that the transversal recirculation is driven by the component of the free-stream velocity perpendicular to the canyon longitudinal axis, for any wind direction. This scaling is not evident at the rooftop of the vegetated canyon, due to the fact that the shape and the spatial arrangement of trees affect the behaviour of the transversal recirculation differently depending on the wind direction.

- The spatial average of the mean longitudinal velocity in the cross-section of the canyon ($U_{\parallel,log}$) scales with the street-axis parallel component of the free-stream velocity. This result is in line with the analytical model by Soulhac et al. (2008). We found differences of 9%, 22%, and 17% between the analytical spatial average of the mean longitudinal velocity in the canyon cross-section $U_{an,\theta}$ and the experimental $U_{\parallel,log}$, with wind directions θ=0°, θ=30°, and θ=60°, respectively.

- The presence of trees decreases the spatial average of the mean longitudinal velocity by 75% with respect to the non-vegetated canyon, for any wind direction. This demonstrates that, on average, the hindering effect of trees is independent from the wind direction.

In the canyon with intersections and with oblique wind direction (θ={30°,60°}), the interaction between the flow and the corners of the intersection leads to the formation of vertical-axis recirculating structures at the canyon edges. These structures make the canyon flow strongly three-dimensional. The presence of trees attenuates the effects of lateral incoming flows. We obtain the following results in the empty and vegetated canyons with intersections:

- with θ=0°, the presence of street intersections does not alter significantly the longitudinal homogeneity of the mean flow field within the canyon with and without trees;

- With oblique wind direction and in the absence of trees, lateral recirculating structures cause flow detachment regions, alter the transversal recirculation, increase flow velocity fluctuations with respect to the

laterally-closed canyon without trees. These effects modify the spatial pattern of the mean and turbulent flows with respect to the canyon without intersections, mostly close to the upwind intersection with θ=30° and along the whole laterally-opened canyon with θ=60°;

- With oblique wind direction, the presence of trees dampens lateral recirculating structures, although their effects are mostly detectable close to the upwind intersection. There, with θ=30°, we found a transverse flow towards the upwind wall in correspondence of the tree trunks, not visible in the vegetated canyon without intersections. With θ=60°, lateral flows lead to a longitudinal flow channeling between the tree and the downwind wall, in addition to a positive transversal flow between tree trunks. These phenomena are no more visible close to the downstream intersection, where the spatial patterns of the mean longitudinal and transversal velocity are similar to those observed in the laterally-closed vegetated canyon, with both wind directions θ=30° and θ=60°;

- The mean transversal velocity does not scale with the component of the free-stream velocity perpendicular to the canyon axis, since the behaviour of the vertical-axis recirculating structures at the canyon edges depends on the wind direction. Although, these structures are dampened by the trees, the scaling of $\overline{v}/U_{\perp}$ with θ is not evident at the rooftop of the vegetated canyon, highlighting that the interactions between the external flow and the trees is affected by the wind direction;

- With oblique wind direction and in the absence of trees, the spatial average of the mean longitudinal velocity in the cross-section of the canyon with intersections $U_{\parallel,log}$ is heterogeneous along the longitudinal axis. This behaviour revealed the entrainment of fresh air from the external flow into the canyon with wind direction θ=30° and transport of air from the canyon to the external boundary layer, with wind direction θ=60°. The combination of these two results provides insight about the ventilation of a street network, with oblique wind direction;

- The presence of trees reduces the heterogeneity of the spatial average of the mean longitudinal velocity in the cross-section $U_{tr,log}$ along the

laterally-opened canyon, as well as the differences in $U_{tr,log}$ values between configurations with and without intersections;

- With street intersection, the discrepancy between the experimental spatial average of the mean longitudinal velocity $U_{\parallel,log}$, calculated in the centre of the canyon, and the analytical $U_{an,\theta}$ (Soulhac et al., 2008) is almost double the one found in the case without intersections. Notably, the experimental $U_{\parallel,log}$ decreases by 14% and 40% with respect to the analytical $U_{an,\theta}$, with parallel and oblique wind directions, respectively. This result prevents the application of the analytical model, suitable to parametrise the longitudinal advective flow along a two-dimensional canyon, to a canyon with intersection.

The velocity measurements presented in this chapter deepen our understanding of the influence of wind direction, street intersections, and vegetation on the turbulent flow field within urban canyons. These parameters can also have an effect on the canyon ventilation. These effects are investigated in the next chapter, where we will analyse the pollutant concentration field within canyons, with different wind directions and canyon geometries. A limit of the work presented in this chapter is that we did not characterise the complex flow within the intersections, since it requires the measurement of the three velocity components, which was not feasible, due to the difficulty of introducing the LDA coupled with a mirror (necessary for measuring the vertical velocity component, w) into the intersection.

Chapter 6

Experimental evaluation of the canyon ventilation

The ventilation efficiency of an urban canyon is determined by advective and turbulent exchanges of pollutants between the canyon and the external flow. Some experimental studies quantifies this phenomenon evaluating the Pollutant Exchange Rate (PCH) of the canyon (Liu et al., 2005), defined as the integral of the vertical turbulent mass fluxes across the canyon rooftop. Di Bernardino et al. (2018) performed coupled measurements of velocity and concentration within a two-dimensional canyon, with different aspect ratio, to evaluate experimentally the PCH. The results revealed a strong dependence of PCH from the canyon aspect ratio, in line with what found by Liu et al. (2005) using LES simulations. With a similar experimental approach, Marucci and Carpentieri (2019) calculated the PCH parameter with different wall heating conditions. However, the experimental evaluation of the PCH requires high-resolution simultaneous measurements of concentration and velocity turbulent fluctuations, which involve the employment of a complex and space-demanding experimental apparatus.

In dispersion models at the city scale, like SIRANE (Soulhac et al., 2011, 2013), the canyon ventilation is parametrised by means of the bulk vertical exchange velocity between the canyon and the overlying flow. The evaluation of this quantity requires only knowledge of the pollutant flow rate at the source and the overall average concentration within the canyon. Salizzoni et al.

(2009) provided a first experimental estimate of this quantity measuring the wash-out process of the canyon. They show that the vertical exchange velocity depends on the external turbulent flow conditions. The influence of turbulence intensity within the canyon on the vertical exchange velocity was analysed by Fellini et al. (2020), who measured the wash-out process for different canyon geometries, wall roughness, and wall heating conditions. In these studies, the wash-out curves for the street canyon were evaluated using a two-box model, in which each box represents a specific region of the canyon with its own recirculating and transport dynamics. This methodology is applicable in cases where well-established recirculating flow structures exist within the canyon, as in two-dimensional streets with perpendicular incident wind. However, in vegetated street canyons or under non-orthogonal wind directions, accurately describing the flow field and linking it to well-defined recirculating structures becomes challenging. In these complex conditions, the bulk vertical exchange velocity between the canyon and the external flow can be evaluated, modeling the canyon as a closed box characterised by well-mixed concentration. Fellini et al. (2022) performed high-resolution concentration measurements within a closed cavity, perpendicular to the external flow, to obtain a reliable value for the spatial average of the mean concentration within the canyon. They considered different vegetation densities. They found that the presence and density of vegetation do not significantly influence the vertical exchange velocity within the canyon, even though their considerable effect on the local distribution of the pollutant concentration. However, studies addressing non-orthogonal wind directions or the influence of street geometry on canyon ventilation are completely missing. In a numerical study, Buccolieri et al. (2015) demonstrated that the vertical exchange velocity depends on the wind direction, the urban canopy geometry, and lateral turbulent mass fluxes at the street intersections. These findings still need to be validated through comparison with experimental data.

Therefore, we performed an experimental campaign aimed at characterising the mean concentration field within a vegetated canyon with and without intersections, for different wind directions. Combining the concentration data with the flow velocity data collected in the experimental campaign presented in Chapters 4 and 5, we provide an estimate of the ventilation efficiency of the canyon. After analysing the spatial patterns of the mean concentration

within the canyon without (Sect. 6.2.1) and with (Sect. 6.3.1) intersections, we analyse the influence of wind direction, presence of vegetation, and street intersections on the vertical exchange velocity between the canyon and the external boundary layer (Sects. 6.2.2 and 6.3.2).

6.1 Experimental details

Within the street network of Configuration 2 (see Fig. 6.1a), we selected a reference street canyon 3.5 m long and with H/W=1, laying on the rotating platform (grey blocks in Fig. 6.1a). We considered the same vegetation configurations, canyon geometries, and wind directions considered in Chapter 5 (see Sect. 5.1). Notably, at first, we closed the lateral boundaries of the reference canyon to model a two-dimensional canyon with L/H=35, then we removed the blocks in correspondence of the street intersections and we selected a portion of street with L/H=5 between two street intersections. We analysed the mean concentration field in the Zero (panels 6.1b and 6.1d) and Full (panels 6.1c and 6.1e) vegetation configurations and with wind directions θ={0°,30°,60°}. A ground-level point source was inserted within the reference canyon (blue point in all panels of Fig. 6.1), about $11H$ far from the entrance of the reference canyon. It consists of a plastic tube with 8 mm diameter, emitting ethane at a flow rate of 0.5 l/min, allowing an emission velocity (equal to 0.16 ms^{-1}) sufficiently low to avoid flow perturbation in the canyon. It is worth mentioning that we used a point source, since it was not possible to create a homogeneous linear source that occupies the entire length of the reference canyon. The origin of the reference system was located in correspondence of the point source with the x-, y-, and z-axis oriented in the streamwise direction, transversal direction and upwards, respectively (see red arrow in Fig. 6.1a).

We used the FID to perform concentration measurements (details on this technique in Sect. 2.2.3). In the laterally-closed canyon, the scalar concentration was measured in around 200 points distributed on two-dimensional cross-sections, located along a defined control volume of the canyon, sufficiently far from the point source to be sure that the canyon is completely filled by the pollutant plume. We verified this condition checking that the spatial pattern of the mean pollutant concentration was almost homogeneous along the control

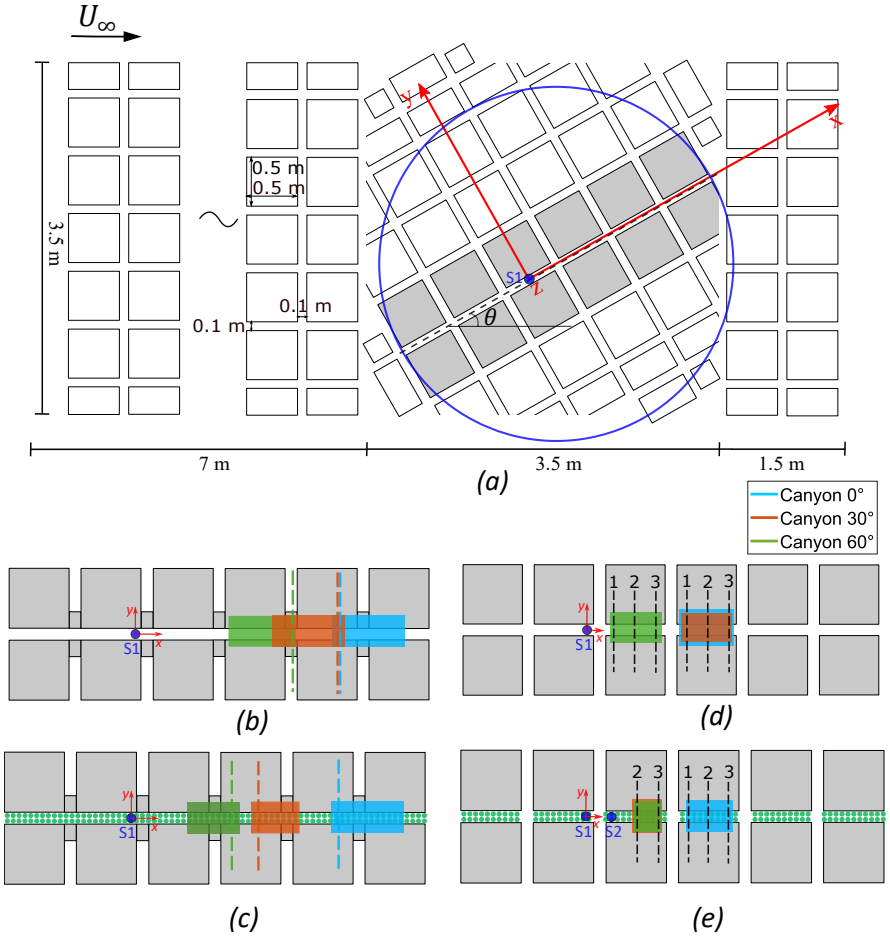


Figure 6.1 (a) Scheme of the urban canopy in Configuration 2, with the reference street canyon rotated of 30° with respect to the external wind. The blocks confining the reference canyon are coloured grey. The red arrows represent the reference system of the reference canyon, the big blue circle the rotating platform, and the small blue dot the ground-level pollutant source. Planar view of the canyon without intersections without (b) and with (c) vegetation. Dashed lines indicate the position of the cross-sections discussed in Sect. 6.2.1. Planar view of the canyon with intersections without (d) and with (e) vegetation. Black dashed lines indicate the positions of the cross-sections close to the upwind intersection (cross-section 1), in the canyon centre (cross-section 2), and close to the downwind intersection (cross-section 3). Blue, orange and green rectangles represent the measuring control volume, with wind directions θ=0°, θ=30°, and θ=60°, respectively.

volume. Note that as the wind angle increases, measurements were collected closer and closer to the source, since concentration levels decrease more rapidly along the canyon as θ increases (see coloured rectangles in panels 6.1b-e). This is evident also in the vegetated canyon. The measuring grid is the same adopted for flow velocity measurements, notably with horizontal resolution of 2 cm and vertical resolution of 2 cm in the range $0.2 \leq z/H \leq 0.8$ and 1 cm in the range $0.8 \leq z/H \leq 1$.

In the presence of street intersections, the measuring cross-sections were distributed regularly along the portion of the reference canyon between two intersections. With oblique wind direction and in the presence of trees, we moved the point source inside the same portion of the canyon where we performed concentration measurements (see "S2" in Fig. 6.1e), close to the upwind intersection, to avoid that, passing trough the intersection, the pollutant is deviated into the cross-wind streets before entering in the main canyon, due to lateral obstruction by trees. For this reason, in the vegetated laterally-opened canyon, with wind directions θ=30° and θ=60°, we did not collect concentration data close to the upwind intersection.

6.2 Concentration field in a street canyon without intersections for different wind directions

We analyse the influence of the presence of trees and wind direction on the spatial pattern of the mean scalar concentration field within a canyon without intersections (Sect. 6.2.1). Afterwards, we estimate the bulk vertical exchange velocity, to asses the ventilation efficiency of the canyon (Sect. 6.2.2). The mean concentration is normalised by the ethane mass flow rate as $\overline{c_{ad}} = \overline{c}HWU_{\parallel,log}/Q_{et}$, where $\overline{c}$ is the mean of the concentration time series, H and W are the height and width of the canyon, Q_{et} is the ethane mass flow rate emitted at the source, and $U_{\parallel,log}$ is the spatial average in the cross-section of the empty canyon of the experimental mean velocity component parallel to the canyon longitudinal axis. As explained in Chapter 5, this velocity is estimated as the spatial average of the $\overline{u}$ measurements resampled onto a 5 mm resolution grid using linear interpolation and weighted by the cell associated to each measurement point, adding the missing data close to the canyon boundaries

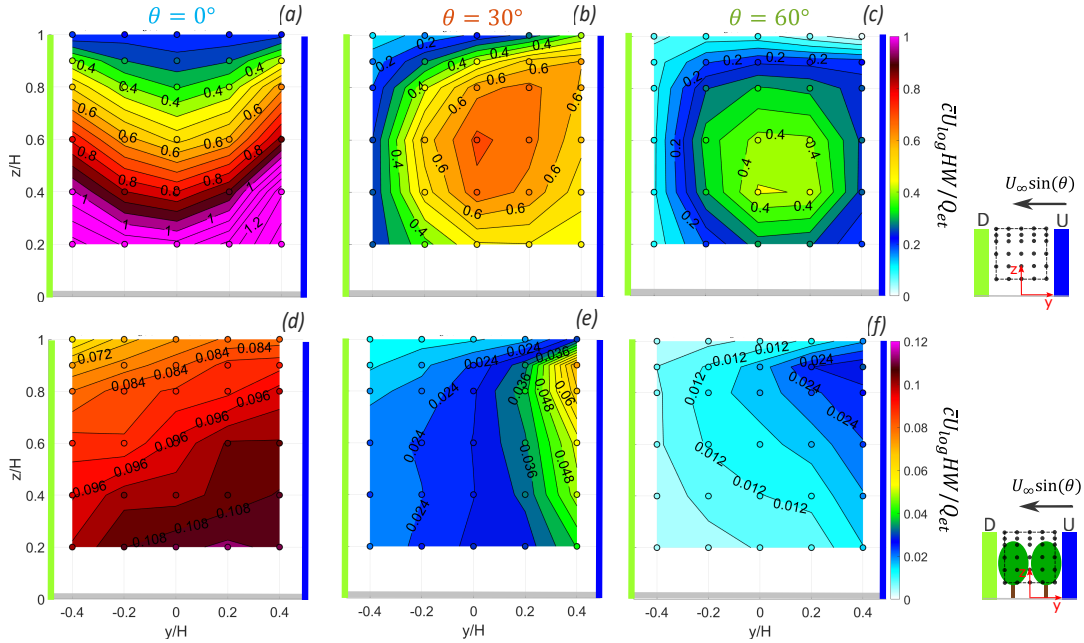


Figure 6.2 Transversal behaviour of the mean concentration within the empty canyon, with wind directions θ=0° (a), θ=30° (b), and θ=60° (c). (d-f) Same as (a-c), but in the vegetated canyon. Green and blue bars indicate the downwind and upwind walls of the canyon (see sketches on the right).

by extrapolation with logarithmic law. Similarly, for the vegetated case, the scalar concentration is normalized by $U_{tr,log}$. Comparing spatial patterns of the non-dimensional mean concentration between different cross-sections, we found that they are very similar along the canyon for both the empty and vegetated cases (without intersections). For this reason, we report in the following $\overline{c_{ad}}$ on a single two-dimensional cross-section, obtained by linearly interpolating point measures (the positions of the cross-sections with respect to the pollutant source are visible in panels 6.1b-c).

6.2.1 Cross-sectional concentration field in the street canyon

In the wind-aligned canyon without trees, the distribution of the mean concentration (Fig. 6.2a) is symmetrical with respect to the vertical axis of the canyon: concentration values increase by 20% moving from the centre towards the right and left walls, reaching similar values close to both walls. In the

vertical direction, $\overline{c_{ad}}$ values monotonically decrease from around 1 at ground level to 0.2 at the rooftop. The mean concentration behaviour is opposite to that of the mean longitudinal velocity (see Fig. 5.2a). In fact, $\overline{c_{ad}}$ is high at the canyon floor and walls, where the mean longitudinal velocity approaches zero, and low at the rooftop, where both the mean and turbulent velocity fields reach their maximum values.

With oblique wind direction and without trees (panels b and c in Fig. 6.2), $\overline{c_{ad}}$ shows an asymmetric pattern with respect to the vertical axis of the canyon, with concentration levels at the upwind wall almost double those at the downwind wall. Moreover, the maximum scalar concentration is in the central core of the canyon, contrary to what observed with θ=0°. In particular, with θ=30°, $\overline{c_{ad}}$ (Fig. 6.2b) is equal to 0.7 in the centre of the cross-section and monotonically decreases to 0.2 at the rooftop and along the downwind wall and to around 0.5 at ground level and at the upwind wall. A similar spatial pattern with lower concentration levels is visible with θ=60° (see Fig. 6.2c): $\overline{c_{ad}}$ is equal to 0.4 in the central core, 0.1 at the rooftop and along the downwind wall, and around 0.25 near the upwind wall and close to the ground. These peculiar behaviours are induced by the helicoidal flow structure established within the canyon, with oblique wind direction (as discussed in Sect. 5.2.1). In particular, the difference in $\overline{c_{ad}}$ values between the upwind and downwind walls is a result of the transversal recirculation: the external air enters the canyon at the downwind wall and transports the pollutant towards the upwind wall. Simultaneously, the mean longitudinal flow leads to the accumulation of the scalar concentration along the longitudinal axis of the canyon. In the canyon centre, the low intensity of velocity turbulent fluctuations prevents the pollutant to be mixed over the canyon cross-section. Conversely, the interaction between the external boundary layer and the canyon flow at the rooftop and along the downwind wall leads to high fluctuation intensity of the velocity (panels c and d of Figs. 5.3 and 5.4), thus to low mean scalar concentration in these regions. It is worth noting that, at a distance of approximately $15H$ from the source (which is the position of the cross-sections shown in panels 6.2a-6.2c), the maximum $\overline{c_{ad}}$ value decreases with the increase of the wind angle; looking at the maximum values, we observe that there is a difference of 40% from θ=0° to θ=30° (maximum mean concentration drops from 1.2 to 0.7, respectively) and 36% reduction from θ=30° to θ=60° (maximum mean

concentration decreasing to 0.45). Similar considerations can be made near ground level: at z/H=0.2, $\overline{c_{ad}}$ for θ=0° (equal to 1.2) is twice that for θ=30° (around 0.5) and almost four times that for θ=60° (around 0.2). These results suggest that the transversal recirculation favours the wash-out process within the street canyon. Moreover, with oblique wind direction the air quality at the pedestrian level is better than in a wind-aligned canyon.

The presence of trees hinders the flow canalization and the helicoidal flow structure within the canyon (panels e and f of Figs. 5.2-5.4). Panels d-f in Fig. 6.2 confirms that the spatial pattern of the mean scalar concentration is different from that in the empty canyon, regardless of the wind direction. Moreover, the $\overline{c_{ad}}$ values are approximately 90% lower than in the empty canyon in the whole cross-section and with all wind directions. This hold true even considering that, under oblique wind conditions, measurements were taken about $0.7H$ closer to the point source compared to the non-vegetated case (i.e., concentration measurements were collected in cross-sections $10H$ and $8H$ far from the source with θ=30° and θ=60°, respectively – see Fig. 6.1c).

With θ=0°, trees lead to the partial homogenisation of $\overline{c_{ad}}$ in the canyon cross-section (see Fig. 6.2d). In fact, the monotonic increases in $\overline{c_{ad}}$ from the bottom to the top of the cross-section observed in the empty canyon is maintained, but the difference between maximum (around 0.1) and minimum (equal to 0.07) values decreases to 30%. This difference is less than half that in the empty canyon (equal to 83%). In the transversal direction, $\overline{c_{ad}}$ increases by around 20% moving from the left-hand wall to the right-hand wall. This asymmetrical behavior is reasonably due to the sensitivity of the mean concentration to small asymmetries in the experimental setup and to the heterogeneous shape and orientation of the trees.

The spatial distribution of the mean scalar concentration within the vegetated canyon is similar between θ=30° and θ=60°, as observed in the empty canyon. Notably, the scalar concentration accumulates in the upper upwind corner of the canyon, whilst it shows low values in the centre and at the rooftop. For θ=30°, $\overline{c_{ad}}$ (Fig. 6.2e) is equal to 0.07 in the upper upwind corner of the canyon (at y/H=+0.4 and z/H=0.9) and it decreases to 0.04 moving towards the upwind lower corner. In the canyon centre and along the downwind wall $\overline{c_{ad}}$ is almost 0.02, and it decreases to 0.01 at the rooftop. The difference in

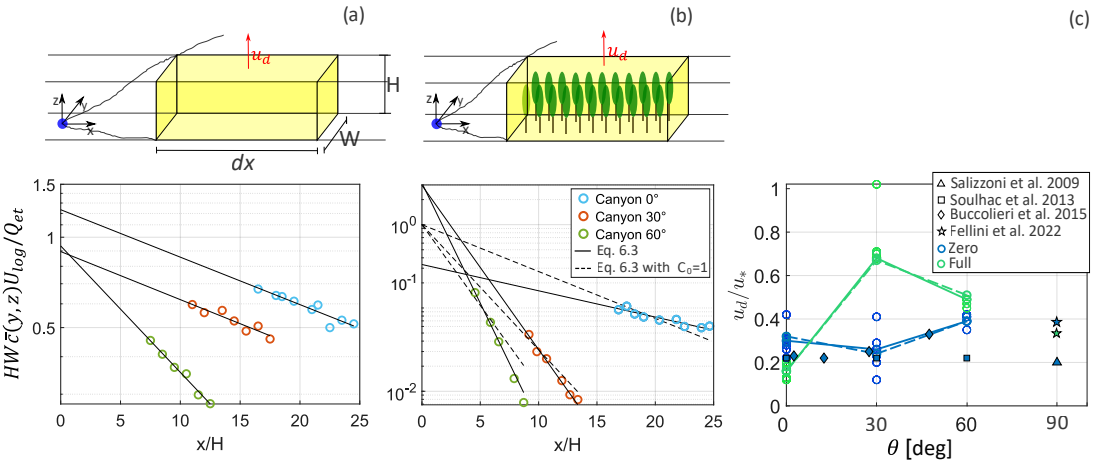


Figure 6.3 Longitudinal evolution of the non-dimensional transversally-averaged mean concentration in the cross-section of the empty (a) and vegetated (b) canyons. Blue, orange, and green colors indicate wind directions θ=0°, θ=30°, and θ=60°, respectively. The yellow box in the sketches indicates the control volume. (c) Variation of u_d with θ and comparison with other literature studies. Dashed and continuous lines refer to u_d estimated from Eq. (6.3) and Eq. (6.5), respectively.

$\overline{c_{ad}}$ between the upwind and downwind wall is around 70%. For θ=60° (Fig. 6.2f), the maximum mean concentration in the upper upwind corner is equal to 0.03, while $\overline{c_{ad}}$ decreases to 0.01 in the canyon centre and to 0.007 close to the downwind wall. Considering that trees dampen the mean flow within the canyon, the spatial behaviour of the mean scalar concentration is induced by the heterogeneous intensity of velocity turbulent fluctuations over the canyon cross-section. We found high turbulent fluctuation intensity of the velocity at the rooftop and along the downwind wall, induced by the interaction between the external flow and the tree crowns (see Figs. 5.3g-h and 5.4g-h). On the other hand, velocity turbulent fluctuations are inhibited in correspondence of the upwind tree leading to the accumulation of the scalar concentration at the upwind wall.

6.2.2 Vertical exchange velocity

After analysing the influence of wind direction and trees on the mean scalar concentration field, we investigate their effects on the ventilation efficiency. In operational urban dispersion models (Soulhac et al., 2011, 2013), the ventilation efficiency of canyons is determined by the vertical turbulent mass fluxes $\overline{w'c'}$

between the canyon and the external flow, that occur at the rooftop. The experimental evaluation of $\overline{w'c'}$ is a difficult task, that requires the simultaneous measurements of velocity and concentration fluctuations, with the LDA-FID system. This experimental technique cannot be used in our experiment, due to the impossibility of introducing the LDA coupled with the FID and a mirror in the square canyon. Therefore, the turbulent transfer at the canyon rooftop is parametrised using the bulk vertical exchange velocity u_d, evaluated using the box model approach (Salizzoni et al., 2009; Soulhac et al., 2013). In the following, we present a first attempt of evaluating u_d from experimental data, considering different wind directions and vegetation configurations.

We identified a control volume of thickness dx within the canyon, sufficiently far from the point source to guarantee that the mean concentration field has reached steady state conditions (see sketches in panels 6.3a-b). The origin of the x-axis is located in correspondence of the pollutant source, located outside the control volume, so that the non-dimensional mean concentration at the source is $\overline{c_{ad}}(x/H = 0)$=1. Assuming steady state conditions and neglecting mass fluxes throughout the lateral boundaries, the canyon ventilation can be described with a mass balance between the longitudinal pollutant advective flux entering and leaving the control volume and the vertical mass flux towards the external flow at the rooftop. This mass balance is written as:

$$-\frac{\partial}{\partial x}\{HW[U_{\parallel,log}C_{ad}(x) + \overline{u'c'}(x)]\}dx = u_d C_{ad}(x) W dx \tag{6.1}$$

where $U_{\parallel,log}$ represents the longitudinal advective flow, C_{ad} is the transversally-averaged non-dimensional mean concentration – calculated as the spatial average of the mean concentration $\overline{c_{ad}}$ resampled onto a 1 cm resolution grid using linear interpolation and weighted by the cell associated to each measuring point –, $\overline{u'c'}$ is the longitudinal turbulent mass flux, and u_d is the vertical exchange velocity at the canyon rooftop. The velocity $U_{\parallel,log}$ can be considered constant along the x-axis of the canyon and we assume $\overline{u'c'}/(U_{\parallel,log}C_{ad}) << 1$, thus the mass balance (6.1) can be simplified as

$$\frac{dC_{ad}(x)}{dx} = -\frac{u_d}{U_{\parallel,log}H}C_{ad}(x). \tag{6.2}$$

The solution of Eq. (6.2) provides the longitudinal evolution of C_{ad} along the non-dimensional longitudinal axis x/H of the canyon

$$C_{ad}(x/H) = C_0 \exp\Big\{-\frac{u_d x}{U_{\parallel,log} H}\Big\}, \tag{6.3}$$

where C_0 and $C_1 = u_d/U_{\parallel,log}$ are the parameters of the exponential function, which represent the mean pollutant concentration at the source (at x/H=0) and the vertical exchange velocity normalised by the mean longitudinal velocity, respectively. Following the same reasoning, Eq. 6.3 can written for the vegetated canyon, replacing $U_{\parallel,log}$ with the longitudinal velocity along the vegetated canyon.

In Fig. 6.3a-b, we plot the evolution of the experimental C_{ad} along the control volume of the empty and vegetated canyons, with wind directions θ=0°, θ=30°, and θ=60°. We fitted the experimental data with Eq. (6.3), to obtain the parameters C_0 and C_1 that minimize the sum of the square difference between the exponential function and the experimental data. From the parameter C_1 we estimated the vertical exchange velocity $u_d = C_1 U_{\parallel,log}$ in the empty and vegetated canyons. In the empty canyon (Fig. 6.3a), the mean concentration C_{ad} decays exponentially along x, regardless of the wind direction. This exponential behaviour is confirmed by the good overlap between Eq. (6.3) and the experimental C_{ad}, which provides a parameter C_0 equal to around 1, thus, a mass flux $\overline{c}U_{\parallel,log}HW$ at the source equal to the ethane mass flow rate Q_{et}. The estimated bulk exchange velocity u_d within the empty canyon (see blue dashed line in panel 6.3c) does not exhibit a clear trend with θ: u_d/u_* decreases by 25% as θ increases from 0° to 30°, and then rises by 38% from 30° to 60°. In the vegetated canyon, the exponential decay of C_{ad} is still detectable for all wind directions (see Fig. 6.3b), but the best-fit between Eq. (6.3) and the experimental C_{ad} provides values of C_0 equal to 0.3 and 3 for the parallel and oblique wind directions, respectively. This means that the mass flux at the source is different from Q_{et}. An explanation for this discrepancy is that the mass balance (6.2) does not completely describe the ventilation process in the vegetated canyon, since turbulent mass fluxes $\overline{u'c'}$ are not negligible with respect to the advective flux and contribute to the transport of the scalar concentration along the vegetated canyon. The u_d values, calculated from the parameter C_1 (green dashed lines in panel 6.3c), show a variation with θ more

marked than in the non-vegetated canyon: u_d/u_* increases by 76% as theta rises from 0° to 30°, and then decreases by 24% between 30° and 60°. Furthermore, under oblique wind direction, the vertical exchange velocity in the vegetated canyon exceeds that in the empty canyon, while the opposite is observed when the wind is aligned with the street axis. In particular, trees lead to an increase in u_d/u_* of 64% and 23% for θ=30° and θ=60°, respectively. For oblique wind direction, we estimated u_d also from the best-fit between the experimental C_{ad} and the exponential function (6.3) setting C_0=1. We obtained u_d/u_* values equal to 0.51 and 0.34, for θ=30° and θ=60°, respectively. When θ=30°, the difference in u_d/u_* between the empty and vegetated canyons reduces to 50% (as u_d/u_* is equal to 0.24 in the empty canyon), while for θ=60° u_d/u_* results 13% lower in the vegetated canyon than in the empty one (where u_d/u_* is equal to 0.39). However, it should be noted that the exponential function with only one parameter C_1 does not show a perfect overlap with the experimental data (see black dashed lines in panel 6.3b).

A second method to apply the box model approach to assess the canyon ventilation is to model the canyon as a closed box characterised by almost well-mixed concentration C_{vol}, without considering the exponential decay of the mean concentration along the x-axis (Fellini et al., 2022). Assuming that (i) the turbulent mass transfer between the canyon and the external flow occurs only at the canyon rooftop and it is parametrised by the bulk vertical exchange velocity, (ii) the system is in steady state conditions, (iii) the pollutant concentration is well mixed within the box, (iv) there are no transversal mass fluxes throughout the lateral boundaries and (v) $\overline{u'c'}/U_{\parallel,log}C_{ad} << 1$, the mass balance between the longitudinal advective mass flux entering and leaving the box and the turbulent pollutant flux at the rooftop is:

$$HWU_{\parallel,log}C_{ad}(x) - HWU_{\parallel,log}C_{ad}(x + \Delta x) = W\Delta x u_d C_{vol} \tag{6.4}$$

where $U_{\parallel,log}C_{ad}$ is the longitudinal advective mass flow rate throughout the transversal cross-sections upwind (x) and downwind ($x + \Delta x$) the control volume, C_{vol} is the spatial average of the mean scalar concentration over the whole control volume – calculated averaging the $C_{ad}(x)$ values weighted by the distance between the measuring cross-sections –, and H, W, and Δx are the height, width and length of the box. From Eq. (6.4), the bulk vertical exchange

velocity u_d can be estimated as

$$u_d = \frac{HU_{\parallel,log}[C_{ad}(x) - C_{ad}(x + \Delta x)]}{\Delta x C_{vol}}. \tag{6.5}$$

In Fig. 6.3c, we report the variation of u_d/u_*, calculated from Eq. (6.5), with the wind direction, in the empty and vegetated canyons. The different points refer to different u_d/u_* values calculated progressively increasing the length Δx of the control volume. We observe that the u_d/u_* values are almost equal to those obtained with the exponential law fitting of the experimental C_{ad}. As discussed above, the u_d/u_* values do not show a well-defined trend with the wind direction, regardless of the presence of trees. Furthermore, with oblique wind direction, the presence of trees induces a remarkable increase in u_d/u_* – notably, 64% and 23% for θ=30° and θ=60°, respectively – with respect to the non-vegetated canyon. This tree-induced increase of the ventilation efficiency of the canyon is in line with the lower concentration levels detected in the vegetated canyon with respect to the empty one, found for oblique wind direction. However, this consideration cannot be applied to the wind-aligned canyon. When comparing the u_d values obtained for different wind directions and vegetated configurations, there is an aspect to be considered. In all cases, we estimated u_d from the mean concentration field downstream a point source located at ground level. This source configuration provided a steady mean concentration behaviour with maximum concentration at ground level within wind-aligned canyons. For oblique wind direction, a complex three-dimensional flow structure caused a pollutant accumulation in the central core of the empty canyon and in the upper upwind corner of the vegetated canyon (see Figs. 6.2b-c and 6.2e-f). These are not typical behaviours of a mean scalar field generated by a ground-level source, which normally expects maximum concentrations at ground level. This issue, linked to the point source used in our experiment, has to be considered when comparing u_d values obtained for different wind directions, since the u_d parameter is sensitive to the position of the source.

Our estimates of u_d/u_* are compared with those of other studies, which refer to the u_d parameter to asses the ventilation efficiency of a canyon. With wind direction θ=90°, Salizzoni et al. (2009) found an experimental estimate of u_d/u_* equal to 0.20, using a two-box model approach to describe the wash-out of a two-dimensional canyon with a ground level linear source. The

different analytical model, experimental setup, and wind direction explain the discrepancy of $17 \div 49\%$ (depending on the wind direction) compared to the u_d/u_* values obtained in our experiment. An other experimental estimate of u_d/u_* is provided by Fellini et al. (2022), whose work is the only one investigating the influence of the vegetation density on the ventilation efficiency of a large canyon (H/W_w=0.5), perpendicular to the external wind. They found that the presence of vegetation affects the spatial distribution of the pollutant concentration within the canyon, but it has limited effects on the canyon ventilation. They found a difference of 10% in the vertical exchange velocity between the empty and vegetated canyons, which is 7 times lower than that found in the present study for θ=30° (equal to 64%) and half that found for θ=60° (equal to 23%). In the operational urban dispersion model SIRANE (Soulhac et al., 2011, 2013), the bulk vertical exchange velocity is modeled with the analytical model $u_d = \sigma_w/\sqrt{2}\pi$, which considers u_d proportional to the vertical velocity fluctuations σ_w at roof level and independent from the wind direction and canyon geometry. This analytical model provides u_d/u_* equal to 0.22 for any wind direction, considering $\sigma_w/u_*(z = H) \sim 1$ (true also in the present study). This analytical u_d is 31%, 8%, and 44% lower than those found in the empty canyon of the present study with θ=0°, θ=30°, and θ=60°, respectively. This heterogeneous difference between the analytical and the experimental u_d varying the wind angle suggests that the wind direction should be considered in the evaluation of the ventilation efficiency of the canyon. The variation of u_d/u_* with the wind direction was investigated with numerical simulations by Buccolieri et al. (2015), within a three-dimensional street canyon. They found that the increase in the wind angle leads to an increase of the turbulent transfer between the canyon and the external flow, thus to an increase in u_d/u_*. The clear dependence of u_d/u_* from θ, hardly found in the canyon of the present study, is linked to the complex flow topology which arises inside a canyon with intersections increasing the wind angle.

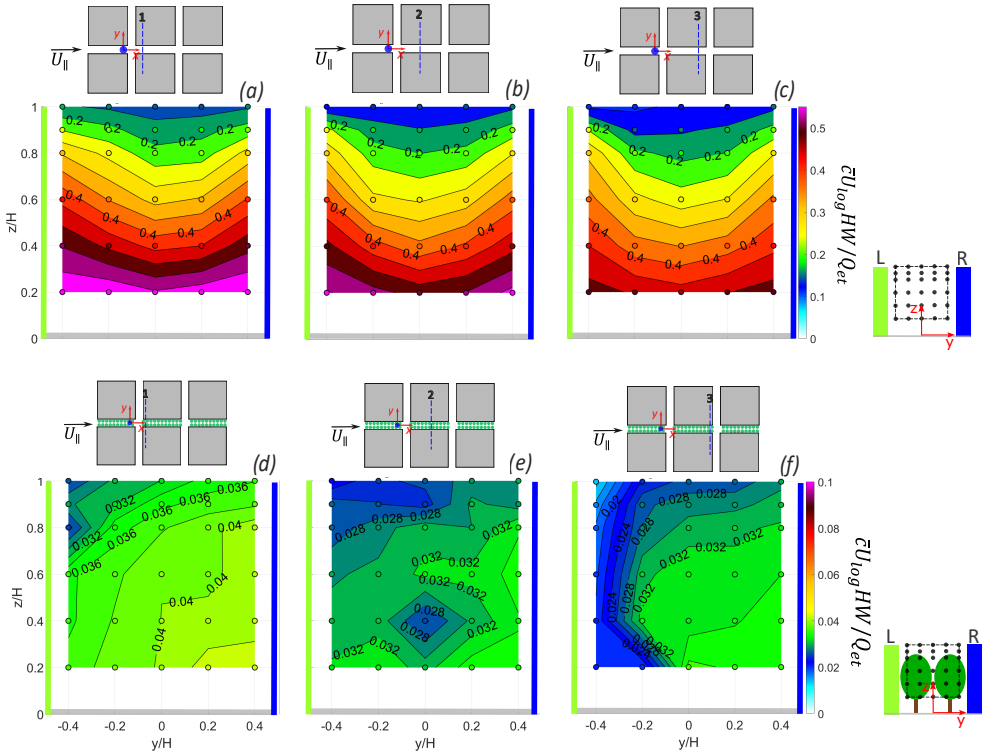


Figure 6.4 Transversal behaviour of the mean concentration in the empty canyon, close to the upwind intersection (a), in the centre of the laterally-opened canyon (b), and close to the downwind intersection (c), with wind direction θ=0°. (d-f) Same of (a-c) in the vegetated canyon. Green and blue bars indicate the left and right walls of the canyon (see sketches on the right).

6.3 Concentration field in a street canyon with intersections for different wind directions

6.3.1 Cross-sectional concentration field in the street canyon

To analyse the influence of street intersections on the mean concentration field, we report the non-dimensional mean concentration on three two-dimensional cross-sections: close to the upwind intersection, in the centre of the canyon, and close to the downwind intersection (cross-sections 1, 2, 3 in panels 6.1d-e). As already introduced in Sect. 6.2, the non-dimensional concentration in the empty canyon is expressed as $\overline{c_{ad}} = \overline{c}HWU_{\parallel,log}/Q_{et}$, where $U_{\parallel,log}$ is the average of the $U_{\parallel,log}$ values calculated averaging the experimental $\overline{u}$ data in cross-sections 1, 2,

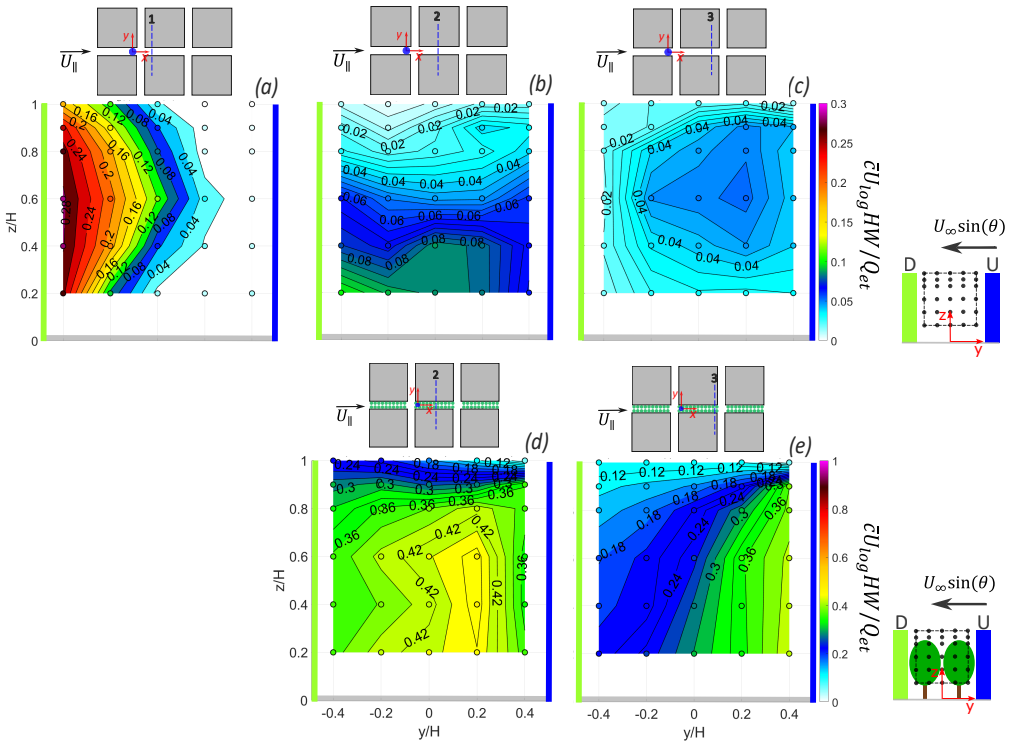


Figure 6.5 Transversal behaviour of the mean concentration in the empty canyon, close to the upwind intersection (a), in the centre of the laterally-opened canyon (b), and close to the downwind intersection (c), with wind direction θ=30°. (d-e) Same of (b-c) in the vegetated canyon. Green and blue bars indicate the downwind and upwind walls of the canyon (see sketches on the right).

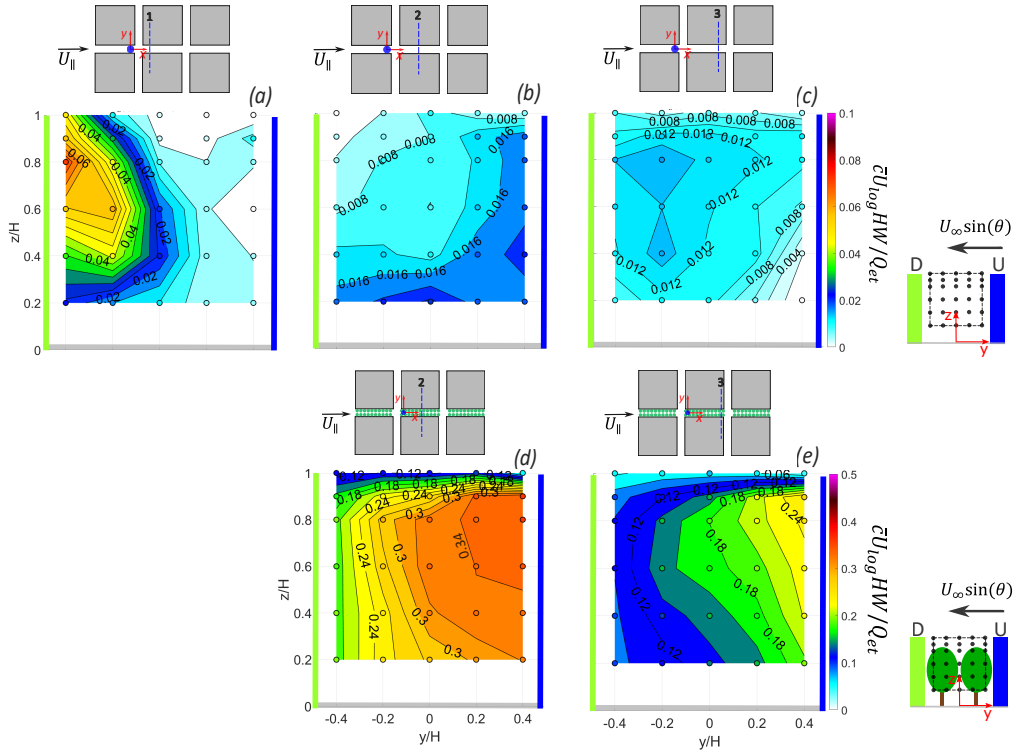


Figure 6.6 Transversal behaviour of the mean concentration in the empty canyon, close to the upwind intersection (a), in the centre of the laterally-opened canyon (b), and close to the downwind intersection (c), with wind direction θ=60°. (d-e) Same of (b-c) in the vegetated canyon. Green and blue bars indicate the downwind and upwind walls of the canyon (see sketches on the right).

and 3. The same approach was used to calculate the reference velocity $U_{tr,log}$ within the vegetated canyon.

In the wind-aligned street canyon without trees, the mean scalar concentration exhibits the same spatial pattern in the three cross-sections (see panels 6.4a-c): it decreases monotonically from ground level to the canyon rooftop and slightly increases from the centre to the side walls, symmetrically with respect to the vertical canyon axis. This behaviour is the same observed in the laterally-closed canyon (Fig. 6.2a), demonstrating that the presence of intersections does not affect the spatial distribution of $\overline{c_{ad}}$ within the wind-aligned canyon. The $\overline{c_{ad}}$ values close to the ground (z/H=0.2) slightly decrease along the canyon, as expected moving far away from the point source. A more heterogeneous pattern shows up in the vegetated canyon (see panels 6.4d-f). This is in contrast to the longitudinally homogeneous and quite symmetric behaviour of the mean and turbulent flow fields, found in the vegetated laterally-opened canyon (see Figs. 5.6a-h). However, the difference between the maximum and minimum concentration over each cross-section is less than half that in the empty canyon. Close to the upwind intersection (Fig. 6.4d), $\overline{c_{ad}}$ decreases monotonically from the lower right-hand corner of the canyon ($\overline{c_{ad}}$ equal to around 0.042) to the upper left-hand corner (where $\overline{c_{ad}}$ is equal to around 0.02). In the cross-sections in the centre and close to the downwind intersection, we detect a difference between the maximum and minimum $\overline{c_{ad}}$ values equal to 18%, thus lower than that found in the cross-section close to the upwind intersection. In the centre of the canyon (Fig. 6.4e), it is difficult to identify a clear monotonic concentration pattern, while close to the downwind intersection (Fig. 6.4f), there is a well-defined zone of $\overline{c_{ad}}$ equal to 0.02 along the left wall and a zone with $\overline{c_{ad}}$ equal to 0.032 in the centre of the canyon and along the right wall. The asymmetrical spatial pattern of the mean concentration and its longitudinal heterogeneity suggest that in the presence of street intersections the spatial distribution of the mean concentration is sensitive to the random shape and orientation of the model trees.

For oblique wind direction, the interaction between the corners of the intersections and the air flow leads to the formation of vertical-axis recirculating structures at the canyon edges. Consequently, flow and concentration fields are strongly three-dimensional. When θ=30°, the scalar concentration in the non-vegetated canyon accumulates mainly close to the downwind wall of cross-

section 1 (Fig. 6.5a). In fact, $\overline{c_{ad}}$ is equal to around 0.3 at the downwind wall and to zero at the upwind wall. This asymmetrical spatial pattern is probably induced by the entrance of air from the intersecting streets (Fig. 5.10d), that causes a flow detachment region along the upwind wall, with high intensity of velocity turbulent fluctuations (see Fig. 5.7c-d). Consequently, the pollutant mixing is more efficient at the upwind wall than at the downwind wall. Moreover, the accumulation of pollutant at the downwind wall is favoured by the negative mean transversal velocity at the canyon rooftop and close to the ground (see Fig. 5.7b), which transports the pollutant in this area of the cross-section. In the centre of the canyon (Fig. 6.5b), the mean scalar concentration shows a vertical stratification: $\overline{c_{ad}}$ is equal to 0.1 close to the ground, to 0.06 close to the centre and to 0.02 at the rooftop. Note that, at ground level, there is an around -50% difference between the downwind and upwind lower corners of the canyon. This asymmetry demonstrates that the transversal recirculation, which involves a positive flow from the downwind to the upwind wall at ground level, does not develop in the centre of the laterally-opened canyon. Close to the downwind intersection (Fig. 6.5c), the spatial pattern of the mean scalar concentration recalls that found in the laterally-closed empty canyon (Fig. 6.2b), with a central core of high mean concentration levels and low concentration around it. This pattern suggests the restoration of the helicoidal structure, which implies the entrainment of air from the external flow into the canyon at the rooftop and along the downwind wall, where $\overline{c}_{ad}$ shows the minimum values (around 0.02) and a longitudinal component of the mean flow responsible for the accumulation of pollutants along the x-axis of the canyon (where $\overline{c}_{ad}$ is equal to 0.05). Moreover, also the distribution of the intensity of velocity turbulent fluctuations (see Figs. 5.7g) drives the spatial pattern of the mean concentration in this cross-section. In particular, the pollutant accumulation in the central core is favoured by low velocity fluctuations in this region, while low concentration levels at the rooftop and along the downwind wall are due to high velocity fluctuations induced by the interaction between the canyon flow and the external boundary layer.

The presence of trees in the 30° rotated canyon hinders the development of the vertical-axis recirculating structures at the canyon edges, leading to a spatial pattern of the mean and turbulent flow fields quite homogeneous along the canyon x-axis. However, the spatial pattern of the mean scalar

concentration is different in the cross-sections measured in the canyon centre and close to the downwind wall (we recall that with oblique wind direction, the pollutant source is located inside the laterally-opened canyon close to the upwind intersection – Fig. 6.1e). In the centre of the canyon, the spatial pattern of $\overline{c_{ad}}$ is divided into two regions (see Fig. 6.5d): a region of low mean concentration values (around 0.2) at the rooftop and a region of high values inside the canyon. In particular, inside the canyon, $\overline{c_{ad}}$ is equal to about 0.4 and 0.5 in correspondence of the downwind and upwind tree, respectively. The low $\overline{c_{ad}}$ values at the rooftop are induced by the high turbulent fluctuation intensity due to the interaction between the tree crowns and the external flow, while inside the canyon we found the maximum concentration levels (around 0.5) in correspondence of the upwind tree, where turbulent fluctuations of the velocity reaches the minimum values (see Fig. D.1 in Appendix D). Close to the downwind intersection, the spatial pattern of $\overline{c_{ad}}$ is similar to that in the laterally-closed canyon with θ=30° (Fig. 6.5e): high mean concentration values at the upwind wall (equal to 0.4) and low values in the canyon centre and at the downwind wall (equal to around 0.2). This spatial behaviour is in line with the heterogeneous distribution of the turbulent fluctuation intensity of the velocity (see Figs. 5.7q-r). In particular, the tree crowns enhance the surface roughness promoting turbulence generation and pollutant mixing in correspondence of the upwind tree (y/H=[-0.4,0]), where we detected low mean concentration values. Conversely, the accumulation of the concentration shows up close to the upwind wall, where turbulent fluctuations show their minimum values.

Increasing the wind angle to θ=60°, $\overline{c_{ad}}$ exhibits a three-dimensional spatial pattern within the non-vegetated canyon, as observed with θ=30°. However, in the three cross-sections, the mean scalar concentration is significantly lower than that found with θ=30°, since the plume emitted by the point source is mostly deflected into the intersecting streets, as it passes through the intersection. Close to the upwind intersection, $\overline{c_{ad}}$ (Fig. 6.6a) is 80% higher at the downwind wall than at the upwind wall. However, it is hard to link this accumulation with the fluctuation intensity of the velocity, since its maximum values are close to the downwind wall (see Fig. 5.8c), where there are maximum mean concentration values. In the centre of the canyon (Fig. 6.6b), $\overline{c_{ad}}$ shows the maximum values around 0.02 at ground level and along the upwind wall, since the transversal recirculation transports the pollutant from the downwind

wall to the upwind wall. Close to the downwind intersection, the maximum mean scalar concentration is visible in the downwind half of the cross-section (see Fig. 6.6c), demonstrating that at the downwind edge of the canyon the clockwise transversal recirculation is broken down by the vertical-axis recirculating structure at the canyon edge.

For wind direction θ=60°, the presence of trees almost homogenise the mean scalar concentration along the canyon. In fact, both in the centre of the canyon and close to the downwind intersection, the spatial pattern of $\overline{c_{ad}}$ is similar to that found in the vegetated canyon without intersections (Fig. 6.2f). Notably, in the centre of the canyon (Fig. 6.6d) $\overline{c_{ad}}$ is equal to 0.1 and 0.2 in the shear layers at the rooftop and along the downwind wall, respectively. In this two regions, the interaction between tree crowns and the external flow causes a sharp increase in turbulent fluctuations of the velocity compared to their intensity inside the canyon between the trees (see Figs. D.1g-h in Appendix D). Moving transversely from the downwind to the upwind wall, $\overline{c_{ad}}$ increases from 0.2 to 0.35. A similar spatial pattern shows up close to the downwind intersection (Fig. 6.6e), but with lower $\overline{c_{ad}}$ with respect to the canyon centre, as expected moving further away from the pollutant source. In this cross-section 3, it is evident that the maximum mean concentration value is in the upper upwind corner of the canyon (as observed in the laterally-closed canyon – Fig. 6.2f).

6.3.2 Vertical exchange velocity

For a canyon with intersections, the longitudinal behaviour of the transversally-averaged mean concentration C_{ad} is difficult to be modeled with an exponential function – as made in the laterally-closed canyon – due to the complex flow dynamics within the intersections influencing the pollutant advective transport along the canyon. We evaluated the vertical exchange velocity modeling the canyon as a closed box characterised by a well-mixed concentration C_{vol}, where the mean longitudinal velocity $U_{\parallel,log}$ is not constant along the x-axis, as it is altered by lateral flows at the canyon edges. This control volume was selected between two street intersections, so that assumptions (i)-(v) made for the canyon without intersections (Sect. 6.2.2) also apply in this case. From the mass balance between the longitudinal pollutant advective flux entering and

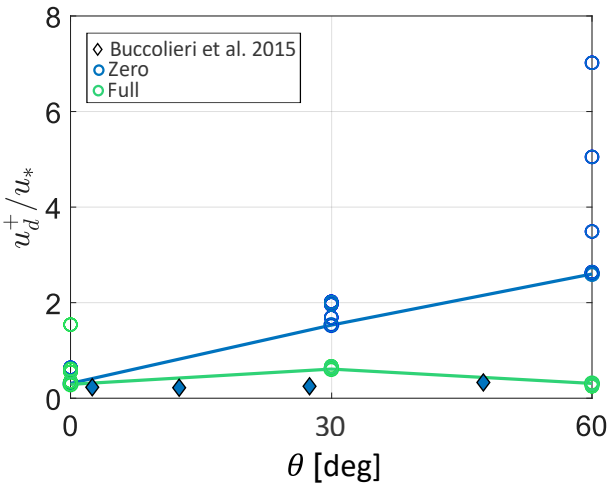


Figure 6.7 Variation of the vertical exchange velocity with θ. Blue and green colors refer to the empty and vegetated canyons, respectively. Different points refer to u_d^+/u_* values calculated by progressively increasing the length Δx of the control volume. The blue diamonds indicate u_d estimated numerically by Buccolieri et al. (2015).

leaving the box and the turbulent pollutant flux at the rooftop, we obtain the expression for the vertical exchange velocity for a street canyon with intersections:

$$u_d^+ = \frac{H[U_{\parallel,log,1}(x)C_{ad}(x) - U_{\parallel,log,3}(x+\Delta x)C_{ad}(x+\Delta x)]}{\Delta x C_{vol}}. \tag{6.6}$$

where u_d^+ is the vertical exchange velocity at the rooftop, $U_{\parallel,log,1}C_{ad}$ and $U_{\parallel,log,2}C_{ad}$ are the longitudinal advective mass flow rate calculated in the cross-sections close to the upwind intersection (cross-section 1) and close to the downwind intersection (cross-section 3), respectively, C_{vol} is the spatial average of the mean scalar concentration over the whole control volume, and H, W, and Δx are the height, width and length of the box. To evaluate u_d^+ in the vegetated canyon, we use $U_{tr,log}(x)$ and C_{ad} calculated with mean concentration and longitudinal velocity data measured in the vegetated canyon. Note that for oblique wind direction, $U_{tr,log,1}(x)$ and $U_{tr,log,2}(x+\Delta x)$ are calculated in the cross-sections in the centre of the canyon (cross-section 2, showed in appendix D) and close to the downwind intersection (cross-section 3), respectively, as the point source is positioned close to the upwind intersection.

In Fig. 6.7, we report the variation of the vertical exchange velocity u_d^+ with the wind direction θ, in the empty and vegetated laterally-opened canyons. In the empty canyon, u_d^+ shows a clear increasing trend with the wind angle: it increases by 80% from θ=0° to θ=30° and by 40% from θ=30° to θ=60°. The large difference in the vertical exchange velocity between θ=0° and θ=30° suggests that the vertical-axis recirculating structures at the canyon edges, developed with the non-parallel wind direction, contribute to the ventilation of the canyon. This is confirmed also by the fact that with oblique wind direction, the vertical exchange velocity values are higher than those in the laterally-closed canyon, while this does not verify with the street axis-parallel wind direction. Moreover, the increasing trend from θ=30° to θ=60° is in line with the longitudinal behaviour of the mean longitudinal velocity U_{log} along the empty canyon with intersections, discussed in Fig. 5.10a. In fact, we found that vertical advective fluxes outward from the canyon are favoured within canyons inclined at 60° to the external flow, while within canyons inclined at 30°, the air entrainment from the external flow into the canyon is favoured.

We compare our experimental u_d^+ values with those obtained, from numerical simulations, by Buccolieri et al. (2015), within a non-vegetated three-dimensional canyon. They found that the vertical exchange velocity increases with the wind angle, but their values are significantly lower than those obtained in our study. For example, for θ=30° the difference is of 80%. This discrepancy arises probably due to the different methods adopted to evaluate the vertical exchange velocity in the two studies. Notably, our model neglects the turbulent component of the mass fluxes, which is instead considered by Buccolieri et al. (2015). Moreover,

In the presence of trees, the increasing behaviour of the vertical exchange velocity u_d^+ with the wind angle is no more detectable, but the u_d^+ values are independent from the wind direction. The u_d^+ has the same values with θ=0° and θ=60° and doubles with θ=30°. Contrary to what observed in the absence of street intersections, the presence of trees causes a decrease in the vertical exchange velocity, mostly with oblique wind direction – with which we found decreases of -60% and -90%, with θ=30° and θ=60°, respectively –. This result is reasonably due to the fact that trees partially hinder the flow structures at the canyon edges, which favour the ventilation efficiency of the canyon.

6.4 Conclusions to Chapter 5

This chapter was aimed at investigating the influence of wind direction, presence of vegetation, and street intersections on the mean scalar concentration field and ventilation efficiency within a reduced-scale street canyon modeled in the wind tunnel. Pollutant emission was simulated with a ground-level point source of ethane. The analysis of the spatial pattern of the mean concentration within the street canyon without intersections revealed that:

- with the street-axis parallel wind direction, the mean scalar concentration within the non-vegetated canyon shows a spatial behaviour symmetrical to the vertical axis, with concentration values that monotonically decrease from ground level to the rooftop. With oblique wind direction, maximum concentration levels were found in the central core of the canyon, while minimum values were found along the downwind wall. In fact, the transversal recirculating structure drives the external air inside the canyon at the downwind wall, transports the scalar concentration towards the upwind wall, and the longitudinal flow component promotes a pollutant accumulation along the longitudinal axis of the canyon.

- At the pedestrian level, mean scalar concentration levels reduce with increasing wind angle θ, thanks to a more efficient wash-out of the canyon with oblique wind direction with respect to the street axis-parallel wind direction.

- The presence of trees partially homogenises the mean scalar concentration in the cross-section, with θ=0°. On the contrary, with oblique wind direction, the scalar concentration accumulates along the upwind wall, due to the tree-induced dampening of turbulent velocity fluctuations around the upwind tree. Nevertheless, the interaction between tree crowns and the external flow enhances the pollutant mixing at the downwind wall, leading to 70% lower mean concentration at the downwind wall with respect to the upwind wall.

The presence of street intersections modifies the spatial behaviour of the mean scalar concentration with respect to the laterally-closed canyon, mostly in

the absence of trees. From the results of the mean concentration measurements within the laterally-opened canyon we understood that:

- the presence of intersections causes a strongly three-dimensional spatial pattern of the mean concentration within the non-vegetated canyon, specially with oblique wind direction (θ={30°,60°}). With θ=30° and θ=60° and close to the upwind intersection, the mean scalar concentration shows its maximum values along the downwind wall, demonstrating the absence of the clock-wise recirculating structure that transports the pollutant towards the upwind wall. Close to the downwind wall, with θ=30° the transversal recirculation is recovered: the mean scalar concentration is low along the downwind wall and high in the central core of the canyon. Conversely, with θ=60°, the maximum concentration shows up close to the downwind wall, suggesting the absence of the transversal transport from the downwind to the upwind wall in the canyon cross-section close to the downwind wall.

- Trees partially homogenise the mean scalar concentration along the wind-aligned canyon with intersections. In particular, the random shape and size of the trees lead to different spatial patterns in the three cross-sections along the canyon – close to the upwind intersection, in the canyon centre, and close to the downwind intersection –, but the difference between maximum and minimum values is less than half that in the empty canyon.

- With oblique wind direction, the mean scalar concentration tends to accumulate at the upwind wall, as observed in the canyon without intersections, both in the cross-sections measured in the canyon centre and close to the downwind wall. We found low concentration at the downwind wall and at the rooftop, both favoured by the efficient pollutant mixing induced by the interaction between the tree crowns and the external flow.

Combining the velocity measurements (presented in Chapters 4 and 5) with the concentrations ones, we estimated the ventilation efficiency of the canyon by calculating the bulk vertical exchange velocity between the canyon and the external boundary layer, varying the canyon geometry, wind direction, and vegetation configuration. Notably, we performed a mass balance between the longitudinal pollutant advective flux entering and leaving a control volume of

the canyon and the vertical mass flux towards the external flow at the rooftop. We found that, in the canyon without intersections, the vertical exchange velocity is independent from the wind direction, regardless of the presence of trees. Trees enhance the vertical exchange velocity by 64% and 23%, with θ=30° and θ=60°, respectively. In the presence of street intersections, the vertical exchange velocity within the empty canyon increases moving from parallel wind direction θ=0° to oblique wind direction, suggesting that the vertical-axis recirculating structures et the canyon edges contribute to the ventilation. Conversely, trees dampen these flow structures, thus the vertical exchange velocity in the vegetated canyon is lower than in the empty canyon, with all wind directions. However, both with and without intersections, when comparing the vertical exchange velocity values among the different wind directions, we should take into account that with θ=30° and θ=60°, the average concentration within the canyon does not show the spatial distribution typical of a pollutant emission at ground level (i.e. the maximum concentration is not at ground level). This is not true in the wind-aligned canyon. This experimental issue (which verifies both with and without trees) could affects our results, since the vertical exchange velocity is sensitive to the position of the pollutant source. In order to avoid this issue and improve the estimate of the ventilation efficiency within a street canyon, another experimental campaign is planned, simulating pollutant emissions with a ground level linear source, whose length occupies the whole reference street canyon.

Chapter 7

Conclusions and perspectives

This thesis presents the results of three experimental campaigns performed in the atmospheric wind tunnel at the École Centrale de Lyon, aimed at investigating the aerodynamic influence of trees on the turbulent flow and pollutant concentration fields within a street canyon, subject to a neutrally-stratified boundary layer. The first experimental campaign was aimed at performing concentration, velocity, and simultaneous concentration-velocity measurements inside a canyon oriented perpendicular to the external wind, with different tree densities. A second experimental campaign of flow velocity measurements was carried out to investigate the influence of wind direction θ, street geometry, presence of trees, and street intersections on the turbulent flow field within a street canyon. The effects of these parameters on the mean concentration field were investigated performing a third experimental campaign of scalar concentration measurements.

From the experimental results, we draw the following conclusions about the aerodynamic effects of vegetation on street canyon ventilation:

- within a large canyon (H/W_w=0.5) perpendicular to the external flow (θ=90°), trees inhibit the turbulent kinetic energy and vertical turbulent mass fluxes inside the canyon, with a consequent lower pollutant mixing with respect to an empty canyon. Indeed, the presence of trees induces a transition from the nearly two-dimensional spatial patterns of the mean and turbulent concentration fields (characteristic of the non-vegetated canyon), to strongly three-dimensional fields, both inside the canyon and

at the rooftop. Moreover, trees partially hinder the upward mean flow and mean mass fluxes close to the upwind wall. In fact, at the rooftop, we found that positive values of $\overline{w}$ and $\bar{w}\bar{c}$ at the upwind wall occur only between adjacent trees – with a spatial periodicity which depends on the tree density –, whilst they are equal to zero in correspondence of trees.

- With the street axis-parallel wind direction (θ=0°), local values of the mean longitudinal velocity between tree crowns decrease by around 80% with respect to the non-vegetated case, both within square and large canyons. This decrease in the mean longitudinal velocity was also evident within a square canyon with oblique wind direction (θ=30° and θ=60°), but in this case trees hinder also the mean transversal flow at ground level, breaking up the transversal recirculation.

- Concerning flow velocity fluctuations, with θ=0°, the interaction between the tree crowns and the external boundary layer enhances longitudinal and transversal velocity turbulent fluctuations by around 30% at the rooftop of the square canyon, with respect to the non-vegetated configuration. Conversely, velocity turbulent fluctuations are dampened inside the canyon, in correspondence of tree crowns. Inside a large canyon (H/W_w=0.5) aligned with the external wind, a vegetation-free corridor between the rows of trees leads to 20% increase in longitudinal and transversal velocity fluctuations in the centre of the vegetated canyon with respect to the empty one. This result suggests more efficient pollutant mixing compared to the large wind-aligned canyon without trees and also compared to the vegetated canyon perpendicular to the external wind. With oblique wind direction (θ={30°,60°}) and aspect ratio H/W=1, a tree-induced increase in turbulent fluctuations with respect to the empty canyon (up to 40%) verifies both at the rooftop and inside the canyon, along the downwind wall. As a consequence, an asymmetric spatial distribution of turbulent velocity fluctuations arises inside the canyon, that leads to an accumulation of pollutant concentration along the upwind wall, where turbulent fluctuations are dampened by the upwind tree, and almost zero mean scalar concentration close to the downwind wall, where high turbulent fluctuations promotes pollutant mixing.

- Rows of trees characterised by intersecting crowns both in the longitudinal and transversal directions hinder the formation of large-scale turbulent structures within a canyon, regardless of the wind direction. Indeed, the spectra of the longitudinal and transversal velocity in the vegetated square canyon result shifted towards higher frequencies (smaller length scales) with respect to those calculated in the empty square canyon. On the contrary, in the vegetation-free corridor in the centre of a large canyon (both with θ=0° and θ=90°), trees affect only the energy content of large-scale structures: the energy associated to low frequencies progressively decreases with increasing vegetation density.

The huge amount of experimental data collected during this thesis provides a contribution to understand the effects of trees on the turbulent flow and concentration fields within an urban canyon, with different wind directions and street geometries. These results are useful in the design of urban greening strategies. Indeed, even though vegetation improves the liveability of cities, in some cases it may deteriorate the air quality within urban streets. For example, high density vegetation with intersecting crowns hinders the advective flow and dampens turbulent kinetic energy within street canyons. As a consequence, the transport and mixing of pollutants are less efficient than those in a non-vegetated canyon. With orthogonal and oblique wind directions, we observed an accumulation of concentration close to the upwind wall, while with the parallel wind direction we found the maximum scalar concentration at the bottom of the canyon cross-section, i.e., close to the pedestrian level. Conversely, within a wind-aligned large canyon, rows of trees along the lateral walls create a vegetation-free corridor in the canyon centre with high surface roughness, that promotes turbulence generation and pollutant mixing within the canyon.

Furthermore, the experimental data collected in this thesis are useful to validate analytical models and numerical simulations, aimed at simulating flow and dispersion in urban-like geometries in the presence of vegetation. These tools are useful nowadays to help decision makers to face the problem of urban air pollution. In fact, nowadays, cities represent the fulcrum of economic exercises and social relations, thus half of the World's population leaves in cities and this percentage is expected to grows in the future. For this reason, the improvement of the quality of life in cities, the enhancement of green areas, and

the reduction of air pollution are included in one of the sustainable development goals of the United Nations (SDG11). To share our concentration, velocity, and turbulent mass fluxes data within the reduced-scale canyon, we are currently creating an online dataset.

However, our experimental facility presented some limitations. It was not possible to characterise the vertical velocity field within the square canyon (H/W=1), due to the difficulty of introducing the LDA instrument coupled with a mirror (necessary for measuring the vertical velocity component, w) into vegetated canyons. This limitation prevented us also to measure vertical turbulent mass fluxes with the coupled system LDA-FID, within the square canyon. Moreover, the introduction of a pollutant point source within the canyon (with non orthogonal wind directions, i.e., with θ=$\{0°,30°,60°\}$) did not produce concentration fields typical of a ground-level source, with all the wind directions considered. This prevented us to accurately analyse the effect of wind direction on the vertical exchange velocity at the rooftop of the canyons with and without trees. For this reason, other experiments are planned, using a linear source of the same length as the canyon, to confirm the vertical exchange velocity results, presented in Chapter 6. A future development of this thesis will be to extend the analysis of the flow field and pollutant dispersion in urban geometries from the scale of the single street to the scale of an entire urban district. To this end, concentration and velocity measurements will be carried out within several streets belonging to regular street networks or to neighborhoods with more complex geometries. For example, we are planning an experimental campaign of concentration and flow velocity measurements, within a realistic reduced-scale neighborhood of Lyon, reproduced in the wind tunnel.

Bibliography

Abhijith, K., Kumar, P., Gallagher, J., McNabola, A., Baldauf, R., Pilla, F., Broderick, B., Di Sabatino, S., and Pulvirenti, B. (2017). Air pollution abatement performances of green infrastructure in open road and built-up street canyon environments – A review. *Atmospheric Environment*, 162:71–86.

Aboelata, A. and Sodoudi, S. (2020). Evaluating the effect of trees on UHI mitigation and reduction of energy usage in different built up areas in Cairo. *Building and Environment*, 168:106–490.

Allegrini, J., Dorer, V., and Carmeliet, J. (2013). Wind tunnel measurements of buoyant flows in street canyons. *Building and Environment*, 59:315–326.

Balogun, A. A., Tomlin, A. S., Wood, C. R., Barlow, J. F., Belcher, S. E., Smalley, R. J., Lingard, J. J., Arnold, S. J., Dobre, A., Robins, A. G., et al. (2010). In-street wind direction variability in the vicinity of a busy intersection in central London. *Boundary-layer meteorology*, 136:489–513.

Bao, S., Feng, Z., and Cao, S.-J. (2025). Numerical investigations on urban roadside vegetation for efficient mitigation of airborne ultra-fine particles pollution: Model development, validation and implementation. *Urban Climate*, 61:102377.

Blackman, K., Perret, L., and Savory, E. (2015). Effect of upstream flow regime on street canyon flow mean turbulence statistics. *Environmental Fluid Mechanics*, 15(4):823–849.

Blackman, K., Perret, L., and Savory, E. (2018). Effects of the upstream-flow regime and canyon aspect ratio on non-linear interactions between a street-canyon flow and the overlying boundary layer. *Boundary-Layer Meteorology*, 169:537–558.

Buccolieri, R., Gromke, C., Di Sabatino, S., and Ruck, B. (2009). Aerodynamic effects of trees on pollutant concentration in street canyons. *Science of the Total Environment*, 407(19):5247–5256.

Buccolieri, R., Jeanjean, A. P., Gatto, E., and Leigh, R. J. (2018). The impact of trees on street ventilation, nox and pm2. 5 concentrations across heights

in marylebone rd street canyon, central london. *Sustainable Cities and Society*, 41:227–241.

Buccolieri, R., Salim, S. M., Leo, L. S., Di Sabatino, S., Chan, A., Ielpo, P., de Gennaro, G., and Gromke, C. (2011). Analysis of local scale tree–atmosphere interaction on pollutant concentration in idealized street canyons and application to a real urban junction. *Atmospheric Environment*, 45(9):1702–1713.

Buccolieri, R., Salizzoni, P., Soulhac, L., Garbero, V., and Di Sabatino, S. (2015). The breathability of compact cities. *Urban Climate*, 13:73–93.

Cancelli, C., Boffadossi, M., and Salizzoni, P. (2006). *Fluidodinamica ambientale: Turbolenza e dispersione*. Otto Editore.

Carlo, O. S., Fellini, S., Palusci, O., Marro, M., Salizzoni, P., and Buccolieri, R. (2024). Influence of obstacles on urban canyon ventilation and air pollutant concentration: An experimental assessment. *Building and Environment*, 250:111–143.

Carpentieri, M. and Robins, A. G. (2010). Tracer flux balance at an urban canyon intersection. *Boundary-Layer Meteorology*, 135:229–242.

Carpentieri, M., Robins, A. G., and Baldi, S. (2009). Three-dimensional mapping of air flow at an urban canyon intersection. *Boundary-layer meteorology*, 133:277–296.

Cassiani, M., Bertagni, M. B., Marro, M., and Salizzoni, P. (2020). Concentration fluctuations from localized atmospheric releases. *Boundary-Layer Meteorology*, 177:461–510.

Clemente, M., Pignatti, G., Degaetano, M., and Corona, P. (2025). A "street tree" master plan for the strategic management of linear reforestation and urban landscape enhancement in rome, italy. *Land*, 14(3):606.

Corona, P., Clemente, M., Alivernini, A., Degaetano, M., Di Stefano, V., Ferrara, C., Mattioli, W., Menta, F., Presutti Saba, E., Pontuale, G., et al. (2024). Analisi e strategie per la riqualificazione delle alberature stradali di roma capitale.

Del Ponte, A. V., Fellini, S., Marro, M., Soulhac, L., Ridolfi, L., and Salizzoni, P. (2025). The turbulent flow within a wind-aligned street canyon with trees: an experimental study: Avd ponte et al. *Boundary-Layer Meteorology*, 191(6):21.

Del Ponte, A. V., Fellini, S., Marro, M., van Reeuwijk, M., Ridolfi, L., and Salizzoni, P. (2024). Influence of street trees on turbulent fluctuations and transport processes in an urban canyon: a wind tunnel study. *Boundary-Layer Meteorology*, 190(2):6.

Di Bernardino, A., Monti, P., Leuzzi, G., and Querzoli, G. (2015). Water-channel study of flow and turbulence past a two-dimensional array of obstacles. *Boundary-Layer Meteorology*, 155(1):73–85.

Di Bernardino, A., Monti, P., Leuzzi, G., and Querzoli, G. (2018). Pollutant fluxes in two-dimensional street canyons. *Urban climate*, 24:80–93.

Diener, A. and Mudu, P. (2021). How can vegetation protect us from air pollution? A critical review on green spaces' mitigation abilities for air-borne particles from a public health perspective – with implications for urban planning. *Science of the Total Environment*, 796:148605.

Dobre, A., Arnold, S., Smalley, R., Boddy, J., Barlow, J., Tomlin, A., and Belcher, S. (2005). Flow field measurements in the proximity of an urban intersection in london, UK. *Atmospheric Environment*, 39(26):4647–4657.

EEA (2020). *Healthy environment, healthy lives: how the environment influences health and well-being in Europe*. Europian Environment Agency.

EEA (2024). *Air pollution in Europe: 2024 reporting status under the National Emission reduction Commitments Directive*. Europian Environment Agency.

Fellini, S., Marro, M., Del Ponte, A. V., Barulli, M., Soulhac, L., Ridolfi, L., and Salizzoni, P. (2022). High resolution wind-tunnel investigation about the effect of street trees on pollutant concentration and street canyon ventilation. *Building and Environment*, 226:109763.

Fellini, S., Ridolfi, L., and Salizzoni, P. (2020). Street canyon ventilation: Combined effect of cross-section geometry and wall heating. *Quarterly Journal of the Royal Meteorological Society*, 146(730):2347–2367.

Fellini, S., Salizzoni, P., and Ridolfi, L. (2021). Vulnerability of cities to toxic airborne releases is written in their topology. *Scientific Reports*, 11(1):23029.

Ferrini, F. and Fini, A. (2011). Sustainable management techniques for trees in the urban areas. *Journal of Biodiversity and ecological sciences*, 1(1):1–20.

Ferrini, F., Fini, A., Mori, J., and Gori, A. (2020). Role of vegetation as a mitigating factor in the urban context. *Sustainability*, 12(10):4247.

Finn, D., Clawson, K. L., Carter, R. G., Rich, J. D., Biltoft, C., and Leach, M. (2010). Analysis of urban atmosphere plume concentration fluctuations. *Boundary-layer meteorology*, 136:431–456.

Finnigan, J. (2000). Turbulence in plant canopies. *Annual review of fluid mechanics*, 32(1):519–571.

Fischer, H. B., List, J. E., Koh, C. R., Imberger, J., and Brooks, N. H. (1979). *Mixing in inland and coastal waters*. Accademic Press.

Fuka, V., Xie, Z.-T., Castro, I. P., Hayden, P., Carpentieri, M., and Robins, A. G. (2018). Scalar fluxes near a tall building in an aligned array of rectangular buildings. *Boundary-layer meteorology*, 167:53–76.

Garbero, V., Salizzoni, P., and Soulhac, L. (2010). Experimental study of pollutant dispersion within a network of streets. *Boundary-layer meteorology*, 136:457–487.

Grilo, F., Pinho, P., Aleixo, C., Catita, C., Silva, P., Lopes, N., Freitas, C., Santos-Reis, M., McPhearson, T., and Branquinho, C. (2020). Using green to cool the grey: Modelling the cooling effect of green spaces with a high spatial resolution. *Science of the Total Environment*, 724:138182.

Grimmond, C. and Oke, T. R. (1999). Aerodynamic properties of urban areas derived from analysis of surface form. *Journal of Applied Meteorology and Climatology*, 38(9):1262–1292.

Gromke, C. (2011). A vegetation modeling concept for building and environmental aerodynamics wind tunnel tests and its application in pollutant dispersion studies. *Environmental pollution*, 159(8-9):2094–2099.

Gromke, C., Buccolieri, R., Di Sabatino, S., and Ruck, B. (2008). Dispersion study in a street canyon with tree planting by means of wind tunnel and numerical investigations – evaluation of CFD data with experimental data. *Atmospheric Environment*, 42(37):8640 – 8650.

Gromke, C., Jamarkattel, N., and Ruck, B. (2016). Influence of roadside hedgerows on air quality in urban street canyons. *Atmospheric environment*, 139:75–86.

Gromke, C. and Ruck, B. (2007). Influence of trees on the dispersion of pollutants in an urban street canyon – experimental investigation of the flow and concentration field. *Atmospheric Environment*, 41(16):3287–3302.

Gromke, C. and Ruck, B. (2009). On the impact of trees on dispersion processes of traffic emissions in street canyons. *Boundary-Layer Meteorology*, 131(1):19–34.

Gromke, C. and Ruck, B. (2012). Pollutant concentrations in street canyons of different aspect ratio with avenues of trees for various wind directions. *Boundary-Layer Meteorology*, 144(1):41–64.

Grylls, T. and van Reeuwijk, M. (2021). Tree model with drag, transpiration, shading and deposition: Identification of cooling regimes and large-eddy simulation. *Agricultural and Forest Meteorology*, 298:108288.

Grylls, T. and van Reeuwijk, M. (2022). How trees affect urban air quality: It depends on the source. *Atmospheric Environment*, 290:119275.

Guan, D., Zhang, Y., and Zhu, T. (2003). A wind-tunnel study of windbreak drag. *Agricultural and forest meteorology*, 118(1-2):75–84.

HEI (2024). *State of Global Air 2024. Special report.* Health Effects Institute.

Hinze, J. (1967). Secondary currents in wall turbulence. *The Physics of Fluids*, 10(9):122–125.

Hsu, K.-W. and Chao, J.-C. (2021). Study on the value model of urban green infrastructure development—a case study of the central district of taichung city. *Sustainability*, 13(13):7402.

Huang, Y.-D., Hou, R.-W., Liu, Z.-Y., Song, Y., Cui, P.-Y., Kim, C.-N., et al. (2019). Effects of wind direction on the airflow and pollutant dispersion inside a long street canyon. *Aerosol and Air Quality Research*, 19(5):1152–1171.

Jaroslawski, T., Savory, E., and Perret, L. (2020). Roof-level large-and small-scale coherent structures in a street canyon flow. *Environmental Fluid Mechanics*, 20:739–763.

Jeanjean, A. P., Buccolieri, R., Eddy, J., Monks, P. S., and Leigh, R. J. (2017). Air quality affected by trees in real street canyons: The case of Marylebone neighbourhood in central london. *Urban Forestry & Urban Greening*, 22:41–53.

Jeanjean, A. P., Hinchliffe, G., McMullan, W., Monks, P. S., and Leigh, R. J. (2015). A CFD study on the effectiveness of trees to disperse road traffic emissions at a city scale. *Atmospheric Environment*, 120:1–14.

Ji, L., Shu, C., Gaur, A., Wang, L., and Lacasse, M. (2024). A state-of-the-art review of studies on urban green infrastructure for thermal resilient communities. *Building and Environment*, 257:111524.

Kaimal, J. C., Wyngaard, J., Izumi, Y., and Coté, O. (1972). Spectral characteristics of surface-layer turbulence. *Quarterly Journal of the Royal Meteorological Society*, 98(417):563–589.

Kottegoda, N. T. and Rosso, R. (1997). *Applied statistics for civil and environmental engineers.* McGraw-Hill.

Krogstadt, P.-Å. and Antonia, R. (1999). Surface roughness effects in turbulent boundary layers. *Experiments in fluids*, 27(5):450–460.

Kukačka, L., Nosek, Š., Kellnerová, R., Jurčáková, K., and Jaňour, Z. (2012). Wind tunnel measurement of turbulent and advective scalar fluxes: a case study on intersection ventilation. *The Scientific World Journal*, 2012:1–13.

Li, J. and Bilger, R. (1996). The diffusion of conserved and reactive scalars behind line sources in homogeneous turbulence. *Journal of Fluid Mechanics*, 318:339–372.

Li, Z., Zhang, H., Juan, Y.-H., Lee, Y.-T., Wen, C.-Y., and Yang, A.-S. (2023). Effects of urban tree planting on thermal comfort and air quality in the street canyon in a subtropical climate. *Sustainable Cities and Society*, 91:104334.

Li, Z., Zhang, H., Wen, C.-Y., Yang, A.-S., and Juan, Y.-H. (2021). The effects of lateral entrainment on pollutant dispersion inside a street canyon and the corresponding optimal urban design strategies. *Building and Environment*, 195:107740.

Lin, Y., Hang, J., Yang, H., Chen, L., Chen, G., Ling, H., Sandberg, M., Claesson, L., and Lam, C. K. C. (2021). Investigation of the reynolds number independence of cavity flow in 2D street canyons by wind tunnel experiments and numerical simulations. *Building and Environment*, 201:107965.

Linden, J., Gustafsson, M., Uddling, J., Watne, Å., and Pleijel, H. (2023). Air pollution removal through deposition on urban vegetation: The importance of vegetation characteristics. *Urban Forestry & Urban Greening*, 81:127–843.

Liu, C.-H., Leung, D. Y., and Barth, M. C. (2005). On the prediction of air and pollutant exchange rates in street canyons of different aspect ratios using large-eddy simulation. *Atmospheric Environment*, 39(9):1567–1574.

Maison, A., Flageul, C., Carissimo, B., Wang, Y., Tuzet, A., and Sartelet, K. (2022). Parameterizing the aerodynamic effect of trees in street canyons for the street network model MUNICH using the CFD model Code_Saturne. *Atmospheric Chemistry and Physics*, 22(14):9369–9388.

Majumdar, D., Vita, G., Ramponi, R., Glover, N., and van Reeuwijk, M. (2025). The drag length is key to quantifying tree canopy drag. *Journal of Wind Engineering and Industrial Aerodynamics*, 261:106084.

Manickathan, L., Defraeye, T., Allegrini, J., Derome, D., and Carmeliet, J. (2018). Comparative study of flow field and drag coefficient of model and small natural trees in a wind tunnel. *Urban Forestry & Urban Greening*, 35:230–239.

Marrazzo, G. and Raimondi, A. (2025). The role of urban trees as nature-based solutions for stormwater runoff control. *Urban Forestry & Urban Greening*, 103:128598.

Marro, M., Gamel, H., Méjean, P., Correia, H., Soulhac, L., and Salizzoni, P. (2020). High-frequency simultaneous measurements of velocity and concentration within turbulent flows in wind-tunnel experiments. *Experiments in Fluids*, 61(12):1–13.

Marucci, D. and Carpentieri, M. (2019). Effect of local and upwind stratification on flow and dispersion inside and above a bi-dimensional street canyon. *Building and Environment*, 156:74–88.

Merlier, L., Jacob, J., and Sagaut, P. (2018). Lattice-Boltzmann Large-Eddy Simulation of pollutant dispersion in street canyons including tree planting effects. *Atmospheric Environment*, 195:89–103.

Montgomery, D. C., Peck, E. A., and Vining, G. G. (2021). *Introduction to linear regression analysis*. John Wiley & Sons.

Moonen, P., Gromke, C., and Dorer, V. (2013). Performance assessment of large eddy simulation (LES) for modeling dispersion in an urban street canyon with tree planting. *Atmospheric environment*, 75:66–76.

Nakamura, Y. and Oke, T. R. (1988). Wind, temperature and stability conditions in an east-west oriented urban canyon. *Atmospheric Environment (1967)*, 22(12):2691–2700.

Neophytou, M.-A., Markides, C., and Fokaides, P. (2014). An experimental study of the flow through and over two-dimensional rectangular roughness elements: Deductions for urban boundary layer parameterizations and exchange processes. *Physics of Fluids*, 26(8):086603.

Nironi, C., Salizzoni, P., Marro, M., Mejean, P., Grosjean, N., and Soulhac, L. (2015). Dispersion of a passive scalar fluctuating plume in a turbulent boundary layer. Part I: Velocity and concentration measurements. *Boundary-layer meteorology*, 156(3):415–446.

Nowak, D. J. and Crane, D. E. (2002). Carbon storage and sequestration by urban trees in the USA. *Environmental pollution*, 116(3):381–389.

Oettl, D. and Ferrero, E. (2017). A simple model to assess odour hours for regulatory purposes. *Atmospheric environment*, 155:162–173.

Oke, T. R., Mills, G., Christen, A., and Voogt, J. A. (2017). *Urban climates*. Cambridge University Press.

Oliveira, S., Andrade, H., and Vaz, T. (2011). The cooling effect of green spaces as a contribution to the mitigation of urban heat: A case study in Lisbon. *Building and environment*, 46(11):2186–2194.

Orsi, M., Soulhac, L., Feraco, F., Marro, M., Rosenberg, D., Marino, R., Boffadossi, M., and Salizzoni, P. (2021). Scalar mixing in homogeneous isotropic turbulence: A numerical study. *Physical Review Fluids*, 6(3):034502.

Pastore, M. C. et al. (2025). Planning, planting, and maintaining new urban forests in the metropolitan area of milano case study of forestami. *SPOOL*, 12(1):113–126.

Peltola, O., Aslan, T., Aurela, M., Lohila, A., Mammarella, I., Papale, D., Thomas, C. K., Vesala, T., and Laurila, T. (2025). Towards an enhanced metric for detecting vertical flow decoupling in eddy covariance flux observations. *Agricultural and Forest Meteorology*, 362:110326.

Perret, L., Basley, J., Mathis, R., and Piquet, T. (2019). The atmospheric boundary layer over urban-like terrain: influence of the plan density on roughness sublayer dynamics. *Boundary-Layer Meteorology*, 170(2):205–234.

Pietri, L., Petroff, A., Amielh, M., and Anselmet, F. (2009). Turbulence characteristics within sparse and dense canopies. *Environmental fluid mechanics*, 9(3):297–320.

Poggi, D. and Katul, G. (2007a). Turbulent flows on forested hilly terrain: the recirculation region. *Quarterly Journal of the Royal Meteorological Society*, 133(625):1027–1039.

Poggi, D., Katul, G., and Albertson, J. (2006). Scalar dispersion within a model canopy: Measurements and three-dimensional lagrangian models. *Advances in Water Resources*, 29(2):326–335.

Poggi, D. and Katul, G. G. (2007b). An experimental investigation of the mean momentum budget inside dense canopies on narrow gentle hilly terrain. *Agricultural and forest meteorology*, 144(1-2):1–13.

Poggi, D., Porporato, A., Ridolfi, L., Albertson, J., and Katul, G. (2004). The effect of vegetation density on canopy sub-layer turbulence. *Boundary-Layer Meteorology*, 111:565–587.

Raupach, M., Coppin, P., and Legg, B. (1986). Experiments on scalar dispersion within a model plant canopy part i: The turbulence structure. *Boundary-Layer Meteorology*, 35:21–52.

Raupach, M. R., Antonia, R. A., and Rajagopalan, S. (1991). Rough-wall turbulent boundary layers. *Applied Mechanics Reviews*, 44(1):1–25.

Raupach, M. R., Finnigan, J. J., and Brunet, Y. (1996). Coherent eddies and turbulence in vegetation canopies: the mixing-layer analogy. *Boundary-Layer Meteorology*, pages 351–382.

Salem, N. B., Garbero, V., Salizzoni, P., Lamaison, G., and Soulhac, L. (2015). Modelling pollutant dispersion in a street network. *Boundary-Layer Meteorology*, 155:157–187.

Salizzoni, P., Marro, M., Soulhac, L., Grosjean, N., and Perkins, R. J. (2011). Turbulent transfer between street canyons and the overlying atmospheric boundary layer. *Boundary-layer meteorology*, 141(3):393–414.

Salizzoni, P., Soulhac, L., and Mejean, P. (2009). Street canyon ventilation and atmospheric turbulence. *Atmospheric Environment*, 43(32):5056–5067.

Salizzoni, P., Soulhac, L., Mejean, P., and Perkins, R. J. (2008). Influence of a two-scale surface roughness on a neutral turbulent boundary layer. *Boundary-layer meteorology*, 127(1):97–110.

Sawford, B. and Stapountzis, H. (1986). Concentration fluctuations according to fluctuating plume models in one and two dimensions. *Boundary-layer meteorology*, 37(1-2):89–105.

Snyder, W. H. (1972). Similarity criteria for the application of fluid models to the study of air pollution meteorology. *Boundary-Layer Meteorology*, 3(1):113–134.

Snyder, W. H. and Castro, I. P. (2002). The critical Reynolds number for rough-wall boundary layers. *Journal of wind engineering and industrial aerodynamics*, 90(1):41–54.

Soulhac, L., Garbero, V., Salizzoni, P., Mejean, P., and Perkins, R. (2009). Flow and dispersion in street intersections. *Atmospheric Environment*, 43(18):2981–2996.

Soulhac, L., Perkins, R. J., and Salizzoni, P. (2008). Flow in a street canyon for any external wind direction. *Boundary-Layer Meteorology*, 126(3):365–388.

Soulhac, L. and Salizzoni, P. (2010). Dispersion in a street canyon for a wind direction parallel to the street axis. *Journal of Wind Engineering and Industrial Aerodynamics*, 98(12):903–910.

Soulhac, L., Salizzoni, P., Cierco, F.-X., and Perkins, R. (2011). The model SIRANE for atmospheric urban pollutant dispersion; part I, presentation of the model. *Atmospheric environment*, 45(39):7379–7395.

Soulhac, L., Salizzoni, P., Mejean, P., and Perkins, R. J. (2013). Parametric laws to model urban pollutant dispersion with a street network approach. *Atmospheric Environment*, 67:229–241.

Stapountzis, H., Sawford, B., Hunt, J., and Britter, R. (1986). Structure of the temperature field downwind of a line source in grid turbulence. *Journal of Fluid Mechanics*, 165:401–424.

Tennekes, H. and Lumley, J. L. (1972). *A first course in turbulence*. MIT press.

Tomson, M., Kumar, P., Barwise, Y., Perez, P., Forehead, H., French, K., Morawska, L., and Watts, J. F. (2021). Green infrastructure for air quality improvement in street canyons. *Environment international*, 146:106–288.

Tritton, D. J. (2012). *Physical fluid dynamics*. Springer Science & Business Media.

Van Renterghem, T., Forssén, J., Attenborough, K., Jean, P., Defrance, J., Hornikx, M., and Kang, J. (2015). Using natural means to reduce surface transport noise during propagation outdoors. *Applied Acoustics*, 92:86–101.

Wang, Y., Ni, Z., Chen, S., and Xia, B. (2019). Microclimate regulation and energy saving potential from different urban green infrastructures in a subtropical city. *Journal of cleaner production*, 226:913–927.

WHO (2023). *Improving the capacity of countries to report on air quality in cities: Users' guide to the repository of United Nations tools*. World Health Organization.

Yassin, M. (2008). Probability characteristics of concentration fluctuations in plume dispersal. *Journal of Engineering Sciences*, 36(1):115–130.

Zhang, L., Zhang, Z., Feng, C., Tian, M., and Gao, Y. (2021). Impact of various vegetation configurations on traffic fine particle pollutants in a street canyon for different wind regimes. *Science of the Total Environment*, 789:147–960.

Zhao, N., Prieur, J.-F., Liu, Y., Kneeshaw, D., Lapointe, E. M., Paquette, A., Zinszer, K., Dupras, J., Villeneuve, P. J., Rainham, D. G., et al. (2021). Tree characteristics and environmental noise in complex urban settings–a case study from montreal, canada. *Environmental Research*, 202:111887.

Zhao, Y., Chew, L. W., Fan, Y., Gromke, C., Hang, J., Yu, Y., Ricci, A., Zhang, Y., Xue, Y., Fellini, S., et al. (2023a). Fluid Tunnel Research for Challenges of Urban Climate. *arXiv preprint arXiv:2301.03001*.

Zhao, Y., Li, H., Bardhan, R., Kubilay, A., Li, Q., and Carmeliet, J. (2023b). The time-evolving impact of tree size on nighttime street canyon microclimate: Wind tunnel modeling of aerodynamic effects and heat removal. *Urban Climate*, 49:101–528.

Zheng, S., He, C., Guldmann, J.-M., Xu, H., and Liu, X. (2023). Heat mitigation benefits of urban trees: a review of mechanisms, modeling, validation and simulation. *Forests*, 14(12):2280.

Zölch, T., Henze, L., Keilholz, P., and Pauleit, S. (2017). Regulating urban surface runoff through nature-based solutions – an assessment at the micro-scale. *Environmental research*, 157:135–144.

Appendix A

Expressions of the third and fourth moments of the gamma, lognormal, and Weibull distributions

The skewness and kurtosis of the gamma, lognormal and Weibull 2p distributions are reported as a function of the only parameter C_v:

1. gamma distribution:

$$\begin{aligned} S_k(\vartheta) &= \frac{2}{\sqrt{\vartheta}} \\ K_u(\vartheta) &= \frac{6}{\vartheta} + 3 \end{aligned} \tag{A.1}$$

   where ϑ is defined as $\vartheta = C_v^{-2}$.

2. lognormal distribution:

$$\begin{aligned} S_k(C_v) &= [\exp(\ln(1 + C_v) + 2]\sqrt{\exp[\ln(1 + C_v^2)] - 1} \\ K_u(C_v) &= \exp[4\ln(1 + C_v^2)] + 2\exp[3\ln(1 + C_v^2)] + 3\exp[2\ln(1 + C_v^2)] - 3 \end{aligned} \tag{A.2}$$

3. Weibull 2p distribution:

$$\begin{aligned} S_k(C_v) &= \Gamma\Big(1+\frac{3}{C_v^{-1.086}}\Big)C_v^{-3}a_w^3 - 3C_v^{-1} - C_v^{-3} \\ K_u(C_v) &= \Gamma\Big(1+\frac{4}{C_v^{-1.086}}\Big)C_v^{-4}a_w^4 - 4S_kC_v^{-1} - 6C_v^{-2} - C_v^{-4}. \end{aligned} \tag{A.3}$$

where

$$a_w = \frac{1}{\Gamma(1+C_v^{1.086})} \tag{A.4}$$

Appendix B

Longitudinal homogeneity in the wind-aligned square street canyon

In Figs. B.1, we report longitudinal profiles at y/H={-0.25,0} of the mean longitudinal velocity $\overline{u}$ and of the standard deviation of the longitudinal (σ_u) and transversal (σ_v) velocity, normalised by the free-stream velocity (U_∞).

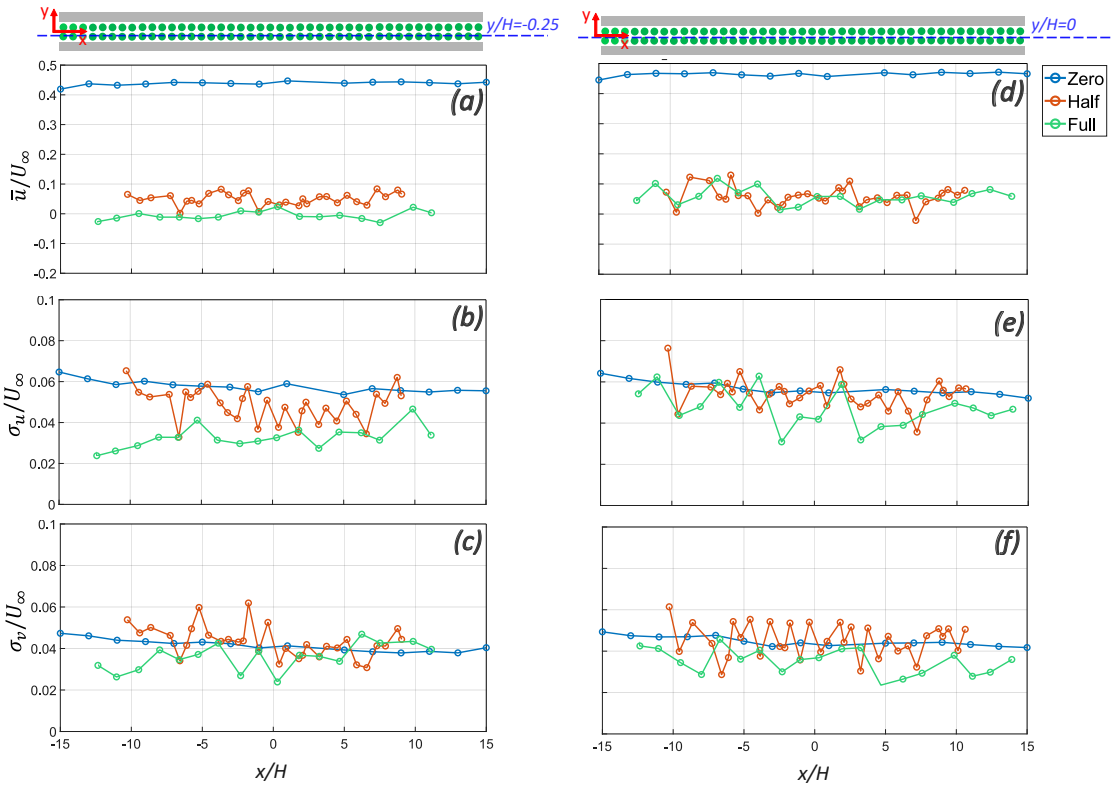


Figure B.1 Longitudinal profiles, measured at y/H=-0.25 (a-c) and y/H=-0 (d-f), of the mean longitudinal velocity (a,d) and standard deviations of the longitudinal (b,e) and transversal (c,f) velocities. The Zero (blue), Half (orange), and Full (green) configurations are shown. The green circles indicate the position of the trees, spaced 7 cm apart. The position of the trees in the Half configuration can be deduced alternately removing half circles symmetrically with respect to the center. The blue dashed line reported in the sketch indicates the position with respect to the tree lines of the longitudinal profile.

Appendix C

Turbulent flow field within a wind-aligned square canyon in the Half configuration

In Fig. C.1, we report the $\overline{u}/U_\infty$, $\overline{v}/U_\infty$, σ_u/U_∞, σ_v/U_∞, the skewness of u and v and the kurtosis of u and v, in the street canyon with trees 14 cm spaced apart (Half configuration).

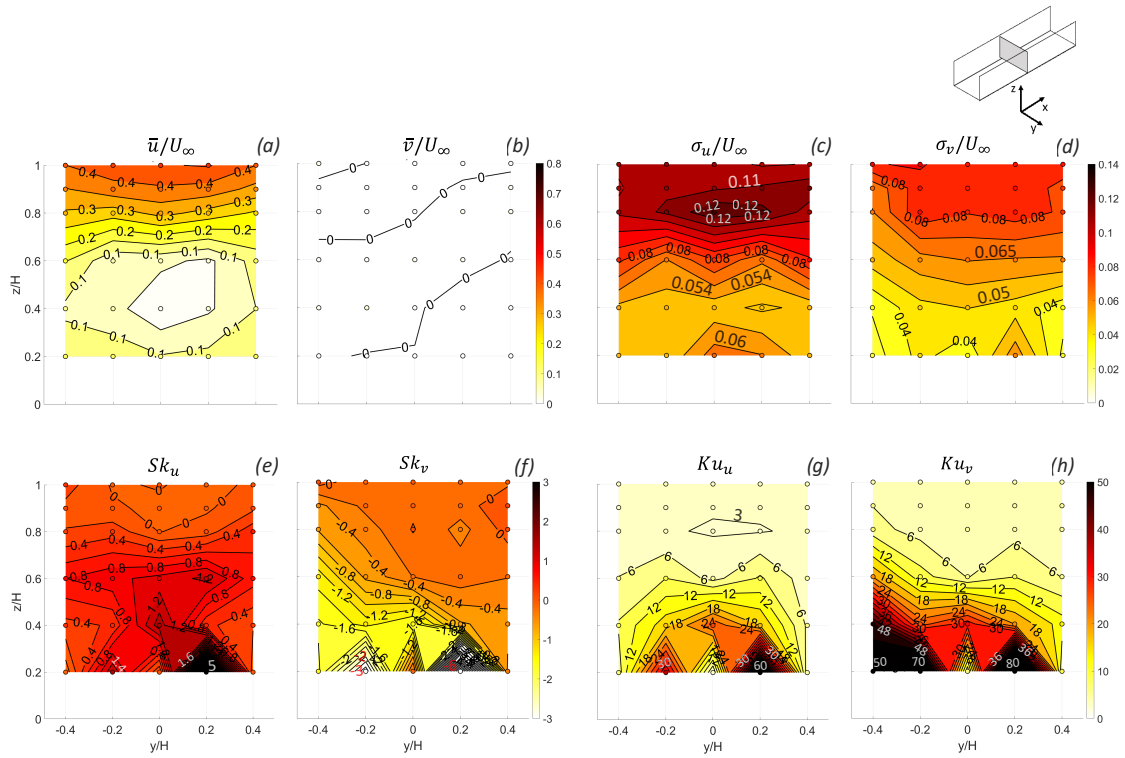


Figure C.1 Transversal behaviour, in the large canyon and in the Half configuration, of the mean longitudinal velocity (a), mean transversal velocity (b), longitudinal velocity standard deviation (c), transversal velocity standard deviation (d), longitudinal velocity skewness (e), transversal velocity skewness (f), longitudinal velocity kurtosis (g), and transversal velocity kurtosis (h).

Appendix D

Mean and turbulent flow fields in the centre of the vegetated canyon with intersections

In Fig. D.1, we report the $\overline{u}/U_\infty$, $\overline{v}/U_\infty$, σ_u/U_∞, σ_v/U_∞ in cross section in the centre of the vegetated canyon with intersections (cross-section 2 in Fig. 6.1). We report velocity statistics within canyons with wind directions θ=30° and θ=60°. These data were used to calculate the vertical exchange velocity u_d^+ in the vegetated canyon with intersections, with oblique wind direction.

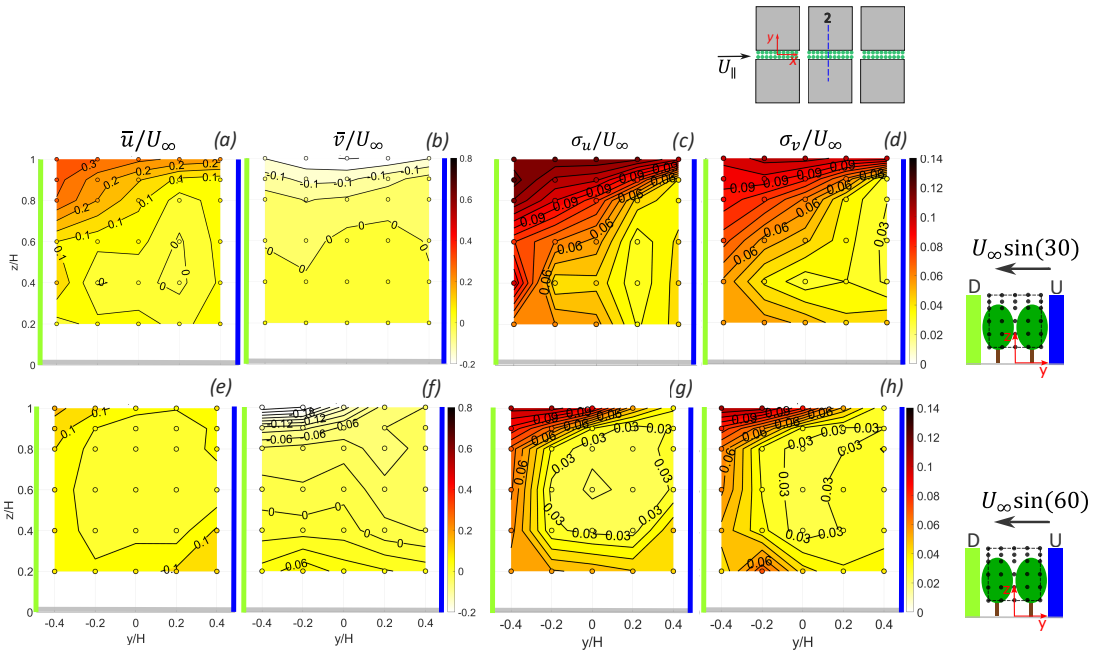


Figure D.1 Transversal behaviour in the centre of the vegetated laterally-opened canyon (cross-section 2) of the mean longitudinal velocity (a,e), mean transversal velocity (b,f), longitudinal velocity standard deviation (c,g), and transversal velocity standard deviation (d,h), for wind directions θ=30° (a-d) and θ=60° (e-h). The sketch in the top-right indicates the position of the measuring cross-section with respect to the intersection (planar view). Green and blue bars indicate the downwind and the upwind walls.

Appendix E

Comparison between velocity statistics measured with LDA and HWA

In Fig. E.1, we report a comparison between vertical profiles of $\overline{u}/U_\infty$, σ_u/U_∞, σ_w/U_∞, and Reynolds stresses ($\overline{u'w'}/U_\infty^2$), measured above the obstacle Configuration 2 with LDA and HWA. For sake of space, we report only vertical profiles in positions Street and Roof, but measurements were performed with both instruments in all the four positions around an obstacle (Street, Roof, Intersect, Canyon).

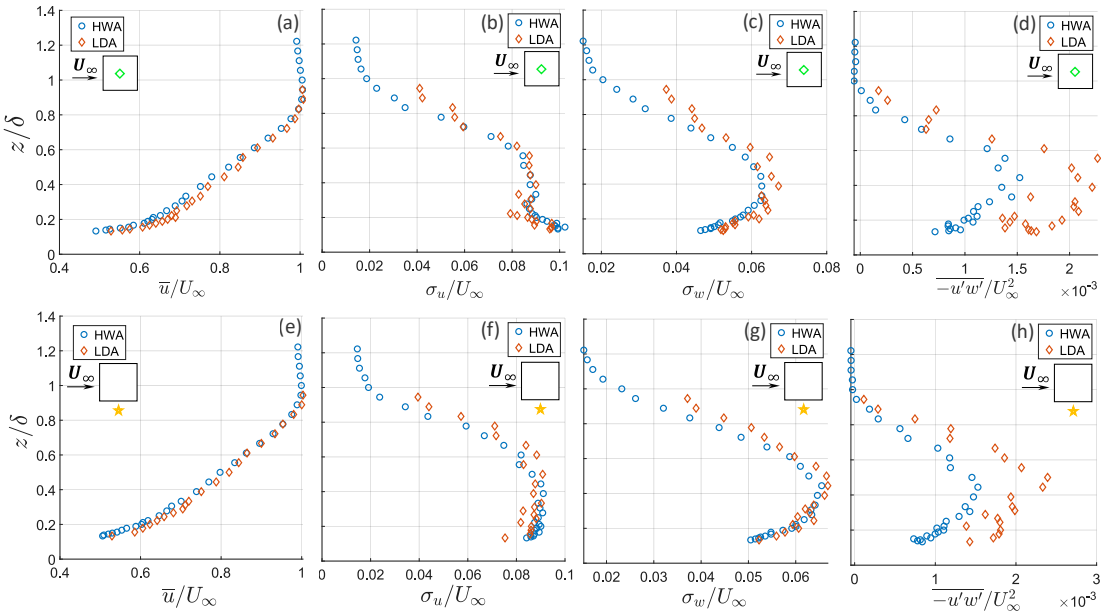


Figure E.1 Comparison between vertical profiles of (a-e) $\overline{u}/U_\infty$, (b-f) σ_u/U_∞, (c-g) σ_w/U_∞, and (d-h) Reynolds stresses ($\overline{u'w'}/U_\infty^2$) measured above obstacle Configuration 2 with LDA and HWA. The white square represents an obstacle and the symbols around it indicate the positions of the vertical profiles.